Physics of Polymeric Ferroic Devices

DISSERTATION

submitted for the award of the title

"Doctor of Natural Sciences"

to the Faculty of Physics, Mathematics, and Computer Science

MAX-PLANCK INSTITUTE FOR POLYMER RESEARCH

AND

JOHANNES GUTENBERG UNIVERSITY OF MAINZ

Morteza Hassanpour Amiri

Mainz, August 2022

Dedication:

To all bright talents never had an opportunity to flourish…

Table of Contents:

Acknowledgment

I would like to express my sincere gratitude to my always supportive supervisor, Prof. Dr. Asadi. I also appreciate all members of AK-Blom for their help and support during my PhD period.

Abstract

Functional polymers are macromolecules with unique and sometimes combined physical properties. For example, poly vinylidene fluoride-co-trifluoroethylene, P(VDF-TrFE), is a well-known random copolymer that is nearly a perfect insulator but also possesses piezoelectricity, a bidirectional property. Upon applying an exerted mechanical stress, electric charges with opposite polarity accumulate on the poles. Similarly, applying a time-variant electric potential difference induces mechanical stress in the structure of the material. P(VDF-TrFE) is also ferroelectric and belongs to a sub-category of piezoelectric materials that can retain their electric polarizations even after removal of the applied external electric field. Consequently, P(VDF-TrFE) has been envisioned for energy harvesting, information storage and multiferroic applications.

In the first three chapters of this thesis, we demonstrate a proof-of-concept single transistor non-volatile memory element using graphene as the semiconductor channel of a field-effect transistor wherein P(VDF-TrFE) is used as the ferroelectric gate insulator. Besides the details of reproducible device fabrication, an experimentally validated device model is presented that can be used for rational design of memory elements based on ferroelectric graphene field-effect transistors for information storage and neuromorphic applications. The model serves as the basis for understanding of the multiferroic field-effect transistors.

In the remaining chapters, voltage generation in piezoelectric P(VDF-TrFE) films is discussed. Using a finite-element analysis method, we investigate some strategies to improve the power output of piezoelectric layers made of P(VDF-TrFE). Porosity is suggested and experimentally validated as a general procedure for improving the voltage output in piezoelectric layers. The findings can be employed in polymer-based multiferroic composites systems to boost their magnetoelectric coupling coefficients.

Finally, the thesis demonstrates multiferroic capacitors based on nanocomposite thin-films of P(VDF-TrFE) and magnetic nanoparticles. For the first time, the theory related to magnetoelectric measurements of multiferroics using a lock-in technique is presented and the internal consistency of the method is experimentally validated. Finally, through experimental investigation and finite element modelling, a detailed study of the polymer-based multiferroic thin-films is presented and discussed extensively.

List of Figures

List of Tables

Chapter 1

Introduction

Motivation

    This chapter provides a brief introduction to the physics of piezoelectrics and ferroelectric polymers as well as polymer-based multiferroics. The focus is on two aspects, voltage generation in piezoelectric polymers and multiferroics, which can be used in energy harvesting devices, and information storage devices based on graphene field-effect transistors. Functional polymeric compounds benefit from the ease of fabrication at a relatively cheaper cost by solution-processed techniques and have the winning card of mechanical flexibility, which is especially crucial in regards to the current surge for flexible, self-powered, and body-mounted biomedical gadgets and implants. Contrary to polymers, inorganic functional materials suffer from brittleness and costly and high-temperature fabrication processes in addition to lack of biocompatibility. However, polymer-based functional materials usually exhibit inferior performance as compared to their inorganic counterparts. One of the objectives of this thesis is to reduce this performance gap by means of employing micro and nanoscale structural modifications in the organic materials and their comprising devices.

1. Ferroic materials

Ferroic materials exhibit hysteretic, thus, non-linear behaviour in their response to external stimuli such as magnetic field, stress or electric field. Due to their fascinating physics and their high technological relevance, ferroic materials have been the topic of intensive research activities since their discovery. Researchers are interested in the fundamental understanding of the origin of this behavior as well as their potential applications particularly for energy conversion, electrical machinery, and data storage to name a few.[1-9] Three ferroic orders have been observed: i) ferroelectricity ii) ferromagnetism and iii) ferroelasticity.[10-12] **Figure 1.1** depicts the hysteresis behavior of magnetization, strain, and electrical displacement in ferromagnetic, ferroelastic, and ferroelectric materials, respectively. Once the applied stimulus exceeds a coercive threshold, the material exhibits its iconic property, namely showing a hysteretic response and a residual variable observed at zero stimulus.
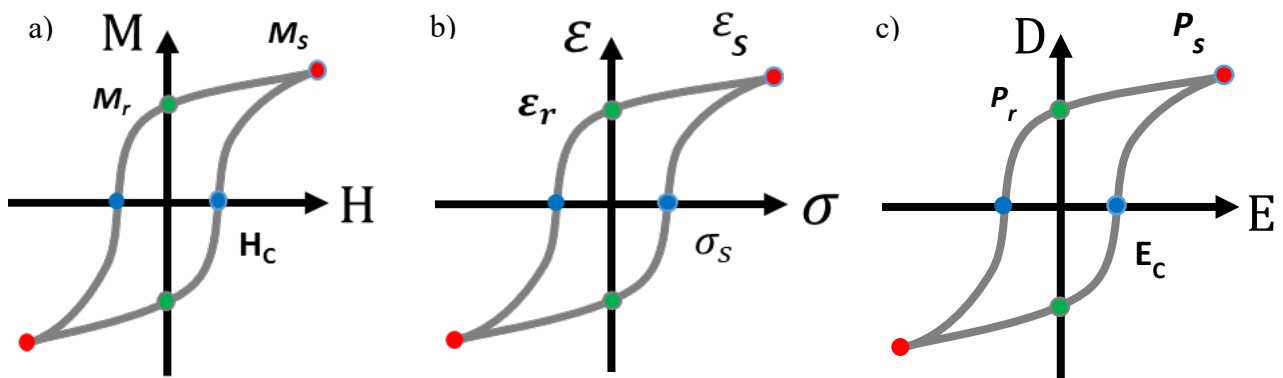
Figure 1.1. *Hysteresis curve for a) magnetization versus magnetic field b) strain versus stress field and c) electric displacement versus electric field in different ferroic materials.*

2. Multiferroics

Multiferroicity refers to the coexistence of more than one ferroic order in a material. **Figure 1.2** elegantly depicts the three ferroic orders related to different domains at the vertices of the triangle, namely, the mechanics, electricity, and magnetism. Each set of arrows indicates the mutual coupling between the two domains. Piezoelectricity that also encompasses ferroelectricity is the bidirectional relation between mechanical and electrical properties of the material, where mechanical stress induces a net electrical polarization in the structure, and vice versa an external electric field results in an induced mechanical strain. Similarly, magnetostriction or piezomagnetisem addresses the magnetically induced mechanical stress and mechanically induced net non-zero magnetization. The latter vertex illustrates the more elusive property of a small class of materials with direct magnetoelectric coupling. The effective realization of a direct magnetoelectric coupling at the microscopic scale is yet to be fully addressed and is currently a topic of active research. [49-58]

Single-phase multiferroic materials are very rare in nature and their origin remained a puzzle for scientists for a long time. This was due to the mutually exclusive nature of ferroelectricity and ferromagnetism in a material.[58] While ferromagnetism is observed in rare earth metals with partially filled d orbitals, ferroelectricity requires electrical insulation and low electrical conductivity. Despite this scarcity, the potential wide range of applications of magnetoelectric coupling in energy harvesting, efficient remote powering, field sensors, hybrid memory elements, etc. has driven the research activities.
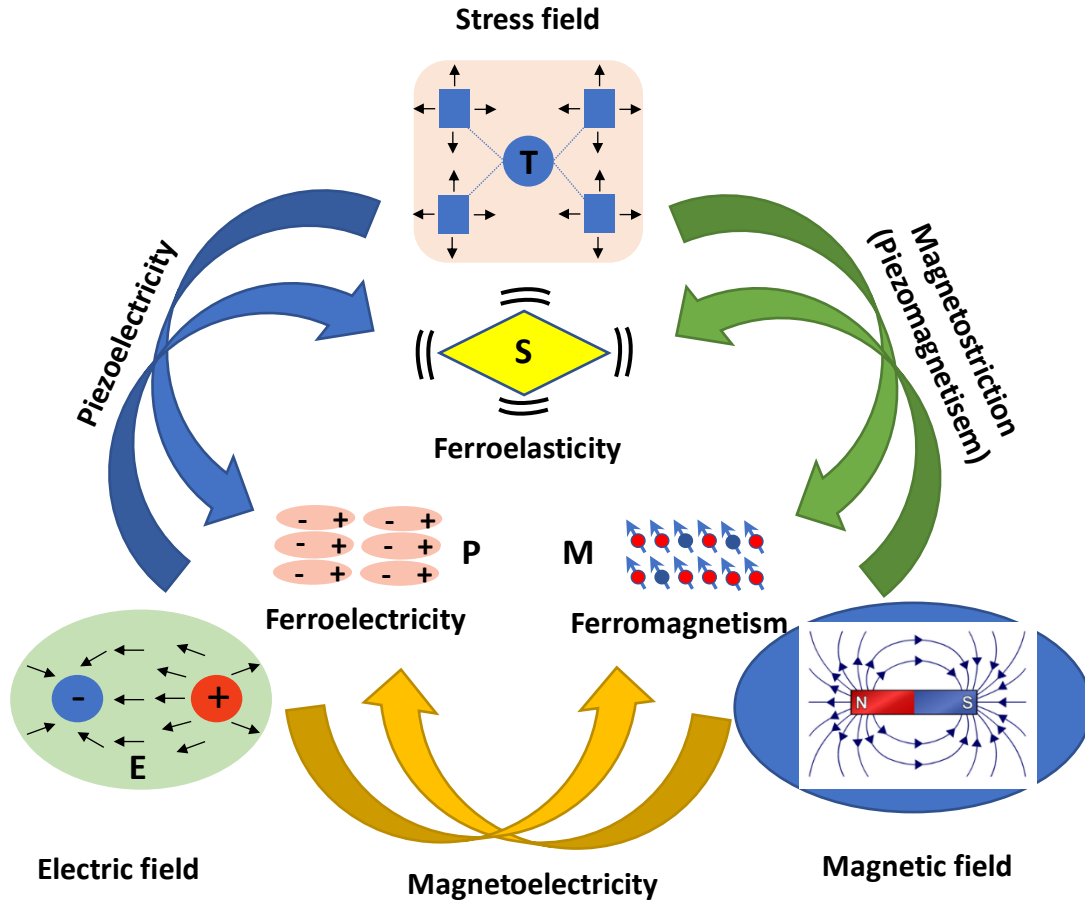
Figure 1.2. *Interplay between various ferroic orders in a multiferroic material.*

3. Ferroelectric materials

Ferroelectricity was first observed in Rochelle salt (KNa ($C_4H_4O_6$) · $4H_2O$) in 1922. The material showed a hysteresis in its electric displacement, D, response versus the applied electric field, E. Due to the similarity of the displacement curve in Rochelle salt with the magnetization hysteresis versus magnetic field of iron, *i.e.*, the newly found property was named ferroelectricity. [13-20] The rudimentary device in this regard is a simple parallel plate capacitor with electrode separation d sandwiching a ferroelectric material. When a voltage difference V is applied, the electric field is given by:

$$E = -\nabla V = \frac{V}{d} \tag{1.1}$$

The electric displacement of the sandwiched material can be written as follows:

$$D = \varepsilon_0 \varepsilon_r E + P \tag{1.2}$$

where ε_0 and ε_r are the electric permittivity of free space and relative permittivity of the ferroelectric material, respectively, and P is the polarisation. While all insulators, depending on their dielectric constant, become polarized when an external electric field is applied, ferroelectric materials have an extra remanent polarisation term, P_r, which accounts for the permanent alignment of the internal dipoles that can change their alignment with respect to the applied field. Thus, when the external electric field vanishes, in contrast with linear dielectric materials, the *D-E* curve does not pass through the origin.

The electric properties of a ferroelectric material are characterized by the following parameters: saturation polarization, P_s, remnant polarization, P_r, and coercive field, E_c. In the presence of an applied field, P_s shows the polarization state of the material when all the domains are aligned with the field direction. The P_r represents the remanent polarization of the material once it is completely polarized and then the external field is reduced to zero. Higher P_r values result in larger ferroelectric loops and manifest a stronger ferroelectricity property. When an electric field antiparallel with the orientation of P_r is applied, the ferroelectric domains start to flip their polarisation orientation and align along the direction of the applied field when the threshold electric field or coercive field, E_c, is reached. Increasing the temperature results in a decrease in E_c as long as the temperature is lower than the Curie temperature designated by T_c. Above T_c, the ferroelectricity will vanish because the material usually undergoes a phase transition to a paraelectric phase, and the crystal structure becomes centrosymmetric.[22]
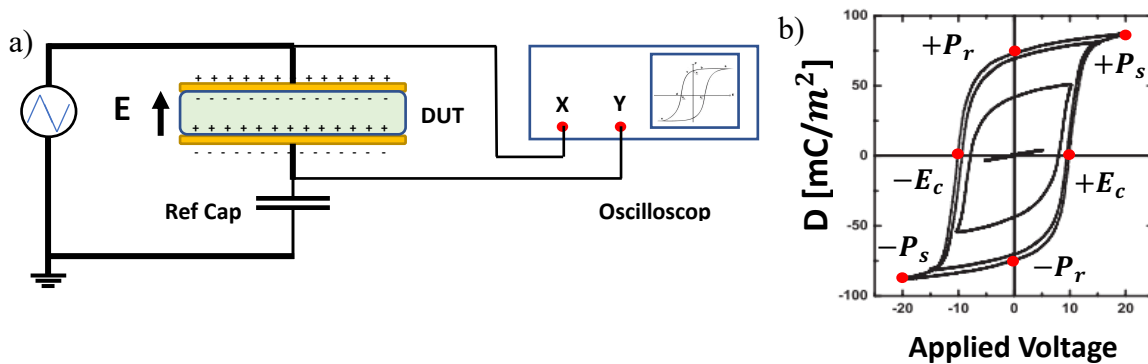
Figure 1.3. *a) Sawyer-Tower setup used for the electrical characterization of a ferroelectric capacitor b) hysteresis loops of a typical ferroelectric material, this figure has been adopted from reference 61*

Figure 1.3a depicts a typical measurement setup called Sawyer-Tower circuit, required for the electrical characterization of the ferroelectric materials. It consists of a function generator, producing a triangular voltage wave, and a reference capacitor. The triangular voltage signal, which is usually amplified, is applied to the series configuration of the reference capacitor and the ferroelectric capacitor as the device under test, DUT. Since in steady-state, ideally no leakage current flows through the ferroelectric capacitor, the accumulated charge across the DUT will be equal to charge accumulated in the reference capacitor. By monitoring the voltage of the DUT and reference capacitor in X-Y mode on the Oscilloscope, the hysteresis loop can be observed. Initially, for the electric field below the coercive field, a reversible and linear curve without any opening appears, as shown in **Figure 1.3b**. When the applied field exceeds the coercive field, a hysteretic behavior appears and the hysteresis becomes larger with increasing the applied electric field until it reaches the saturation limit.

The nonlinear and hysteretic behavior of electric displacement versus electric field of a typical ferroelectric material can be expressed by an empirical equation as follows:

$$P^+(E) = \varepsilon_0 \varepsilon_r E + {}^{P_S}\!/_2 \left(tanh\left(\frac{E+E_c}{\delta}\right) + tanh\left(\frac{E-E_c}{\delta}\right) \right) \tag{1.3}$$

where we have:

$$\delta = 2\mathrm{E_c} \left[\ln\left(\frac{1+\mathrm{P_r}/\mathrm{P_S}}{1-\mathrm{P_r}/\mathrm{P_S}}\right) \right]^{-1} \tag{1.4}$$

Equations **1.3** and **1.4,** when fed by material properties like P_s , P_r , ε_r and E_c, can reconstruct the *D-E* loop of the measured ferroelectric capacitor device. It is worth mentioning that the above equations are used for expressing the behavior of *D-E* curves and do not have any physical interpretation. This stems from the similarity of the hyperbolic Tangent function with the general behavior of hysteretic curves. By adding physically meaningful arguments and multiplicand, Equations **1.3** and **1.4** can be used to express hysteresis curves like *D-E* in a typical ferroelectric material.

4. PVDF and P(VDF-TrFE) as ferroelectric polymers

Figure 1.4 illustrates the molecular structure of PVDF [polyvinylidene fluoride; $(CH_2CF_2)_n$] and its copolymer [poly(vinylidene fluoride-trifluoroethylene); $(CH_2CF_2)_n$-$(CHFCF_2)_m$], which are the most widely used polymeric ferroelectric materials. The PVDF family of polymers possesses several advantages over other polymeric materials such as odd nylons, since PVDF has a relatively larger remanent polarization, a faster polarization switching time, and relatively good stability in a wide range of temperatures. Moreover, PVDF is a highly accessible polymer with large-scale industrial production and is widely used in coating applications for piping when high-temperature resistance in an acidic environment is required. [21-23]

PVDF polymer chains can adopt three different chain configurations, as shown in **Figure 1.4b**, namely trans-gauche-trans-gauche' (TGTG'), all trans (TTT) and a mixture of the two, TTTGTTTG'. Depending on the arrangement of the chains in the crystalline structure of the polymer, 5 different crystalline forms can appear of which only two are a thermodynamically stable piezoelectric/ferroelectric phase. These phases are called *β*-phase, where all chains have the polar trans configuration, or *δ*-phase where the TGTG' chains adopt a polar crystalline configuration. Post-processing steps like physical stretching and application of a strong electric field are required after processing thick-films of PVDF from melt or solution to obtain observable ferroelectricity. The post-processing steps typically lead to an increase in the contribution of the *β* polymorph, which has the largest ferroelectric response among all phases of PVDF.[22-23]

Contrary to PVDF, solution-processed P(VDF-TrFE) thin-films are ferroelectric due to steric effects induced by the TrFE, which promotes formation of the trans configuration in the VDF unit. The only extra step required for enhanced ferroelectric response in P(VDF-TrFE) is annealing at 140 °C in order to enhance the crystallinity of the polymer film. The ferroelectric phase can be obtained by polymerization of PVDF with PTrFE for molar ratios between 50 to 80 % of PVDF.[23]

Since solution-processed P(VDF-TrFE) can be easily spin-coated on device substrates, this technique was widely used to obtain a uniform and pin-hole free layer of P(VDF-TrFE) for the fabrication of the thin film ferroelectric capacitor. By controlling the velocity, acceleration, and duration of spinning of the substrate, required centrifugal force can be produced to spread out the excess of polymer solution to obtain a thin layer of P(VDF-TrFE) on the substrate. Gradual evaporation of the residual solvent takes place and a viscose coating remains on the substrate.

The switching mechanism in P(VDF-TrFE) is mainly attributed to the rotation of the polymeric chain along its backbone, which enables dipole moments to realign themselves in the direction of the applied external field. The dynamic of this switching can be expressed by the following equation: [25-32]

$$t_{SW} = t_\infty e^{E_a(T)/E} \tag{1.5}$$

where E is the applied electric field, $E_a(T)$ is the temperature-dependent activation energy, which amount to 0.85 GV/m for P(VDF-TrFE) and t_∞ is the switching time at the infinite field, which approaches 10 ns for P(VDF-TrFE).[25]
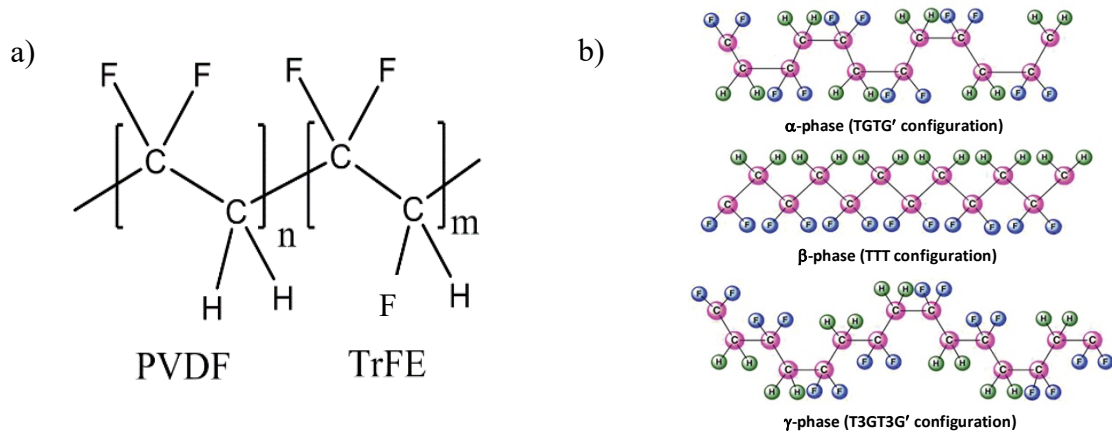
Figure 1.4. *a) Schematic diagram of a P(VDF-TrFE) random copolymer chain. b) Three different conformations of the PVDF chains, the schematic has been adopted from Reference 24.*

The switching of dipoles takes place in two consecutive processes; first, small reversed domains are nucleated and then these domains grow along in the direction of the electric field and sideways. Since nucleation is thermally activated, the activation energy E_a decreases as temperature raises. The coercive field, E_c of a ferroelectric material can also be explained by Equation **1.5**. Regarding the exponential dependency between switching time t_{SW} and amplitude of the applied field, when the applied electric field is significantly lower than a certain value, switching requires a significantly long-time. The switching time can drastically reduce if the applied field exceeds E_c.

5. Graphene

Graphene is the two-dimensional allotrope of carbon, first discovered by Geim and Novoselov in 2005 by isolating monolayers of graphite sheets by means of mechanical exfoliation using scotch tape. Carbon atoms in the graphene layer are organized in an in-plane honeycomb configuration. [33-35] Since this discovery, scientists are continuously fascinated by graphene's electrical, mechanical and optical properties. The high electrical conductivity and charge carrier mobility made graphene a promising candidate material in micro/nanoelectronic devices like FETs. Very high Young's modulus combined with its lightweight opened new horizons for high-end light and strong composite materials. High interaction with light due to its 2D nature accompanied by more than 90% of optical transparency has drawn attention for its potential applications in optoelectronics devices. Lat but not least, the high interface to volume ratio of graphene is promising for various applications in electrochemical systems like batteries and supercapacitors. [36-45]

The performance of graphene in many of the device, however. is compromised because of the method used for graphene synthesis. High-quality graphene sheets obtained by mechanical exfoliation usually suffer from up-scalability issues, which limits applications merely to lab settings. Graphene made by chemical vapor deposition (CVD) has the advantage of being produced in a relatively large area at the cost of having defect sites in the structure with deteriorative effects on the electrical properties. [46-48]

For the graphene layer used as the channel in the FeFET, the electrical properties are the subject of utmost attention. **Figure 1.5a-b** shows a simplified scheme of energy states of the graphene. As a semiconductor with zero band-gap, the valence and conduction bands of graphene touch each other at the Dirac points on vertices of the hexagonal Brillouin zone. When graphene is used as channel semiconductor in a FET, depending on the applied gate bias or impurities, the Fermi energy level can shift to energy levels above or below the Dirac point thus providing graphene with an ambipolar conduction behavior. [49]
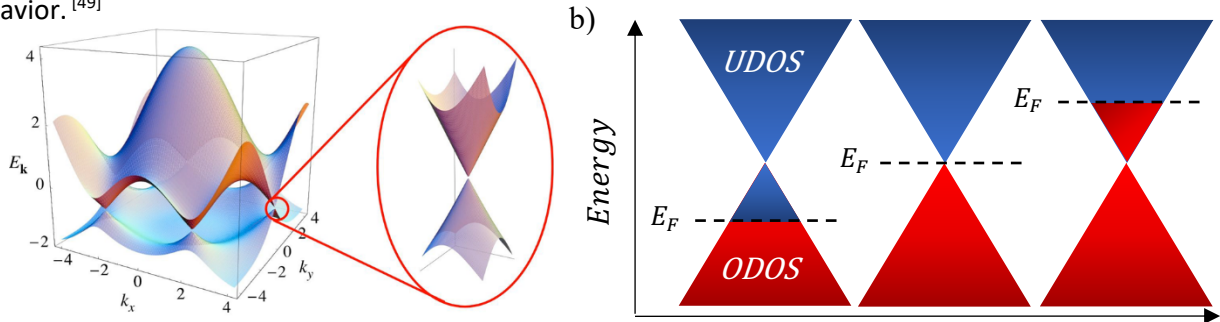
Figure 1.5. a) Valance and conduction band of graphene single layer in the first Brillouin zone touching at the Dirac point, figure has been adopted from reference 50 b) Energy band diagram of graphene at the Dirac point with different impurities or biasing voltage which shifts the Fermi level either in the valence band and occupied density of states (ODOS) or unoccupied density of states (UDOS) and conduction band.

6. Multiferroic polymer composites

Due to the mutually exclusive nature of ferroelectricity and ferromagnetism, natural multiferroics are scarce. The existing single-phase multiferroics show a very low coupling coefficient, which hinders practicality of this class of multiferroic materials for real applications. [51] The alternative strategy is the realization of composite materials consisting of two or more phases. The multiferroic coupling arises by the interaction between the two phases, mostly at the interfaces, upon the application of an external stimuli. Among multiferroic composites, polymer-based composites are specially interesting because of their ease of fabrication using cost-effective low-temperature techniques such as solution-processing.
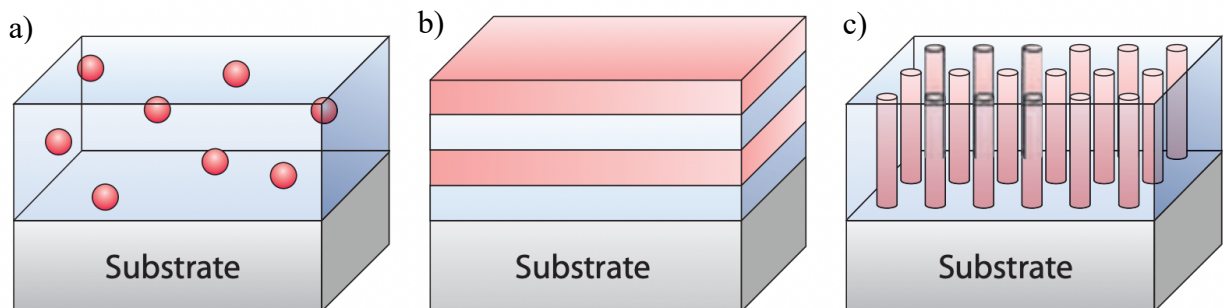
Figure 1.6. Schematic of multiferroic composites with a) 0-3 structure of ferromagnetic nanoparticles embedded in polymeric matrix b) 2-2 structure consisting laminar arrangement of ferroelectric and ferromagnetic materials glued together and c) 1-3 structure of horizontal pillars embedded in polymetric matrix. Figures have been adopted from reference 52.

Figure 1.6 shows different configurations of a polymeric multiferroic composite material consisting of 0-dimensional nanoparticles, 1-dimensional wires, 2-dimensional planes and 3-dimensional matrix. Subject of this thesis is the 0-3 structed polymer-based multiferroic compounds with ferromagnetic nano particles surrounded by a ferroelectric polymer, P(VDF-TrFE), as pictured in **Figure 1.6a**.

7. Multiferroics devices

Since synthetic multiferroics including polymer-based ones possess high coupling between the ferroic phases, various multiferroic devices can be realized. This ranges from magnetic field sensors to efficient energy harvesters for low-power wearable electronics and body implants to hybrid memories for information storage with magnetoelectric read-write capability that can significantly improve the data storage density.

7.1. Ferroelectric field-effect transistors

In a field-effect transistor (FET), as shown in **Figure 1.7a**, a dielectric material also known as the gate insulator, is in contact with a semiconductor layer. When a voltage is applied on the gate terminal, charge carriers of similar polarity are depleted and charges with opposite polarity are attracted the interface between the semiconductor and the gate insulator, forming a channel. A lateral electric field between source and drain contacts on the semiconductor can force the charge carries to flow. At zero gate voltage, the vertical electrical field responsible for channel formation in semiconductors disappears leading to the "off-state" for transistors with a negligible drain-source current. Therefore, the FET can be considered as an electrically controllable on/off switch with two stable states of drain-source current. [26-29]
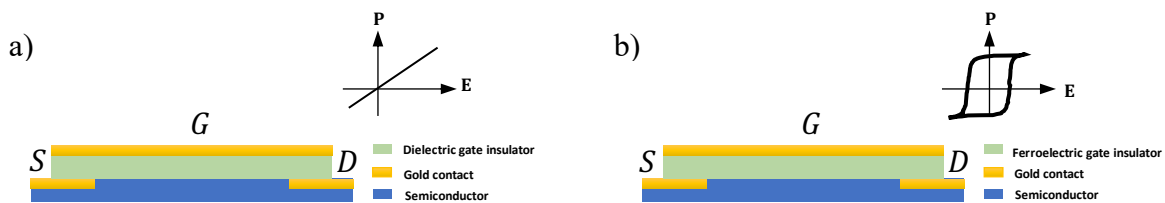
Figure 1.7. Schematics of a) a conventional FET with a linear gate dielectric, and b) FeFET with a ferroelectric gate dielectric.

If the gate insulator is replaced by a ferroelectric material, contrary to conventional FET, a ferroelectric field-effect transistor, FeFET, is obtained (**Figure 1.7b**) which can function as a non-volatile memory element because of the bistability of the remanent polarization of the ferroelectric gate layer. Therefore, the channel conductance shows binary values depending on the polarization state of the gate insulator. These states can be assigned one and zero, thereby enabling the FeFET to function as a memory element. [30-32]

Integration of polymer-based multiferroics as the gate insulator of the FeFET allows for magnetic control of the conduction of the FET channel, thus enabling data encoding in both electric polarization and magnetic moment. To reach to the level of having ultimate information storage capacity with both polarization and magnetization states, we need to understand the physics of the devices. To that end in this thesis, we begin by investigating FeFETs based on graphene transistors. The lessons learned from graphene FeFETs are the first steps towards the design of multi-responsive multi-bit information storage devices.

7.2. Multiferroic energy harvesters

There is an increasing demand for miniaturized low-power consumption electronic systems, which has raised attention about the necessity of diversifying the energy sources to power these electronic systems. Medical body implants, distributed sensory networks and IoT are among frontier applications that would benefit from a battery-less power supply for operation. This is dictated by their size, limited life-time and the need for being recharged in relatively short intervals and above all, possible environmental contaminations. Multiferroic energy harvesters can be a plausible candidate for direct conversion of local sources of energy, like mechanical body motion or available magnetic field to name a few and make the remotely powered system happen.

Polymer-based multiferroics composed of magnetostrictive nanoparticles dispersed in a PVDF matrix can be used as magnetic-field energy harvesters. The nanoparticles react to the magnetic field and stress or strain from the nearby piezoelectric phase. In other words, the nanoparticles function as a source of mechanical vibrations. To optimize the power conversion, one needs to understand the physics of piezoelectric energy harvesters from mechanical vibrations and optimize the piezoelectric phase such that it generates higher voltages for the same applied alternating magnetic field. For example, porosity, as we will show in this thesis, is a possible avenue to substantially enhance the sensitivity of the polymer-piezoelectric to a mechanical excitation.

8. Summary of chapters:

Chapter 2 discusses the improved method of transferring the chemical vaper deposition (CVD) grown Graphene to be used as channel in the single-transistor nonvolatile ferroelectric field effect memory cell. An extra washing step of Graphene in an ammonia bath prior to its transfer to the substrate improves the characteristics of the obtained memory cell by adjusting the Dirac voltage of the graphene layer used as the channel in the device. This was achieved by neutralizing the charged contaminations attached during the release of graphene from the supportive PMMA layers. The results of this chapter have been published in *RSC advances* (DOI: 10.1039/C9RA06738H).

Chapter 3 presents the realization of a ferroelectric field-effect transistor. P(VDF-TrFE) was used as the ferroelectric gate insulator and CVD-grown graphene served as the channel of the transistor in the fabricated device, and the practical challenges related to using graphene as the channel of the FeFET are addressed. Namely, an extra washing step was introduced to remove ion impurities from the transfer process, and de-dope the graphene sheets.

Using the hysteretic behavior of ferroelectric gating, a non-volatile memory element can be obtained, capable of storing binary information by two stable states in the form of a drain-source current, I_{ds}. Device fabrication steps are discussed in detail. Furthermore, a device model is suggested to explain the physics and the characteristic curve of the graphene FeFET. The model takes into the account the physics of 2D materials including the quantum capacitance of the graphene combined with empirical equations explaining ferroelectricity. The obtained device model predicts the behavior of the memory element with good accuracy and consistency. The results of this chapter have been published in *ACS Applied Electronic Materials* (DOI: 10.1021/acsaelm.9b00532).

Chapter 4 Based on the graphene-FeFET non-volatile memory developed in chapter 3, the device geometry has been altered to achieve a memory element with four states, thus more than two stable states, as in Boolean memory devices. This is realized by patterning the ferroelectric insulator along the channel of the transistor and creating trenches. Different thicknesses of the ferroelectric result in different

coercive voltages for the thin- and thick parts of the ferroelectric gate. Fabrication steps required for the realization of a multi-stable state memory are introduced and discussed in detail. The developed analytical model in chapter 3 is modified to capture the physics of the new device architecture and could retrace the I-V characteristic curve of the obtained multilevel memory cell. Based on the obtained model, the practicality of this approach was envisioned for more than four states memory by incorporating ferroelectric gating with more than two different thicknesses in the analytical model. These results have been published in *Advanced Functional Materials* (DOI: 10.1002/adfm.202003085).

Chapter 5 is dedicated to the circuit consideration of the piezoelectric (multiferroic) energy harvesters. It is observed that the reported voltage output of a typical piezoelectric energy harvester is dependent on the input impedance of the measuring instruments. This is especially crucial because the measurements might be deceptive and misleading when the merit of different materials are compared with each other. Here, by considering the circuit equivalent model of piezoelectric materials, issues that arose from the loading effect of the limited input impedance of measurement instruments are discussed. Additionally, an electronic circuit has been designed and realized to minimize this loading effect. Moreover, since it is required to harvest energy in both positive and negative half cycles of the electric response of the Piezoelectric energy harvesters, different rectification circuit solutions are discussed and compared. A detailed design of the prototype circuit with the above-mentioned considerations has been presented. The realized system is consisting of a custom-made, electrically controlled mechanical hammer with adjustable impact frequency and interfacing circuit with active and passive rectifiers. Acquired data is then transferred to a PC software written for controlling the setup and visualization of the real-time device response. The results presented in this chapter form part of a review paper that is prepared on the critical assessment of energy harvesters and is used to provide the first standardized protocol for such measurements.

Chapter 6 presents the finite element method (FEM) numerical analysis to gain more insight into the piezoelectric harvesters and improving the delivered output power by investigation of different structural modifications. The simulation requires coupling equations governing structural mechanics and electrostatics in the material at first instance. Using this framework, piezoelectric material with various geometrical properties are studied and compared, effect of fractional porosity, pore geometry, and pore size are investigated in pursuit of an optimized scenario with maximized voltage output. We used 2D and 3D modeling to implement a detailed study of the local electric field profile, induced strain and deformation, and electric response of various geometries.

Chapter 7 presents a reliable and self-consistent protocol for measuring the magnetoelectric coupling coefficient using a simple versatile lock-in technique. This coupling coefficient is the primary figure of merit for a typical multiferroic material reflecting the strength of the bilateral interplay of the two ferroic orders. This chapter describes the measurement theory and experimentally validates the proposed method. Finally, the most common challenges for accurate measurements of the magnetoelectric coupling coefficient and the possible sources of noise have been discussed.

Chapter 8 takes the FEM analysis one step further and studies voltage generation in a polymer-based multiferroic composite and the magnetoelectric response. The governing constitutional equations are presented and discussed. For the composite fabrication, magnetostrictive nanoparticles dispersed in a P(VDF-TrFE) matrix are considered and characterized in detail to ensure the presence of ferroic-orders coupling. As the composite is exposed to a magnetic field, the force excreted to ferromagnetic nanoparticles generates structural stress in the system. The stress conveys to the piezoelectric polymer and a voltage difference appears between two plates of the capacitor sandwiching the composite. In a

series of simulations, the effect of several parameters is studied to optimize the device response. Effects of size and concentration of magnetic nanoparticles, their dispersion and agglomeration quality, etc. are among the studied parameters. This chapter also take a close look to the fabrication of a multiferroic capacitor made of ferromagnetic nano particles distributed in a ferroelectric polymer matrix.

Reference

1) J. Valasek, *Phys. Rev.* 1920, **15**, 505.
2) Y. Xu, Ferroelectric materials and their applications, *Elsevier* 2013.
3) G. H. Haertling, *J. Am. Ceram. Soc.* 1999, **82**, 797.
4) S. Horiuchi, F. Kagawa, K. Hatahara, K. Kobayashi, R. Kumai, Y. Murakami, Y. Tokura, *Nat. Commun.* 2012, **3**, 1308.
5) L. F. Brown, J. I. Scheinbeim, B. A. Newman, *Ferroelectrics* 1995, **171**, 321.
6) B. Z. Mei, J. I. Scheinbeim, B. A. Newman, *Ferroelectrics* 1995, **171**, 177.
7) T. Itoh, M. Takano, T. Yanagisawa, M. Hashimoto, *Ferroelectrics* 1998, **216**, 35.
8) V. Gelfandbein, D. Katz, *Ferroelectrics* 1981, **33**, 111.
9) K. Tashiro, H. Tadokoro, M. Kobayashi, *Ferroelectrics* 1981, **32**, 167.
10) V. Wadhawan, Introduction to Ferroic Materials (1st ed.). *CRC Press*, 2000.
11) R. C. Smith, S. Seelecke, M. J. Dapino, Z. Ounaies, *Proc. SPIE* 2003 5049.
12) L. Corbellini, J. Plathier, C. Lacroix, C. Harnagea, D. Ménard, A. Pignolet, *J. Appl. Phys.* 2016, **120**, 124101.
13) M. E. Lines, A. M. Glass: Principles and Applications of Ferroelectrics and Related Materials *Clarendon, Oxford* 1977.
14) C. B. Sawyer, C. H. Tower: Rochelle salt as a dielectric, *Phys. Rev.* 1930, **35**, 269.
15) M. Dawber, I. Farnan, J. F. Scott, *Am. J. Phys.* 2003, **71**, 819
16) M. Dawber, K. M. Rabe, J. F. Scott, *Rev. Mod. Phys.* 2005, **77**, 1083
17) E. Fukada, *IEEE Trans. Ultrason. Ferroelectr. Freq. Control*, 2000, **47**, 1277.
18) S. C. Abrahams, *Acta Crystallogr.* 1989, **B 45**, 228
19) L. Martin, A.M. Rappe, *Nat. Rev. Mater.*, 2017, **2**, 16087.
20) J. F. Scott Jpn. *J. Appl. Phys.* 1999, **38,** 2272
21) H. S. Nalwa, Ferroelectric polymers: chemistry: physics, and applications, (1995) CRC Press,
22) J. I. Scheinbeim, B. A. Newman, B. Z. Mei, J. W. Lee, ISAF '92: *Proceedings of the Eighth IEEE International Symposium on Applications of Ferroelectrics, 30 Aug.-2 Sept. 1992*, 1992.
23) J. Harrison, Z. Ounaies, *Encyclopedia of polymer science and technology* 2002, **3**.
24) S. Mishra, L. Unnikrishnan, S. K. Nayak, S. Mohanty, Macromol*. Mater. Eng.* 2018, 1800463.
25) T. Furukawa, Y. Takahashi, K. Nakakubo, H. Kamiya, M. Kutani, *Proceedings of 8th International Symposium on Electrets (ISE 8)*, 1994.
26) Chai, X., Jiang, J., Zhang, Q. et al. *Nat Commun.* 2020, **11**, 2811.
27) J.F. Scott, Paz de Araujo CA. *Science* 1989, **15**, 246(4936):1400-5.
28) R.Naber, C. Tanase, P. Blom, *Nat. Mater.* 2005, **4**, 243–248.
29) Y. T. Lee, D. K. Hwang, W. K. Choi, J. *Korean Phys. Soc.* 2016, **69**, 1347– 1351.
30) Y. Chen, X. Wang, P. Wang, H. Huang, G. Wu, B. Tian, Z. Hong, Y. Wang, S. Sun, H. Shen, J. Wang, Hu, W.; Sun, J.; Meng, X.; Chu, *J. ACS Appl. Mater. Interfaces* 2016, **8**, 32083– 32088.
31) R.G. Kepler & R.A. Anderson, *Adv. Phys.*, 1992, **41:1**, 1-57.
32) 1.A. K. Geim, *Science* 2009, **324**, 1530–1534.
33) K. Novoselov, V. Fal'ko, L. Colombo, *Nature* 2012, **490**, 192–200.
34) S. Bertolazzi, P. Bondavalli, S. Roche, T. San, S.-Y. Choi, L. Colombo, F. Bonaccorso, P. Samorì, *Adv. Mater.* 2019, **31**, 1806663.
35) M. El-Kady, Y. Shao, R. Kaner, *Nat. Rev. Mater.* 2016, **1**, 16033.
36) Ch. Liu, Zh. Yu, D. Neff, A. Zhamu, B. Z. Jang, *Nano Letters* 2010**, 10** (12), 4863-4868.
37) R. Sahoo, T. H. Lee, D. T. Pham, T. H. T. Luu, Y. H. Lee, *ACS Nano*, 2019, **13** (9), 10776-10786.
38) J. Zhu, D. Yang, Z. Yin, Q. Yan, H. Zhang, *Small* 2014, **10**, 3480-3498.
39) M. El-Kady, R. Kaner, *Nat. Commun.* 2013, **4**, 1475.

40) M. F. El-Kady, V. Strong, S. Dubin, R. B. Kaner, *Science* 2012, **335**, 1326–1330.

41) J. Chmiola, C. Largeot, P. L. Taberna, P. Simon, Y. Gogotsi, *Science* 2010, **328**, 480–483.

42) D. Pech, M. Brunet, H. Durou, *Nat. Nanotech.* 2010, **5**, 651–654.

43) M. D. Stoller, S. Park, Y. Zhu, J. An, R. S. Ruoff, *Nano Lett.* 2008, **8**, 3498.

44) W. Gao, N. Singh, L. Song, Z. Liu, A. Reddy, L. Ci, R. Vajtai, Q. Zhang, B. Wei, P. Ajayan, *Nat. Nanotechnol.* 2011, **6**, 496.

45) A. Zurutuza, C. Marinelli, *Nature Nanotech.* 2014, **9**, 730–734.

46) Bae, S., Kim, H., Lee, Y. et al. *Nature Nanotech*. 2010, **5**, 574–578.

47) Vi. Saraswat, R.M. Jacobberger, M. S. Arnold, *ACS Nano* 2021, **15**, 3, 3674-3708

48) T. Knobloch, B. Uzlu, Y.Y. Illarionov, Z. Wang, M. Otto, L. Filipovic, M. Waltl, D. Neumaier, M.C. Lemme, T. Grasser, *Nat Electron* 2022, **5,** 256-266.

49) SW. Cheong, M. Mostovoy, *Nature Mater.* 2007, **6**, 13–20.

50) A. H. Castro Neto, F. Guinea, N. M. R. Peres, K. S. Novoselov, A. K. Geim, *Rev. Mod. Phys.* 2009, **81** (1), 109-162.

51) M. Mostovoy, Nature *Mater.* 2008, **7**, 269–270.

52) Y. Wang, J. Hu, Y. Lin, C. Nan, *NPG Asia Materials* 2010, **2**, 61-68.

53) Multiferroics march on. *Nature Mater*. 2019, **18**, 187.

54) R. Ramesh, *Nature* 2009, **461**, 1218–1219.

55) N. Spaldin, *Nat Rev Mater*. 2017, **2**, 17017.

56) S. Shevlin, Nature *Mater.* 2019, **18**, 191–192.

57) YL. Huang, D. Nikonov, C. Addiego, et al. *Nat Commun.* 2020, **11**, 2836.

58) J. Seidel, L. Martin, Q. He, et al. *Nature Mater.* 2009, **8**, 229–234.

59) Q. He, Y.H. Chu, J. Heron, et al. *Nat Commun.* 2011, **2**, 225.

60) N.A. Spaldin, R. Ramesh, Nature *Mater.* 2019, **18**, 203–212.

61) R.C.G. Naber, P.W.M. Blom, A.W. Marsman, D.M. de Leeuw, *Appl. Phys. Lett.* 2004, **85**, 2032-2034

Chapter 2

Doping free transfer of graphene

Abstract

Doping-free transfer of graphene produced by catalytic chemical vapor deposition (CVD) on copper foil is still a technical challenge since unintentional doping of the transferred graphene layer yields an uncontrolled shift of the Dirac point in graphene-based field-effect transistors (FETs). Typically, CVD graphene is released from the growth template, *e.g.* copper, by etching of the template. During the etching process, ions adhere to the graphene layer resulting in an unintentional doping. We demonstrate that washing the CVD graphene layer in an aqueous ammonia flow bath after copper etching removes most of the unintentional dopants. FETs fabricated from graphene after conventional washing in DI-water display a significant scattering in Dirac bias with lowered mobility. In contrast, FETs from graphene washed in ammonia furnish better performance with high geometrically normalized mobility exceeding 2.4×10^4 cm^2 V^{-1} s^{-1}, and with a balanced transport and a Dirac voltage near zero. The improved FET behaviour is attributed to the effective removal of the ions. A residual ion density of 4×10^{12} cm^{-2} is estimated for the graphene layer without an ammonia washing step.

2.1. Introduction

Two-dimensional (2D) materials such as graphene have been extensively studied for various electronic and optoelectronic applications.[1–5] Several methods have been proposed for wafer-scale production of graphene monolayer, among which catalytic chemical vapor deposition (CVD) of graphene is a technologically viable method.[6,7] To release the graphene layer, a sacrificial polymeric layer, typically poly(methylmethacrylate) (PMMA), is spin-coated on top of an as-grown graphene layer, followed by etching of the copper template. For the fabrication of electronic devices, such as graphene field-effect transistors (FETs), the graphene/PMMA stack is transferred onto a second substrate. FETs are commonly realized by patterning the source and drain electrodes on top of the graphene layer or transferring the graphene/PMMA layer onto a substrate with pre-patterned source and drain electrodes.

Graphene transfer is one of the critical issues in the fabrication of graphene FETs and their upscaling.[8] Since FETs are sensitive interface devices, the presence of ions (or any ionic species) at the interface between the graphene layer and the gate dielectric leads to unintentional doping of the graphene layer, which drastically affects the electrical performance.[9–11] As a result, the Dirac point shifts to voltages much larger than 0 V so that instead of ideal ambipolar behavior, the graphene FET exhibits unbalanced electron/hole transport or even a seemingly unipolar behaviour.

Herein, we demonstrate CVD-based graphene FETs with balanced ambipolar electron/hole transport. Towards that end, we have introduced an extra washing step of graphene in aqueous ammonia after etching away the copper.[12,19] The FETs are fabricated using the conformal transfer technique.[8] Ammonia effectively removes the majority of ions (nearly 4×10^{12} cm^{-2} dopants) that otherwise would unintentionally dope the graphene layer. The extra washing step also improves the mobility of the charge carriers and shifts the position of the Dirac point to biases close to zero volts. We attribute the improved FET behavior to the effective removal of Cu^{2+} from the graphene layer and quantify the density of ions.

2.2. Experimental section

The process flow for graphene transistor fabrication is schematically shown in **Figure 2.1a**. CVD graphene (Graphenea) on Cu foil (25 μm thickness, 99.8%) is coated with PMMA (Aldrich). To minimize errors due to batch-to-batch variations, all the experiments presented here are conducted using graphene obtained from small cuts of the same Cu foil. PMMA is dissolved in toluene (Acros) with 10 wt% and filtrated through 1 μm filters before spin-coating (all materials are used as received). The thickness of the PMMA layer varies from 700 to 800 nm. The graphene layer on the uncoated surface of the copper foil is removed using an oxygen plasma. The Cu foil is etched in a 1 molar aqueous bath of FeCl$_3$, and the floating graphene/PMMA layer is thoroughly washed with DI water. The "ammonia" treatment is performed by placing the floated graphene/PMMA film in a continuous flow bath of NH$_3$: DI-water (1 molar) for 30 min as shown in **Figure 2.2a** followed by a drying step at 40 °C for 12 hours in a vacuum oven at 10^{-1} mbar. Hereafter, we use w-graphene and a-graphene to refer to graphene that is washed in DI-water or aqueous ammonia flow bath, respectively. Subsequently, the graphene/PMMA layers are transferred to a pre-patterned Si-wafer using the conformal transfer technique. After evaporation of residual water, the PMMA layer is removed in a fresh acetone bath. Subsequently, the exposed transferred graphene is washed in a deionized water bath, as depicted in **Figure 2.2b**. The final cleaning processes are repeated several times to minimize the PMMA debris.
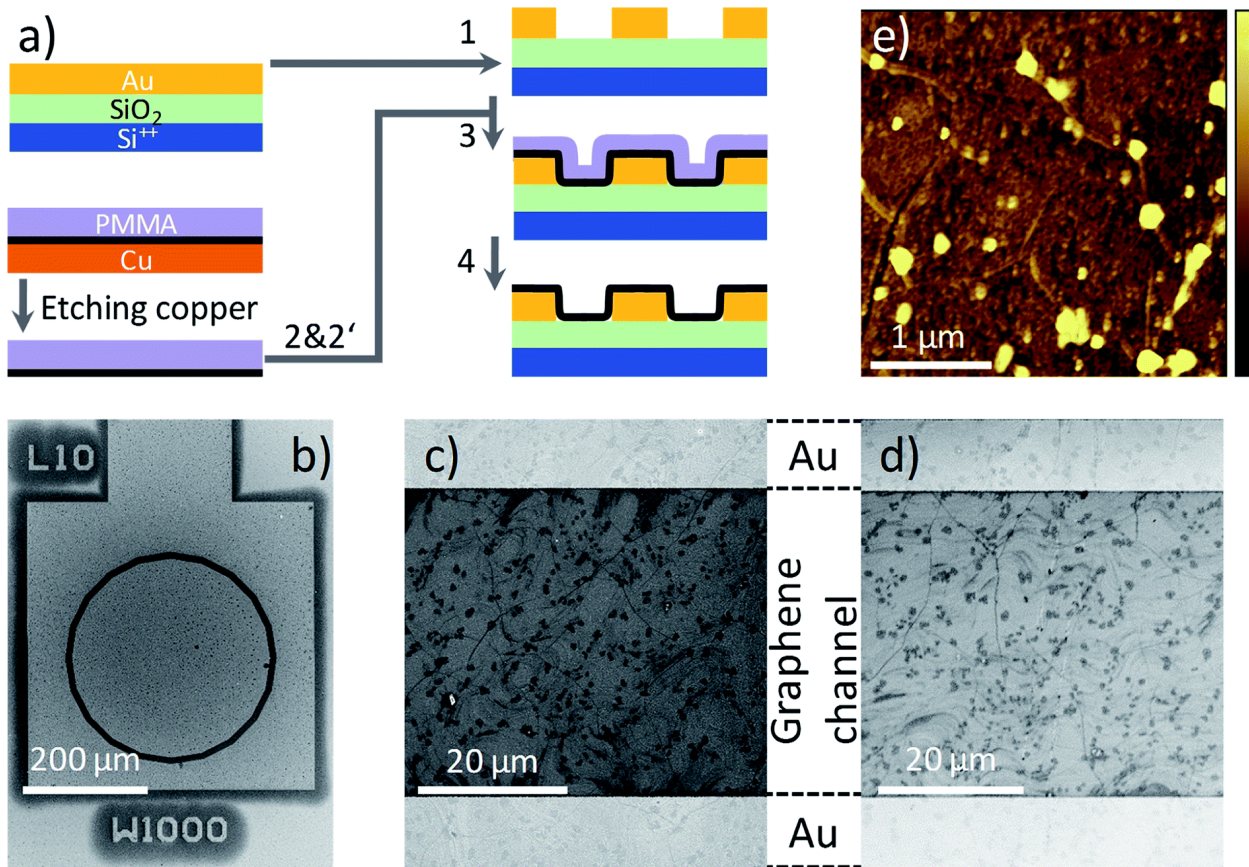
Figure 2.1. *a) Process flow for the fabrication of the graphene transistors. (1) The electrodes are patterned on the substrate. After etching copper template, graphene/PMMA is washed in DI-water, (2) or DI-water and subsequently in aqueous ammonia, (2') and then conformal transferred onto the substrate (3). In (4), PMMA is washed away. b) SEM images of a transistor and one of the CTLM test structures with a channel width of 1000 µm and channel length of 10 µm after coating with the graphene layer. c) and d) SEM images of w-graphene and a-graphene, respectively, transferred onto a pre-patterned FET test structure. The bright region on the top and bottom are the Au contacts of the test structure, and the area in between the contacts is uniformly covered with the graphene layer. e) AFM topography images of the a-graphene after washing in ammonia flow bath. The topography scale bar is from 0 to 15 nm. The bright spots are due to PMMA debris.*
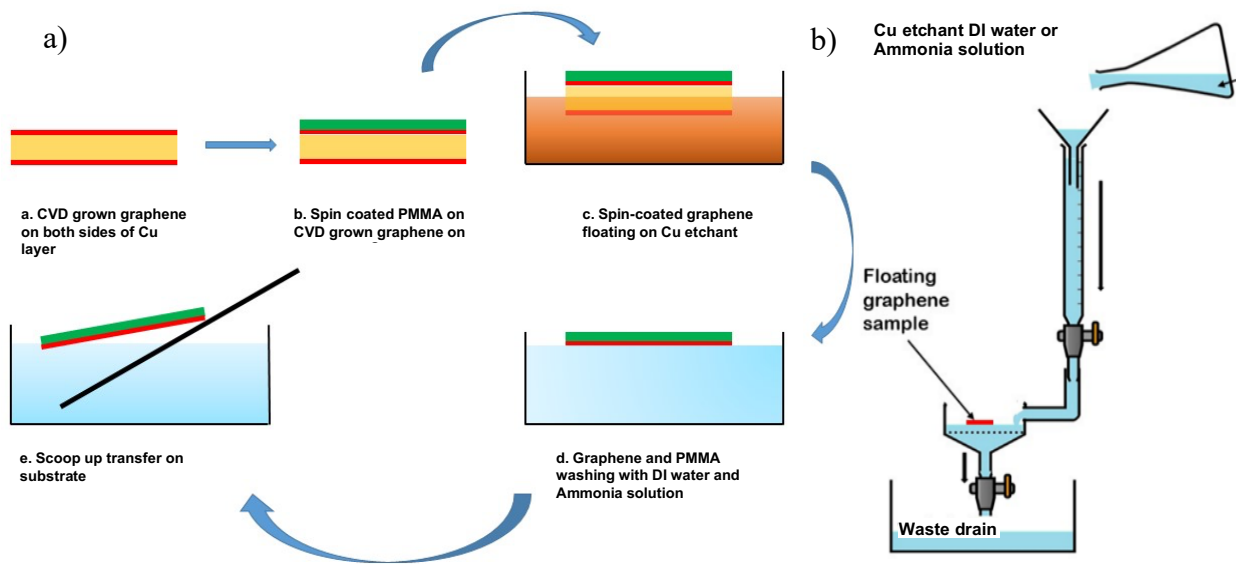
Figure 2.2. *a) Steps of releasing the graphene layer from the Cu layer b) home-made setup for extra washing steps of graphene in ammonia bath.*

The pre-patterned substrates are fabricated on 6-inch Si wafers with 250 nm of thermally grown SiO_2. The electrodes are fabricated by sputter deposition of Ti/Au (2 nm/150 nm) and patterned by conventional photolithography. The spacing between the source and drain electrode varies from 1 µm to 40 µm at a fixed channel width of 1000 µm, having a concentric geometry. A scanning electron microscopy (SEM) image of the transistor test structure is given in **Figure 2.1b**. The SiO_2 surface is passivated with hexamethyldisilazane (HMDS) prior to the conformal transfer of graphene/PMMA. The graphene transferred onto a pre-patterned substrate is inspected using SEM. Although the pre-patterned substrates have an uneven topography, the SEM image presented in **Figure 2.1c-d** provide evidence that the graphene morphologies on the Au contact and the SiO_2 layer are identical and extrinsic defects such as cracks or film discontinuities are absent. Notably, identical morphologies are observed for both w- and a-graphene. Both graphene layers showed traces of PMMA debris. A typical atomic force (AFM) topography image for the a-graphene layer is shown in **Figure 2.1e**. The same AFM images are also obtained for the w-graphene (not shown here). From both TEM and SEM images, it is clear that washing the graphene layer in an ammonia flow bath does not harm the integrity of the graphene layer. The presence of the PMAA layer during the ammonia washing and transfer steps is helpful for the structural integrity of the graphene.

Optical microscopy and atomic force microscopy (AFM) (Nanoscope Dimension 3100 Bruker) were used to analyze the surface morphology of the transferred graphene films before and after ammonia treatment. X-ray photoelectron spectroscopy (XPS) was conducted with a Kratos Axis Ultra DLD spectrometer (Kratos, Manchester, England) using Kα excitation of an Al source with a photon energy 1487 eV. The data was acquired in the hybrid model with a beam spot size of 300×700 µm^2 using a 0° take-off angle, defined as the angle between the surface normal and the axis of the analyzer lens. A charge neutralizer was used during spectra collection to compensate for sample charging. Survey and detailed region XP spectra were collected by setting the analyzer pass energy at 80 eV, C 1s and O 1s high-resolution spectra were collected with an analyzer pass energy of 20 eV. A neutralizer was constantly used during spectra collection. No X-ray damage was inferred to the sample during measurements. Atomic compositions were calculated by subtracting a linear background from the collected spectra with setting an analyzer pass energy at 80 eV. The peak areas were normalized by the manufacturer supplied sensitivity factors, and atomic compositions were calculated accordingly with CasaXPS software.

The sheet resistance of the graphene layer before and after ammonia treatment is determined using a circular transfer line test method (CTLM), as detailed in reference [8]. The sheet resistance is obtained by forcing different constant currents (ranging from 1 μA to 100 μA) and measuring the voltage drop. In total, 32 test structures are measured. The extracted sheet and contact resistances are constant for different current levels.

Metal/insulator/graphene/metal (MIS-) diodes are fabricated by deposition of Cr/Au (1 nm/50 nm) onto thoroughly cleaned glass substrates. After deposition of the graphene/PMMA layer on the substrates and subsequent drying, 100 nm of an Au top contact are evaporated through a shadow mask. The PMMA layer thickness was 700 to 800 nm. The capacitors had a device area of 0.16 mm^2. For each case, 25 MIS-diodes are fabricated, and the results are averaged. All electrical measurements were performed in high vacuum (10^{-6} mbar) using a Keithley 4200 semiconductor characterization system and a Keysight 4980 precision LCR meter.

First, the sheet resistance, R_{sh}, of the graphene layer after different washing processes are determined from the CTLM test structures.[8] The R_{sh} for w-graphene amounts to 450 Ω $\square^{-1}$ and remains constant for different current levels, whereas the a-graphene layer shows an increased R_{sh} of 500 Ω $\square^{-1}$. Observation of higher R_{sh} is due to the de-doping of the graphene layer.

Transfer characteristics of the FET fabricated with w-graphene is presented in **Figure 2.3**. The w-graphene FET exhibit a significant shift in Dirac voltage towards positive voltage and an unbalanced transport leading to a "seemingly" unipolar *p*-type instead of an ambipolar-like behavior. Both observations indicate that the w-graphene layer is doped with positively charged ions. The presence of ions screens the gate bias and shifts the Dirac voltage to higher positive voltages. Therefore, we attribute the unipolar characteristics of the w-graphene FET to unintentional doping of the graphene layer during the transfer process.[13–16] This can be caused by copper, water or etchant (FeCl$_3$ in our case) ions. A doping/de-doping mechanism will be discussed later.
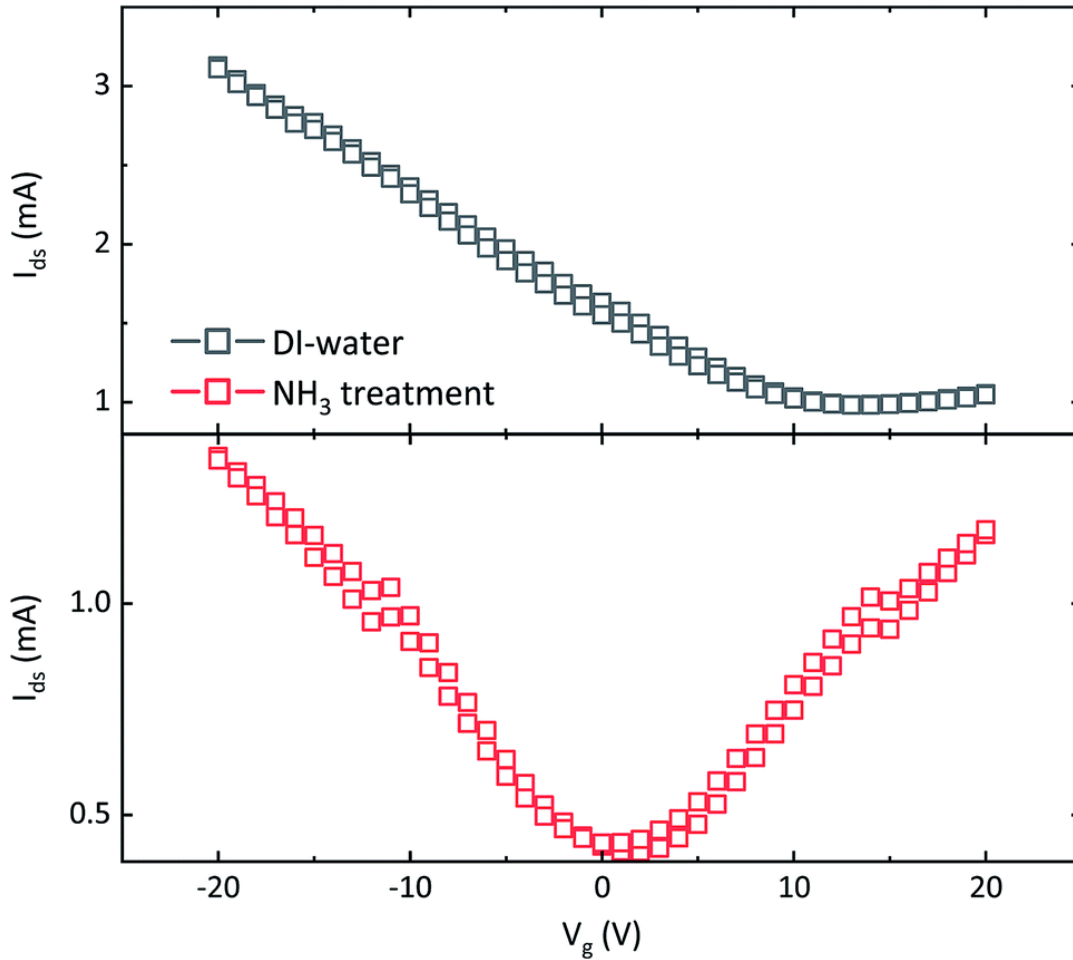
Figure 2.3. *Transfer characteristics of FETs fabricated with graphene layers that are washed only in DI-water (top) and DI-water plus aqueous ammonia flow (bottom). Both transistors have channel lengths and widths of 10 and 1000 μm, respectively. The bias on the drain electrode is +100 mV. The source electrode is grounded.*

To eliminate the troublesome unintentional doping and recover ambipolarity in the graphene FETs, we have introduced an extra washing step in an ammonia flow bath, right before transfer of the graphene/PMMA layer onto the FET substrate. The FET transfer characteristic of the resulting a-graphene FET is presented in **Figure 2.3**. Interestingly, the FET shows a shift of the Dirac voltage to a gate bias near zero volts, namely 1–2 V. Moreover, the transistor shows a nearly symmetric transfer curve. This indicates a balanced charge carrier concentration in the graphene layer, *i.e.* the Fermi level is near or at the Dirac point, which means that ions or charged species are absent. It should be added that both transistors presented in **Figure 2.2** are fabricated from the same batch of CVD graphene coated with PMMA.

It has been recently demonstrated that using paraffin instead of PMMA for the graphene transfer yields a four-fold increase in field-effect mobility, μ_{FE}, of the graphene layer.[17] Since μ_{FE} is a device parameter that is affected by the geometrical parameter *W/L* (channel width/length), for a fair comparison, the normalized mobility, μ_n, is used, which is defined as the field-effect mobility, μ_{FE} multiplied by the geometrical parameter *W/L*:

$$\mu_n = \frac{W\mu_{FE}}{L} = \frac{\partial I_{ds}/\partial V_g}{C_{ox}V_{ds}} \tag{3.1}$$

where C_{ox} is the capacitance of the gate dielectric. The geometrical normalization allows for a fair comparison between the mobilities obtained from the state-of-the-art paraffin-enabled graphene FETs and those presented in **Figure 2.3**. The maximum calculated μ_n for the paraffin transferred graphene amounts to 6.5 x 10^3 whereas μ_n for a-graphene amounts to 2.6 x 10^4, which is a factor of 4 larger.

The current in the a-graphene FET is lower than the one in the w-graphene FET. This indicates that the ammonia treatment de-dopes the graphene layer and reduces the number of the residual carriers in the graphene layer. We suggest a tentative dedoping mechanism as follows. Aqueous $FeCl_3$ is a well-known etchant for copper, and a strong Lewis acid. The chloride plays an essential role in dissolving copper since Cl is a strong complexing agent for Cu^{2+} ions. The etching reaction is written in a simplified form as:

$$2Fe^{3+} + Cu \longrightarrow 2Fe^{2+} + Cu^{2+}$$

The Cu ions in the form of $CuCl_2$ are soluble in water. As a result, there can always be traces of Cl^- or Cu^{2+} ions in w-graphene. The extra washing step of graphene in an ammonia flow bath is ideal for removing both ions. The NH_3 molecules extract the residual Cl^- ions from the graphene layer as ammonium chloride, which is soluble in water and is washed away. Furthermore, the Cu^{2+} ions form an ionic complex in water, namely hexaaquacopper (II) ion $[Cu(H_2O)_6]^{2+}$. The ammonia acts simultaneously as a ligand for the $[Cu(H_2O)_6]^{2+}$ ions to form solid precipitates of the neutral complex according to the following reaction:

$$[Cu(H_2O)^6]^{2+} + 2NH_3 \longrightarrow [Cu(H_2O)_4(OH)^{2-}] + 2NH_4^{2+}$$

Therefore, the extra ammonia washing step would also remove Cu^{2+} ions, potentially acting as a dopant. To unambiguously demonstrate the presence of ions and further estimate their surface concentration, we have performed XPS measurement for the graphene layer before and after ammonia transfer. High resolution X-ray photoelectron spectra [18] for C 1s, Cu 2p, Fe 2p and Cl 2p for both w- and a-graphene are presented in **Figure 2.4**. The C 1s spectrum of the graphene does not change before and after ammonia treatment, indicating that ammonia does not attack the C=C bonds. The Fe 2p spectra show that washing the graphene layer with DI water effectively removes Fe ions, as the XPS spectra do not show the presence of Fe before and after ammonia flow bath treatment. The Cu 2p spectra clearly show a weak signal near 930 eV, which could be assigned to Cu ($2p_{3/2}$) electrons. After the ammonia washing step, the weak signal has disappeared in the background noise. Therefore, washing of the graphene in the ammonia flow bath has removed minute traces of Cu ions. The difference in XPS spectra is more pronounced for the Cl 2p survey of w- and a-graphene. While the a-graphene does not show the presence of Cl, the w-graphene clearly shows a peak at ~ 199–200 eV. The amount of Cl for the w-graphene and a-graphene is calculated, amounting to 0.27 ± 0.04% and 0.16 ± 0.04%, respectively. Therefore, using an ammonia flow bath treatment has effectively removed the majority of the Cl ions.
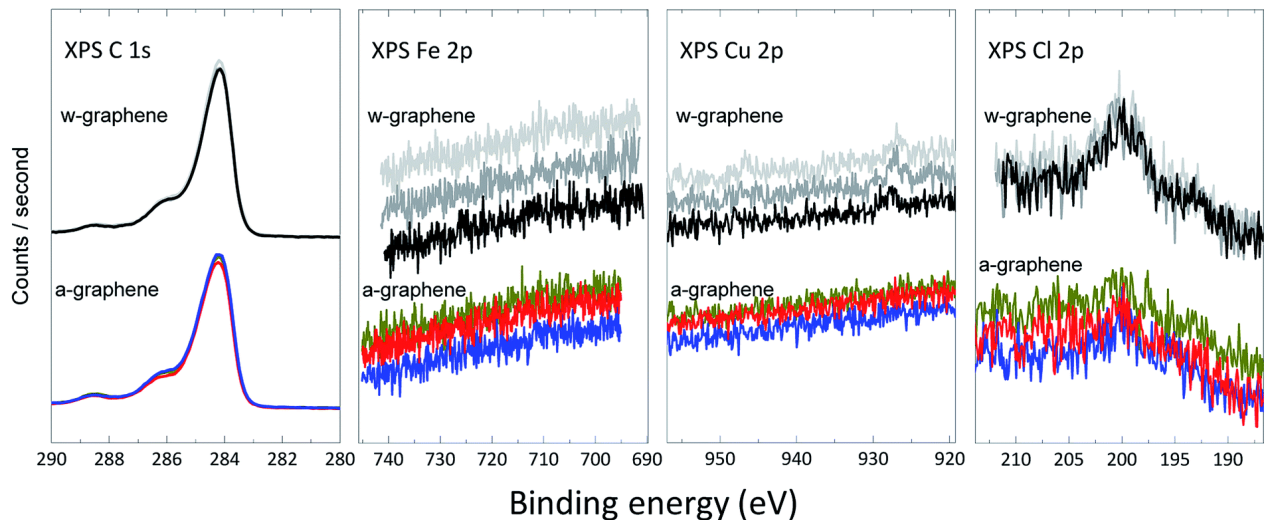
Figure 2.4. *High-resolution C 1s, Fe 2p, Cu 2p, and Cl 2p XPS spectra for w-graphene (top) and a-graphene (bottom). For every graphene layer, three separate samples are measured.*

To estimate the concentration of ions, we have fabricated MIS-diodes. A constant DC bias of +10 V superimposed with an AC signal of 0.1 V with variable frequency is applied to the Au electrode contacting PMMA. The capacitance–frequency responses of the MIS-diodes are given in **Figure 2.5**. MIS-diodes from w-graphene show a decreasing capacitance with increasing frequency. The capacitance at 100 Hz is 160 pF which reduces to 130 pF at 100 kHz. The reduction in capacitance is directly related to ion mobility because, at low frequencies, the ions can follow the electric field changes while they are static at a high frequency. In sharp contrast, the MIS-diodes fabricated with a-graphene possess a lower capacitance of ~ 30 pF that does not vary with the excitation frequency. A constant capacitance over an extensive frequency range indicates that ions are absent in the MIS-diode stack. Since both MIS-diodes have similar PMMA thickness, we can calculate the difference in the number of excess positive ions/charges in w-graphene by considering the capacitances measured at 100 kHz. Taking 130 and 30 pF for w- graphene and a-graphene, respectively, we have estimated an areal doping density of 3.9×10^{12} cm^2 for w-graphene. The doping density is nearly the same as the intrinsic carrier density in graphene. As a result, a nearly two-fold increase in the current of the transistors is expected when we assume that the mobility remains constant. Interestingly, the currents at V_g = 20 V for the transistors presented in **Figure 2.3** differs by a factor of 2.
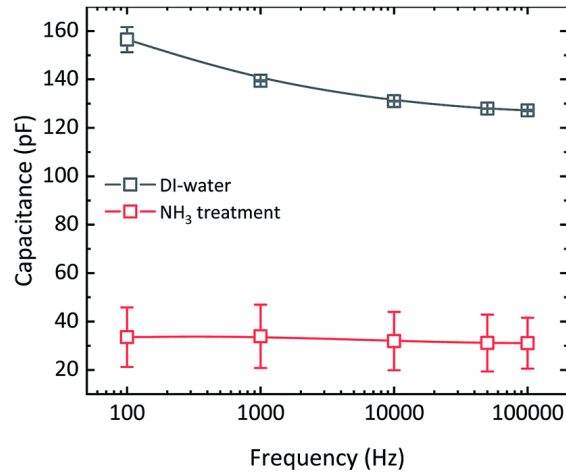
Figure 2.5. *Frequency response of the MIS-diodes fabricated with graphene layers that are transferred after washing in DI-water and aqueous ammonia. Every data point is an average of 5 different devices. The bias applied to the Au electrode contacting PMMA is 10 V. The amplitude of the AC signal is 0.1 V. The MIS-diodes have an area of 0.4 x 0.4 mm2. The solid line is drawn as a guide to the eye.*

2.3. Conclusion

In summary, washing the graphene layer after etching copper in an ammonia flow bath is crucial to achieve FETs with balanced transfer characteristics and close to zero Dirac voltage. Ammonia can effectively remove both chlorine and copper ions. We note that the PMMA transfer technique is not ideal for the realization of high-quality graphene FETs. However, by combining an ammonia flow-bath with more advanced transfer techniques, high-performance CVD-graphene based FETs are within reach.

Reference

1) K. S. Novoselov, A. K. Geim, S. V. Morozov, D. Jiang, Y. Zhang, S. V. Dubonos, I. V. Grigorieva and A. A. Firsov, *Science*, 2004, **306**, 666.
2) S. Wang, Z. Fan, Y. Cui, S. Zhang, B. Yang and H. Chen, *Carbon*, 2017, **111**, 486.
3) S. Wang , Y. Si , J. Yuan , B. Yang and H. Chen , *Phys. Chem. Chem. Phys.* 2016, **18** , 24210.
4) S.-J. Han, A. V. Garcia, S. Oida, K. A. Jenkins and W. Haensch, *Nat. Commun.* 2014, **5**, 3086.
5) S. Bae, H. Kim, Y. Lee, X. Xu, J.-S. Park, Y. Zheng, J. Balakrishnan, T. Lei, H. Ri Kim, Y. Il Song, Y.-J. Kim , K. S. Kim , B. Özyilmaz , J.-H. Ahn, B. H. Hong and S. Iijima , *Nat. Nanotechnol.* 2010, **5**, 574.
6) E. C. P. Smits , A. Walter , D. M. de Leeuw and K. Asadi , *Appl. Phys. Lett.*, 2017, **111** , 173101.
7) I. Levchenko , K. Ostrikov , J. Zheng , X. Li , M. Keidar and K. B. K. Teo , *Nanoscale*, 2016, **8** , 10511.
8) K. Asadi , E. C. Timmering , T. C. T. Geuns , A. Pesquera , A. Centeno , A. Zurutuza , J. H. Klootwijk , P. W. M. Blom and D. M. de Leeuw , *ACS Appl. Mater. Interfaces*, 2015, **7**, 9429.
9) L. Jiao, L. Zhang, X. Wang, G. Diankov and H. Dai, *Nature*, 2009, **458**, 877.
10) H. Liu, Y. Liu and D. Zhu, *J. Mater. Chem.*, 2011, **21**, 3335.
11) X. Wang , Y. Ouyang , X. Li , H. Wang , J. Guo and H. Dai , *Phys. Rev. Lett.*, 2008, **100**, 206803.
12) X. Wang, X. Li, L. Zhang, Y. Yoon, P. K. Weber, H. Wang, J. Guo and H. Dai, *Science*, 2009, **324**, 768.
13) H. Wang, Y. Wu , C. Cong , J. Shang and T. Yu , *ACS Nano*, 2010, **4**, 7221.
14) Z. Yan, J. Yao, Z. Sun, Y. Zhu and J. M. Tour, *Small*, 2012, **8**, 59.
15) S. Myung , J. Park , H. Lee , K. S. Kim and S. Hong , *Adv. Mater.*, 2010, **22** , 2045.
16) Q. Yan , B. Huang , J. Yu , F. Zheng , J. Zang , J. Wu , B.-L. Gu , F. Liu and W. Duan , *Nano Lett.*, 2007, **7** , 1469.
17) W. S. Leong , H. Wang , J. Yeo , F. J. Martin-Martinez , A. Zubair , P.-C. Shen , Y. Mao , T. Palacios , M. J. Buehler , J.-Y. Hong and J. Kong , *Nat. Commun.*, 2019, **10**, 867.
18) J. F. Moulder, W. E. Stickle, P. E. Sobol and K. D. Bomben, Handbook of X-ray Photoelectron Spectroscopy. A Reference Book of Standard Spectra for Identification and Interpretation of XPS Data, J. ChastianPerkin-Elmer Corp., Eden Prairie, 1992.
19) M. H. Amiri , J. Heidler , K. Müllen and K. Asadi , *ACS Appl. Electron. Mater.*, 2020, **2,** 2-8.

Chapter 3

Design Rules for Memories Based on Graphene Ferroelectric Field-Effect Transistors

Abstract

Despite the great progress of ferroelectric gated field-effect transistors (Fe-FETs) based on graphene and other 2D materials, a device model that accurately describes the hysteretic transfer characteristics and provides guidelines on performance enhancement of the Fe-FET is still lacking. This chapter presents an experimentally validated analytical model that couples charge displacement of the ferroelectric layer with the charge transport in the graphene layer. The model describes the hysteretic transfer characteristics of the Fe-FETs with good accuracy and predicts that the on/off ratio of the graphene Fe-FET is determined by the Dirac bias and the charge carrier mobility. The model predicts the unsuitability of an ideal graphene layer for memory applications and outlines the conditions to achieve the best memory performance in graphene Fe-FETs. The model is generic and can be as well used for Fe-FETs based on other 2D materials.

3.1. Introduction

Ferroelectric field-effect transistors (Fe-FETs) based on two-dimensional (2D) materials, where a ferroelectric material is used as the gate dielectric,[1–9] have been envisioned for application in high-speed non-volatile memories,[10–12] THz plasmonics,[13] and broadband photodetectors.[14] The ferroelectric polarization of the gate modulates the charge carrier density in the nearby graphene channel, yielding a hysteretic transfer characteristic with two distinct bistable conductance levels at zero gate bias.[15] Due to the long retention time of the bistable conductance levels, graphene-based Fe-FETs have been exploited for memory applications.[16–20] Wafer-level upscaling,[21–23] integration on flexible foils,[23–26] and even fully solution processed graphene Fe-FETs[27] have been reported.

The full advantage of 2D materials in Fe-FETs has remained obsolete, as there is no experimentally verified device model that can provide guidelines toward performance optimization. This shortcoming can be explained as follows: Fe-FETs are sensitive interface devices. The presence of trapped charges or impurities and charged species such as dopants at the interface between the ferroelectric and the semiconductor layer can greatly alter the hysteretic characteristics of the Fe-FET.[24,28–34] The charge traps and/or impurities can originate from both the ferroelectric and the graphene layer. For instance, graphene Fe-FETs have shown both ambipolar as well as "seemingly" unipolar p-type hysteretic behavior, independent of the source of the graphene layer.[17,35] Leftovers of the polymeric transfer layer at the graphene/ferroelectric interface, and as discussed in previous chapter, residual copper, etchant, or water at the graphene/substrate interface, result in unipolar or even complex anti-hysteretic transfer characteristics and complicate development of a universal device model.[16,36]

Toward a device model for graphene-based Fe-FETs, two issues should be addressed: (i) processing of chemical vapor deposition (CVD)-based graphene Fe-FETs with the aim to obtain ambipolarity and (ii) incorporating the polarization of the ferroelectric gate into the physics of the graphene transistors. Once accomplished, such a model should also be applicable to other 2D materials such as MoS_2, WS_2, graphene nanoribbons, and black phosphorus.

This chapter presents an analytical model describing the hysteretic transfer characteristics of the Fe-FETs. Validation of the model is enabled by the reproducible fabrication of ambipolar CVD-based graphene Fe-FETs using a conformal transfer technique.[37] Ferroelectric poly(vinylidene fluoride-co-trifluoroethylene), P(VDF-TrFE), is used, which has a fully saturated hydrocarbon backbone. The lack of dangling bonds is assumed to minimize charge trapping by the ferroelectric at the interface with the graphene layer. A layer of P(VDF-TrFE) is directly deposited on the CVD-grown graphene to serve as the transfer polymeric support and later as the gate dielectric. The graphene Fe-FETs are fabricated by transferring the graphene/P(VDF-TrFE) stack on to a pre-patterned substrate. Conventionally transferred graphene layers show p-doping and result in "seemingly" unipolar Fe-FETs. Capacitance–voltage (C–V) measurements of the metal/P(VDF-TrFE)/graphene (MIS-) diodes show that the p-doping of graphene originates from negatively charged ions. From the C–V measurements of the MIS-diodes, the ion concentration is estimated. Introducing an extra washing step of the graphene layer in an aqueous ammonia solution retrieves the ambipolar behavior in Fe-FETs. Finally, an analytical model is presented that with a good accuracy describes the transfer characteristics of both graphene Fe-FETs. The model couples the ferroelectric displacement loop of P(VDF-TrFE) to the charge transport in a graphene FET. The model predicts that beside the ferroelectric parameters, namely remanent polarization, coercive field, and dielectric constant, the Dirac bias is a crucial parameter in determining the on/off ratio of the graphene Fe-FETs. At last, appropriate conditions to achieve the highest on/off ratio in a graphene FE-FET are predicted.

3.2. Experimental

Monolayer CVD-graphene on Cu foils (25 µm thickness, 99.8%) was purchased form Graphenea and used as received. The CVD samples on Cu foils were coated with P(VDF-TrFE) (65%–35%) molar ratio, (purchased from Solvay). P(VDF-TrFE) was dissolved in methyl ethyl ketone (MEK) with 10 wt% concentration and filtrated through 1 µm filters prior to deposition. The thickness of the P(VDF-TrFE) layer spin-coated on the Cu/graphene layer varied from 800 to 1500 nm. The P(VDF-TrFE) layer functioned as the polymeric transfer layer as well as the gate dielectric in the final Fe-FETs. The free graphene layer on the surface of the Cu foils was removed using an oxygen plasma. The Cu foil was etched in a 1 M aqueous bath of $FeCl_3$, and the floating graphene/P(VDF-TrFE) layer was thoroughly washed with DI water. After a mild RCA cleaning step, the graphene/P(VDF-TrFE) layers were transferred to a pre-patterned Si wafer using the conformal transfer technique, which delivered reproducible metal/graphene contacts with a device yield near unity.[37] The "ammonia" treatment was performed by placing the floated graphene/P(VDF-TrFE) film in a continuous flow bath of NH_3:DI water (1 M) for 30 min, as described in chapter 2. The layers were subsequently dried at 40 °C for 12 h in a vacuum oven at 10^{-1} mbar and then annealed at 140 °C for 2 h to enhance the crystallinity of the P(VDF-TrFE). The pre-patterned substrates were fabricated on 6-inch Si wafers with 250 nm of thermally grown SiO_2. The patterns included sets of (1) Fe-FET test structures with interdigitated structures with the channel length varying from 10 to 40 µm at a fixed channel width of 10000 µm and (2) circular transfer line test structures with electrode spacing varying from 1 to 40 µm at a fixed channel width of 1000 µm.[37] The electrodes were fabricated by sputter deposition of Ti/Au electrodes (2 nm/150 nm) and patterned by conventional photolithography. The SiO_2 surface was passivated with hexamethyldisilazane (HMDS) prior to conformal transfer of graphene/P(VDF-TrFE).

The sheet resistance of the graphene layer, before and after ammonia treatment, was determined using a four-point probe circular transfer line test method (CTLM), as detailed in the reference. [37] Constant current ranging from 1 to 100 µA was forced, and the voltage drop was recorded for different current levels (at zero gate voltage). The CTLM resistance data showed a linear dependence on electrode spacing. The extracted sheet and contact resistances were constant for different current levels.

The ferroelectric capacitors were fabricated by deposition of Cr/Au (1 nm/50 nm) onto thoroughly cleaned glass substrates. After deposition of the P(VDF-TrFE) or graphene/P(VDF-TrFE) layer on the substrates and subsequent annealing (140 °C, 2 h), 100 nm of the Au top contact was evaporated through a shadow mask. The P(VDF-TrFE) layer thickness was 1200 ± 60 nm. The capacitors had a device area varying from 0.2 to 4 mm^2.

Figure 3.1. a) P(VDF-TrFE) capacitor and the chemical structure of P(VDF-TrFE). b) to f) Schematic description of the fabrication process of the graphene Fe-FETs and MIS-diodes. b) P(VDF-TrFE) is coated on top of the CVD-grown graphene on Cu foils followed by Cu etching in c) and ammonia washing, d). The graphene layer is subsequently transferred using a conformal transfer onto a pre-patterned FET substrate e) or an Au-coated glass substrate for the MIS-diode f). The P(VDF-TrFE) layer serves as both the transfer layer and the gate dielectric.

The schematics of the capacitor and the graphene Fe-FET are presented in **Figure 3.1a-f**, respectively. All electrical measurements were performed in high vacuum (10^{-6} mbar) using a Sawyer–Tower circuit, a Keithley 4200 semiconductor characterization system, and a Keysight 4980 precision LCR meter.

3.3. Results and discussion

The displacement response of P(VDF-TrFE) capacitor to the electric field, the *D–E* loop, is given in **Figure 3.2**. The capacitors display the conventional *D–E* loop with a remanent polarization, P_r, and coercive field, E_c, that amount to 75 mC/m^2 and 60 MV/m, respectively.
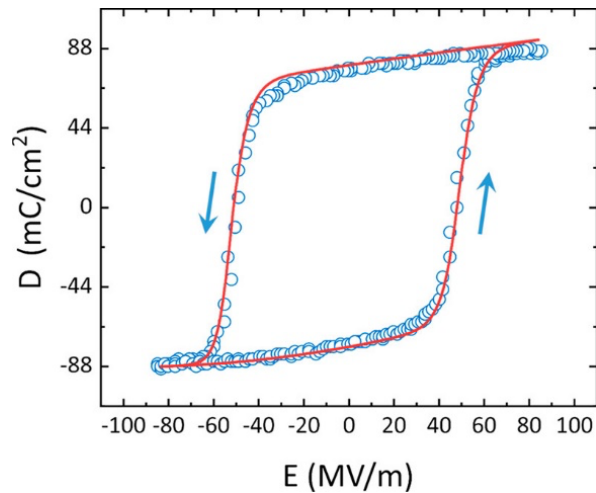
Figure 3.2. Displacement versus electric field for P(VDF-TrFE) ferroelectric capacitor (symbols) and the fit (solid line). The arrows show the direction of voltage sweep.

The sheet resistance, R_{sh}, of the CVD-graphene/P(VDF-TrFE) transferred from DI water (w-graphene), determined from the circular transmission line measurement (CTLM) test structures [37], amounts to 440 ± 5 Ω/□ and remains constant for a current level of 10^{-4} through to 10^{-2} A, indicating that the Au forms an Ohmic contact with the graphene layer. The contact resistance, R_c, is constant over the surveyed current range and amounts to 1.5 ± 0.2 kΩ·µm. The value of R_c is low and comparable to previously reported values. [37,44]
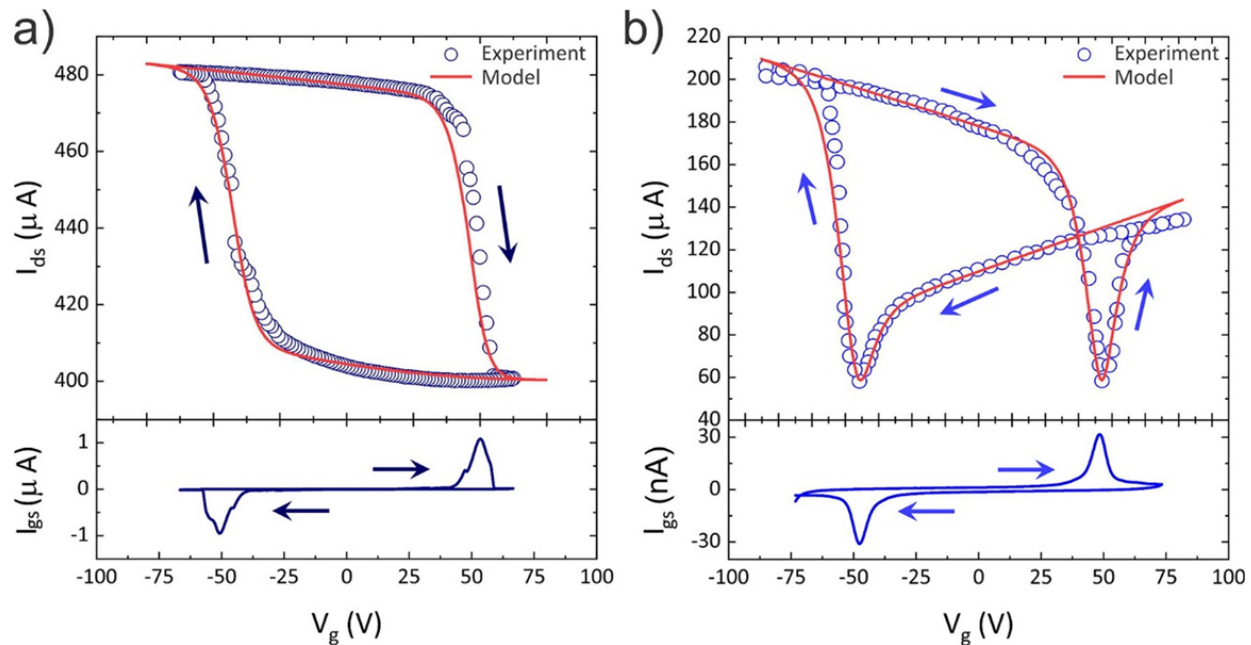
Figure 3.2. Transfer characteristics of graphene Fe-FETs fabricated a) using conventional transfer without an ammonia washing step and b) with an ammonia washing step. The arrows show the direction of voltage sweep.

The transfer characteristic of the Fe-FETs from the same batch of w-graphene/P(VDF-TrFE) is given in **Figure 3.3a**. The transfer characteristic is recorded by application of a small bias of +50 mV to the drain, and the drain current is monitored while changing the gate bias. Since the layer thickness of P(VDF-TrFE) is about 800 ± 50 nm, $V_G > |45|$ V is required to switch the polarization state. Qualitatively, the transfer characteristics can be understood as follows: The gate bias starts from 0 V and then reaches the coercive field of −50 MV/m ($V_G ≈ −50$ V). The gate current exhibits a displacement peak, and P(VDF-TrFE) switches polarization. The polarization vector points away from the graphene channel and induces a channel of accumulated holes in the graphene layer, which simultaneously stabilize the polarization. Upon back-sweeping of the gate bias toward positive values, P(VDF-TrFE) retains its polarization state. At $V_G ≈ +50$ V, the polarization direction of P(VDF-TrFE) switches and points toward the graphene layer. The switching is accompanied by a displacement peak in the gate current. The opposite polarization is then stabilized by formation of an electron accumulation layer in the graphene. However, in spite of the expected electron accumulation, the channel current remains low at the level of the residual or background current. Later, it will be demonstrated that negative polarization is stabilized partly by the negative compensation charges originating from ions instead of induced accumulated electrons. The observed behavior depicted in **Figure 3.3a** resembles the typical transfer characteristics of a Fe-FET with a unipolar p-type semiconductor channel.[39,41] The "seemingly" unipolar behavior of the graphene Fe-FET is attributed to the transfer process.[30] The presence of ions (originating from copper, water, or FeCl₃), which lead to unintentional doping of the CVD-graphene layer, must be avoided. For **Figure 3.3a**, negative doping counter-ions neutralize the ferroelectric polarization for positive gate biases, leading to a unipolar transfer characteristic.

The ambipolarity of the graphene Fe-FET is retrieved by washing the graphene/P(VDF-TrFE) layer in a 1 M ammonia flow bath, as described in chapter 2. The sheet and contact resistances of the graphene transferred after an extra ammonia washing step (hence, a-graphene) amount to 500 ± 5 Ω/□ and 1.5 ±

0.2 kΩ·µm, respectively, and remain constant for the current range varying over 2 orders of magnitude. Observation of a higher R_{sh} is due to the dedoping of the graphene layer.

We have estimated the number of ions removed from the graphene layer by performing capacitance–voltage (C–V) measurements on the Au/P(VDF-TrFE)/graphene MIS-diodes. The C–V responses of the MIS-diodes fabricated from w- and a-graphene, **Figure 3.4**, reveal the typical butterfly loop due to the field-dependent dielectric constant of the P(VDF-TrFE) layer. Observation of the full butterfly loop is a clear indication that both polarization states are stabilized. [38,39] The peaks in the capacitance coincide with the coercive bias of P(VDF-TrFE) layer. At −60 V, both MIS-diodes switch, and the polarization points away from the graphene layer. The polarization is stabilized by the formation of the hole accumulation layer in the graphene layer. For the positive bias, the MIS-diodes with a-graphene switch the polarization at +59 V, whereas w-graphene switches at +70 V. Now, the polarization direction points toward the graphene layer. The nearly perfect symmetry of the C–V response for the a-graphene MIS-diode suggests that the graphene layer is neutral, whereas the asymmetry in the coercive voltage of the MIS-diode with w-graphene indicates that negatively charged species exist between the Au bottom contact and the graphene layer. The interfacial charges screen the electric field at the interface such that a higher positive voltage is required to induce polarization reversal. From the difference in the positive coercive biases of the two MIS-diodes, the number of negatively charged species is estimated using $\Delta n = \frac{\varepsilon_0 \varepsilon_P A}{d} \frac{\Delta V}{e}$, where ΔV = 12.3 V is the observed shift, ε_P = 15 is the dielectric constant, d is the thickness of the P(VDF-TrFE) layer, and A is the area of the MIS-diode (ε_0 and e are vacuum permittivity and electron charge, respectively). An ion density of $\sim 3 \times 10^{12}$/cm^2 is obtained, which is very close to reported literature values.[43]
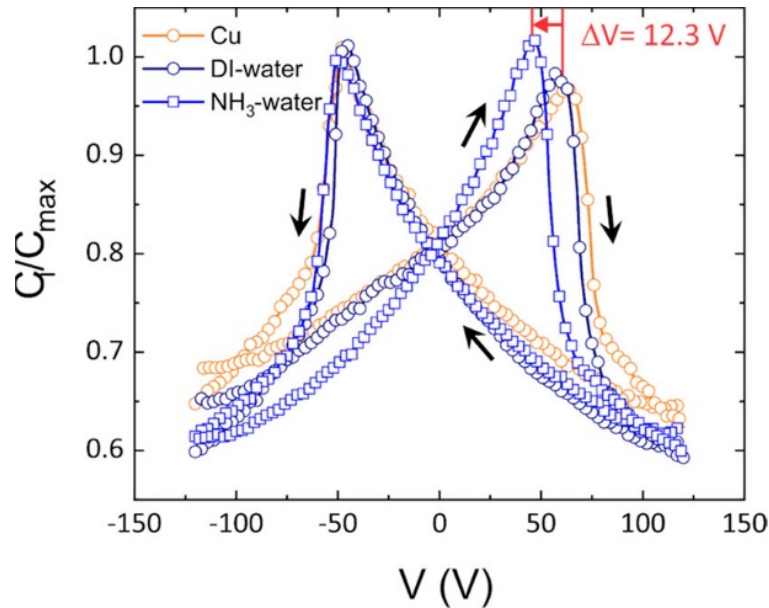
Figure 3.3. Capacitance–voltage (C–V) plot of graphene ferroelectric MIS-diodes for CVD-grown graphene on copper (orange symbols), conventionally transferred graphene from DI water (dark-blue symbols), and graphene washed with ammonia solution (light-blue symbols). The shift in the position of the right peak is due to removal of the ions. The arrows show the direction of voltage sweep.

The transfer characteristic of the Fe-FET fabricated from the same batch of a-graphene/P(VDF-TrFE) is given in **Figure 3.3b**. Application of −100 V to the gate brings the P(VDF-TrFE) to its full positive polarization, and the hole accumulated channel is formed. The hole current does not change substantially

upon sweeping the gate bias toward zero and then further to positive gate bias. At ~+50 V, the gate bias reaches +E_c, and the polarization direction switches. The reversed polarization state is fully compensated by the accumulated electrons, leading to formation of an electron channel. As the gate voltage increases toward +100 V, contrary to **Figure 3.3a**, the electron current prevails. Upon back-sweep of the gate bias to zero and further toward negative biases, the electron current persists. At ~−50 V, the gate bias reaches −E_c, P(VDF-TrFE) polarization switches back to the initial positive polarization state, and the hole current is retrieved. Appearance of both electron and hole channels in the graphene Fe-FET in **Figure 3.3b** clearly demonstrates recovery of the ambipolarity of the CVD-graphene layer by removal of the unintentional doping. The unbalanced transfer characteristics could be due to lower mobility of the electrons on the SiO₂ substrate.

3.4. Predictive modelling of graphene Fe-FETs

To answer the important question about the maximum achievable I_{on}/I_{off} ratio in a graphene Fe-FET, an analytical device model is developed, which integrates ferroelectric polarization of the gate layer, here P(VDF-TrFE), with the standard model that is used for graphene FETs. The description of the ferroelectric polarization loop in the model is generic and can be easily adopted for inorganic ferroelectrics. The displacement, *D*, of the ferroelectric layer is the sum of the linear dielectric response and the ferroelectric polarization as given by

$$D = \varepsilon_0 \varepsilon_P E + P(V, t) \tag{3.1}$$

where E and $P(E)$ are the electric field and ferroelectric polarization, respectively. It has been shown that the *D–E* loop of P(VDF-TrFE) ferroelectric capacitor [40,41] can well be described with an empirical analytical formula of the form:

$$P^+(E) = \varepsilon_0 \varepsilon_P E + {P_s}/{2} \left(tanh\left(\frac{E+E_c}{\delta}\right) + tanh\left(\frac{E-E_c}{\delta}\right) \right) \tag{3.2}$$

with

$$\delta = 2E_c \left[ln\left(\frac{1+P_r/P_S}{1-P_r/P_S}\right) \right]^{-1} \tag{3.3}$$

where *P⁺(E)* denotes the lower branch of the polarization loop going form negative bias and polarization toward the positive values. The negative branch, P⁻(E), is calculated using *P⁻(E) = −P⁺(− E)*. With a good accuracy, as presented in **Figure 3.2**, the empirical model fits the experimentally measured displacement loop using parameter values ε_P = 15, P_r = 75.09 mC/m², P_s = 75.1 mC/m², and E_c = 60 MV/m. The device characteristics correspond to typical values found for P(VDF-TrFE) capacitors.

In the graphene Fe-FET, the polarization of the ferroelectric gate depends only on the gate bias, since the voltage applied on the drain electrode is much smaller and can be neglected.[42] The gate field can therefore be assumed to be uniform in the channel region and given by

$$E = \frac{V_G - V_D}{t_P} \tag{3.4}$$

where t_p is the thickness of P(VDF-TrFE) gate layer, V_G is the gate bias, and V_D is Dirac voltage. The gate-bias-dependent polarization is calculated from equation **3.4**. Depending on the history and gate-bias scan

direction, the applicable description of the ferroelectric polarization, $P^\pm(V_G)$, is chosen. The effective gate bias experienced by the graphene layer is therefore

$$V_{eff} = V_G - V_D + \frac{P^\pm(V_G)}{C_P} \tag{3.5}$$

where $\frac{P^\pm(V_G)}{C_P}$ is the polarization-induced voltage, and C_p is the geometrical areal capacitance of the P(VDF-TrFE) gate layer in F/m^2. In equation **3.5**, it is assumed that that the remanent and saturated polarization of the ferroelectric gate dielectric in the Fe-FET are the same as those in the capacitor. Therefore, coupling of the ferroelectric polarization is 100%. Lower couplings can also be taken into account by introducing a coupling factor$= \alpha \times \frac{P^\pm(V_G)}{C_P}$. Furthermore, the MIS-diode measurements have suggested that both polarization states are stable, and depolarization can be ignored. Moreover, the polarization of the ferroelectric gate dielectric depends only on the gate bias, since the voltage applied on the drain electrode is much smaller and can be neglected.[42]

Introduction of the expression for the effective gate bias integrates the descriptions of ferroelectric polarization with the charge transport. The carrier concentration in the channel, n_{tot}, is obtained by

$$n_{tot} = \sqrt{n_0^2 + n(V_{eff})^2} \tag{3.6}$$

where n_0 represents the intrinsic density of carriers in the channel at the Dirac point, ($\sim 10^{12}$ cm^{-2}), and $n(V_{eff})$ is the of carrier density induced by the effective gate bias. To calculate the current, the value of $n(V_{eff})$ should be known. The physics of the 2D electrons in the graphene channel is taken into account by including the quantum capacitance, C_Q:

$$C_Q = \frac{2e^2\sqrt{n(V_G)}}{\hbar v_f \sqrt{\pi}} \tag{3.7}$$

where $\hbar$ is the reduced Planck's constant, and v_f is Fermi velocity of the carriers. Since C_P and C_Q are in series, V_{eff} can be written as

$$V_{eff} = \frac{e}{C_P} n(V_G) + \frac{e}{C_Q} n(V_G) \tag{3.8}$$

Rearrangement of equation **3.6** yields an analytical form for $n(V_{eff})$:

$$n(V_G) = \frac{C_P}{e}\left(V_{eff} + \frac{b^2}{2e}C_P - b\left(\frac{V_{eff}C_P}{e} + \frac{b^2}{4e^2}C_P^2\right)^{1/2}\right) \tag{3.9}$$

where $b = \frac{\hbar v_f \sqrt{\pi}}{2e}$ and the total resistance of the device can be determined as

$$R_{tot}(V_G) = R_c + \frac{N_{sq}}{\mu_e\sqrt{n_0^2 + n(V_G)^2}} \tag{3.10}$$

where R_c, N_{sq}, and μ are, respectively, contact resistance of the metal–graphene junction, number of squares of the gated area, and charge carrier mobility of the graphene layer. The drain–source current, I_{ds}, at any given gate bias is

$$I_{ds} = \frac{V_{ds}}{R_{tot}} \tag{3.11}$$

Analytically calculated transfer curves are presented in **Figure 3.3a-b** for both graphene Fe-FETs with and without the NH_3 washing step. The parameters obtained for P(VDF-TrFE) from the fit using equation **3.5** are fixed and used as input for the calculation. The only variable parameters to fit the curves are μ and V_D. For simplicity, a constant mobility for the graphene layer is considered. The calculated current, presented by the solid red curve for each case, describes the experimental transfer curves with good accuracy. For the case of the graphene Fe-FET without the ammonia washing step, the best fit to the experimental curves gives V_D = 675 V and μ = 600 cm²/(V·s). For the sample with the ammonia washing step, V_D = 250 V and $μ$ = 400 cm²/(V·s). Equation **3.6** also gives a calculated value of Δn = 3.9 × 10¹² cm⁻², which is very close to the experimentally determined doping value using MIS-diodes, indicating internal consistency of the model. Ammonia treatment of graphene/P(VDF-TrFE) removes traces of dopants (or charge species), shifts the Dirac voltage back to much lower values, and removes the "seemingly" unipolar behavior.

Following the validation, the model can now be used to provide guidelines to improve Fe-FET memory performance. Different parameters of the graphene layer are varied to find out the best operational conditions for the Fe-FETs. An important figure-of-merit for Fe-FET memories is current modulation, or I_{on}/I_{off} ratio, which is defined as the ratio of the drain–source current for the two polarization states of P(VDF-TrFE) at V_G = 0 V. For memory applications, a high I_{on}/I_{off} ratio is desired. First, an ideal and perfect graphene layer with V_D = 0 V is considered. The calculated transfer characteristics are given in **Figure 3.5 a**. Such Fe-FETs show I_{on}/I_{off} = 1. Similar transfer characteristics with a unity I_{on}/I_{off} have been reported for mechanically exfoliated graphene gated with P(VDF-TrFE). However, a unity I_{on}/I_{off} renders defect- and dopant-free graphene impractical for memory applications. The I_{on}/I_{off} ratio is calculated for different parameters for the graphene layer V_D and $μ$, while the ferroelectric parameters (P(VDF-TrFE) in our case) are kept fixed at values obtained from **Figure 3.2** for the capacitors. **Figure 3.5b** presents the I_{on}/I_{off} ratio map for different mobilities and Dirac voltages. It is found that for a fixed Dirac bias, I_{on}/I_{off} is insensitive to the change in mobility for a wide range from 10⁻² to 10⁵ cm²/V·s, whereas for a fixed mobility, I_{on}/I_{off} changes with the Dirac bias. A perfect graphene layer with V_D = 0 V gives an I_{on}/I_{off} = 1, regardless of the mobility. Interestingly, an imperfect graphene layer that is slightly doped, i.e., V_D ≠ 0, is better suited, because the Fe-FETs show I_{on}/I_{off} > 1. For the largest I_{on}/I_{off}, V_D or alternatively the background doping in the graphene layer should be in the range of 350 to 550 V. Such values for V_D can be translated to background doping density that is comparable to the remanent polarization of the ferroelectric layer. Therefore, for the best performing graphene Fe-FET, the background doping density should be comparable with the remanent polarization of the ferroelectric layer (here P(VDF-TrFE)). Interestingly, the I_{on}/I_{off} for the optimal V_D range is less sensitive to the mobility of the charge carriers, since an I_{on}/I_{off} of 2.4 is obtained for the mobility range of 10⁻¹ to 10⁵ cm²/V·s.
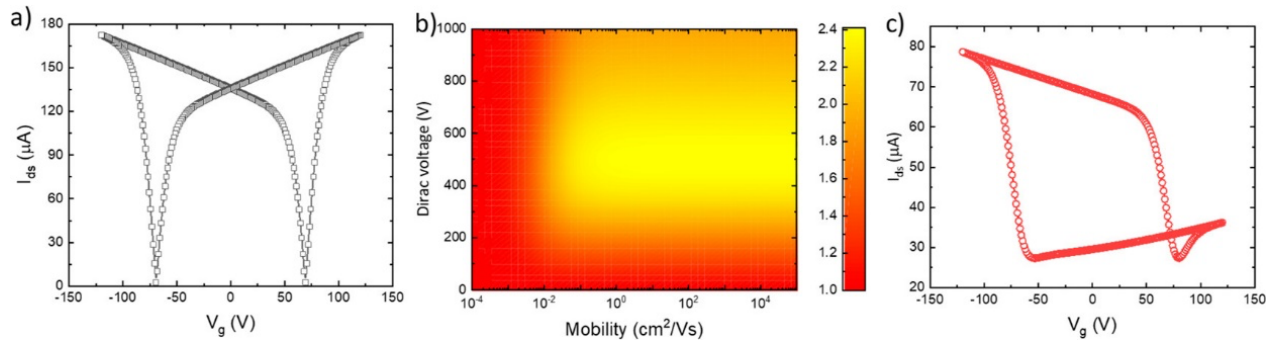
Figure 3.5. Theoretical prediction of the model. a) Transfer characteristics of ideal graphene with a Dirac point at 0 V. b) the color map of the calculated I_{on}/I_{off} ratio at $V_G = 0$ for Dirac biases and mobilities. c) Transfer characteristics of a graphene Fe-FET with the largest on/off ratio of 2.40. For all cases, the contact resistance is 50 Ω. For cases a and b, a constant mobility of 400 cm^2/V·s for the graphene layer is used.

Reference

1) Y. J. Doh, G. C. Yi, *Nanotechnology* 2010, **21**, 105204.
2) I. Jung, J. Y. Son, *Carbon* 2012, **50**, 3854– 3858.
3) H.S. Lee, S. W. Min, M. K. Park, Y. T. Lee, P. J. Jeon, J. H. Kim, S. Ryu, *Small* 2012, **8**, 3111– 3115.
4) Y. T. Lee, D. K. Hwang, W. K. Choi, *J. Korean Phys. Soc.* 2016, **69**, 1347– 1351.
5) G.D. Belletti, S.D. Dalosto, S. Tinte, *J. Phys.: Condens. Matter* 2016, **28**, 435002.
6) Y. Chen, X. Wang, P. Wang, H. Huang, G. Wu, B. Tian, Z. Hong, Y. Wang, S. Sun, H. Shen, J. Wang, W. Hu, J. Sun, X. Meng, J. Chu, *ACS Appl. Mater. Interfaces* 2016, **8**, 32083– 32088.
7) X. Wang, C. Liu, Y. Chen, G. Wu, X. Yan, H. Huang, P. Wang, B. Tian, Z. Hong, Y. Wang, S. Sun, H. Shen, T. Lin, W. Hu, M. Tang, P. Zhou, J. Wang, J. Sun, X. Meng, J. Chu, Z. Li, *2D Mater.* 2017, **4**, 025036.
8) C. Yin, X.Wang, Y. Chen, D. Li, T. Lin, S. Sun, H. Shen, P. Du, J. Sun, X. Meng, J. Chu, H. F. Wong, C. W. Leung, Z. Wang, J. Wang, *Nanoscale* 2018, **10**, 1727– 1734.
9) D. Li, X. Wang, Y. Chen, S. Zhu, F. Gong, G. Wu, C. Meng, L. Liu, L. Wang, T. Lin, S. Sun, H. Shen, X. Wang, W. Hu, J. Wang, J. Sun, X. Meng, J. Chu, Nanotechnology 2018, **29**, 105202.
10) H. J. Hwang, J. H. Yang, Y. G. Lee, C. Cho, C. G. Kang, S. C. Kang, W. Park, B. H. Lee, *Nanotechnology* 2013, **24**, 175202.
11) H. Zhang, Y. Chen, S. Ding, J. Wang, W. Bao, D. W. Zhang, P. Zhou, *Nanotechnology* 2018, **29**, 244004.
12) F. A. McGuire, Y. C. Lin, K. Price, G. B. Rayner, S. Khandelwal, S. Salahuddin, A. D. Franklin, *Nano Lett.* 2017, **17**, 4801– 4806.
13) D. Jin, A. Kumar, K. Hung Fung, J. Xu, N. X. Fang, *Appl. Phys. Lett.* 2013, **102**, 201118.
14) X. Wang, P. Wang, J. Wang, W. Hu, X. Zhou, N. Guo, H. Huang, S. Sun, H. Shen, T. Lin, M. Tang, L. Liao, A. Jiang, J. Sun, X. Meng, X. Chen, W. Lu, J. Chu, *Adv. Mater.* 2015, **27**, 6575– 6581.
15) C. Baeumer, D. Saldana-Greco, J. M. P. Martirez, A. M. Rappe, M. Shim, L. W. Martin, *Nat. Commun.* 2015, **6**, 6136.
16) Y. Zheng, G. X. Ni, C. T. Toh, M. G. Zeng, S. T. Chen, K. Yao, B. Özyilmaz, *Appl. Phys. Lett.* 2009, **94**, 163505.
17) Y. L. Lee, S. Kim, C. Park, J. Ihm, Y. W. Son, *ACS Nano* 2010, **4**, 1345– 1350.
18) Y. Zheng, G.-X. Ni, C.-T. Toh, C.-Y. Tan, K. Yao, B. Özyilmaz, *Phys. Rev. Lett.* 2010, **105**, 166602.
19) S. Raghavan, I. Stolichnov, N. Setter, J. S. Heron, M. Tosun, A. Kis *Appl. Phys. Lett.* 2012, **100**, 023507.
20) S. Lee, Y. Lee, *Carbon* 2018, **126**, 176 – 182.
21) M. Dragoman, M. Modreanu, I. M. Povey, A. Dinescu, D. Dragoman, A. Di Donato, E. Pavoni, M. Farina, *Nanotechnology* 2018, **29**, 425204.
22) M. Zhu, J. Wu, Z. Du, R. Y. Tay, H. Li, B. Özyilmaz, E. H. T. Teo, *Nanoscale* 2015, **7**, 14730– 14737.
23) Y. Zheng, G.-X. Ni, S. Bae, C.-X. Cong, O. Kahya, C.-T. Toh, H. R. Kim, D. Im, T. Yu, J. H. Ahn, B. H. Hong, B. Özyilmaz, EPL 2011, **93**, 17002.
24) W. Lee, O. Kahya, C. T. Toh, B. Özyilmaz, J. H. Ahn *Nanotechnology* 2013, **24**, 475202.
25) Ni, G. X.; Zheng, Y.; Bae, S.; Tan, C. Y.; Kahya, O.; Wu, J.; Hong, B. H.; Yao, K.; Özyilmaz, B. *ACS Nano* 2012, **6**, 3935– 3942.
26) X. Wang, M. Tang, Y. Chen, G. Wu, H. Huang, X. Zhao, B. Tian, J. Wang, S. Sun, H. Shen, T. Lin, J. Sun, X. Meng, J. Chu *Opt. Quantum Electron.* 2016, **48**, 345.
27) J. Heidler, S. Yang, X. Feng, K. Müllen, , K. Asadi, *Solid-State Electron.* 2018, 144, 90– 94.
28) A. Rajapitamahuni, J. Hoffman, C. H. Ahn, X. Hong, *Nano Lett.* 2013, **13**, 4374– 4379.
29) E. B. Song, B. Lian, S. M. Kim, S. Lee, T.-K. Chung, M. Wang, C. Zeng, G. Xu, K. Wong, Y. Zhou, H. I. Rasool, D. H. Seo, H.-J. Chung, J. Heo, S. Seo, K. L. Wang, *Appl. Phys. Lett.* 2011, **99**, 042109.
30) H. Wang, Y. Wu, C. Cong, J. Shang, T. Yu, *ACS Nano* 2010, **4**, 7221– 7228.
31) J. F. Scott, *Science* 2007, **315**, 954– 959.
32) P. Zubko, D. J. Jung, J. F. Scott, *J. Appl. Phys.* 2006, **100**, 114112.

33) M. H. Yusuf, B. Nielsen, M. Dawber, X. Du *Nano Lett*. 2014, **14**, 5437– 5444.

34) W. Jie , J. Hao, *Nanoscale* 2018, **10**, 328– 335.

35) Y. L. Sun, D. Xie, J. L. Xu, X. M. Li, C. Zhang, R. X. Dai, X. Li, X. J. Meng, H. W. Zhu, *Carbon* 2016, **96**, 695– 700.

36) R. C. G. Naber, K. Asadi, P. W. M. Blom, D. M. De Leeuw, B. De Boer *Adv. Mater.* 2010, **22**, 933– 945.

37) K. Asadi, E. C. Timmering, T. C. T. Geuns, A. Pesquera, A. Centeno, A. Zurutuza, J. H. Klootwijk, P. W. M. Blom, D. M. de Leeuw, *ACS Appl. Mater. Interfaces* 2015, **7**, 9429– 9435.

38) Li, M.; Katsouras, I.; Asadi, K.; Blom, P. W. M.; de Leeuw, D. M. *Appl. Phys. Lett.* 2013, **103**, 072903.

39) R.C.G. Naber, J. Massolt, M. Spijkman, K. Asadi, P.W.M. Blom, D.M. De Leeuw, *Appl. Phys. Lett.* 2007, **90**, 113509.

40) S.L. Miller, J. R. Schwank, R. D. Nasby, M. S. Rodgers, *J. Appl. Phys.* 1991, **70**, 2849– 2860.

41) J. J. Brondijk, K. Asadi, P. W. M. Blom, D. M. de Leeuw, J. *Polym. Sci., Part B: Polym. Phys.* 2012, **50**, 47– 54.

42) K. Asadi, P. W. M. Blom, D. M. De Leeuw *Appl. Phys. Lett.* 2011, **99**, 053306.

43) S. Kim, J. Nah, I. Jo, D. Shahrjerdi, L. Colombo, Z. Yao, E. Tutuc, S. Banerjee, *Appl. Phys. Lett.* 2009, **94**, 062107.

44) F. Xia, V. Perebeinos, Y. M. Lin, Y. Wu, P. Avouris, Nat. *Nanotechnol.* 2011, **6**, 179– 18.

Chapter 4

Designing Multi-Level Resistance States in Graphene Ferroelectric Transistors

Abstract

Conventional memory elements encode information in the Boolean "0" and "1" form. Devices that exceed bi-stability in their resistance are useful as memory for future data storage due to their enhanced memory capacity, and are also a necessity for contemporary applications such as neuromorphic computing. In this chapter, with the aid of the device model developed in Chapter 3, design rules for a multibit ferroelectric memory are outlined and more than two stable resistance states in a graphene ferroelectric field-effect transistor are experimentally demonstrated. The design methodology can be extrapolated for on-demand introduction of multiple resistance states in ferroelectric transistors for applications both in data storage and neuromorphic computing. The proposed device model is ready to be employed for the design of multiferroic field-effect transistors, by introduction of magnetization in the description of the gate dielectric.

4.1. Introduction

As demonstrated in the previous chapter, resistance switching in 2D-material-based ferroelectric field-effect transistors (Fe-FETs)[1] is achieved by modulation of charge carrier density and thereby conductance of the 2D material by polarization of the ferroelectric gate insulator.[2-10] The binary states, "0" and "1," are programmed by switching from one polarization state to the other by applying a bias that exceeds the coercive bias, V_C, of the ferroelectric gate insulator.[20-23] Graphene was used as the channel semiconductor material because it has been the workhorse of the 2D material family. Demonstration of wafer-level upscaling of graphene Fe-FETs,[13-19] on flexible foils,[23-27] and even fully solution-processed graphene Fe-FETs[19] has supported the proposed application of 2D materials for high-speed nonvolatile memories.[11, 12]

The conventional Fe-FETs have a Boolean "0" and "1" output. [28-30] The binary system is simple but offers limited data storage capacity as every bit of information (0 and 1) is translated to one of the two possible states. Multi-valued storage devices have been proposed to alleviate the limited storage capacity of the binary devices. [31, 32] For instance, in a quaternary memory, the information is coded into one of the four possible states of 0, 1, 2, and 3 that together represent the information of two binary bits and are represented by 00, 01, 10, and 11, respectively. In comparison, for a 16 × 16-bit array, the binary system offers 256 bits, offering 2^{256} possible states, while at the same time, the quaternary system offers 4^{256} (or $(2^2)^{256}$) possible states. A quaternary graphene Fe-FET would require four different conductance levels at zero gate bias. Despite the technological promise, multi-bit 2D material Fe-FETs have not been extensively studied. [12, 32, 33]

Memory devices also play central role in the hardware-based implementation of artificial neural networks (ANNs).[45] The figure of merit in this hardware-based approach is the mapping of the coupling between neurons that are found in biology (also known as synaptic weight) in the device memory state.[46] This synaptic weight is usually regarded as a continuous variable in biology, and therefore it is more biologically realistic to be emulated with analogue memory devices.[47] It is now well-known that core functions of ANNs, such as vector-matrix-multiplication, can be implemented on a crossbar array of analogue memory devices.[47-50] Despite the fact that nowadays research is quite intense in the field of analogue memory devices for synaptic electronics, the representation of synaptic weight with lower precision (*i.e.*, few bit-memory) is still a viable route for the implementation of ANNs.[51, 52] This approach represents a trade-off between precision in synaptic weight mapping and data volume during transfer,[49] and even allows for the potential implementation of hardware-based ANNs with devices that lack intrinsic analogue memory phenomena. Among other devices, a few examples of 2D or semiconductor Fe-FETs that exhibit gradual modulation of resistance have been reported in the past. [53-56] However, specific design principles for on-demand introduction of the number of states in Fe-FETs based on the needs of a specific application have not been reported yet.

This chapter presents the design and experimental demonstration of graphene Fe-FETs with four resistance states (quaternary) and generalizes the design to exceed four states in a graphene Fe-FET. The Fe-FETs are realized with graphene grown from chemical vapor deposition (CVD) technique that are gated with a ferroelectric polymer poly (vinylidene fluoride-co-trifluoroethylene) (P(VDF-TrFE)). The methodology developed can be used for any combination of 2D materials with both organic and inorganic ferroelectrics, provided that the correct material description is taken into consideration. The methodology allows for developing memory cells with multiple number of states that are predefined through design. The results provide valuable guidelines for realization of multi-level ferroelectric transistors for applications ranging from data storage to neuromorphic computing.

4.2. Experimental

CVD graphene grown on copper (Graphenea) was coated with P(VDF-TrFE) (65–35% mole %) (Solvay). A layer of P(VDF-TrFE), with thickness of 800–1500 nm, was spin-coated onto the graphene-coated copper foil from a 10 wt% methyl ethyl ketone (Sigma-Aldrich) solution. Doping-free transfer of the graphene was done according as described in chapter 2. [58] The graphene layer on the uncoated copper surface was removed by oxygen plasma. After etching Cu in 1 M aqueous bath of $FeCl_3$, the floated graphene/P(VDF-TrFE) layer was thoroughly washed using deionized (DI) water and a continuous flow bath of NH_3:DI-water (1 M) for 30 min. Subsequently, the graphene/P(VDF-TrFE) layer was transferred on to the pre-patterned FET substrate using the conformal transfer technique. The interdigitated Ti/Au (2 nm/150 nm) source-drain electrodes with a fixed channel width of 10 000 µm and a varying channel length of 10–40 µm, **Figure 4.1d** were fabricated by conventional photolithography on 6 inches Si wafers with 250 nm hexamethyldisilazane-passivated, thermally grown SiO_2.
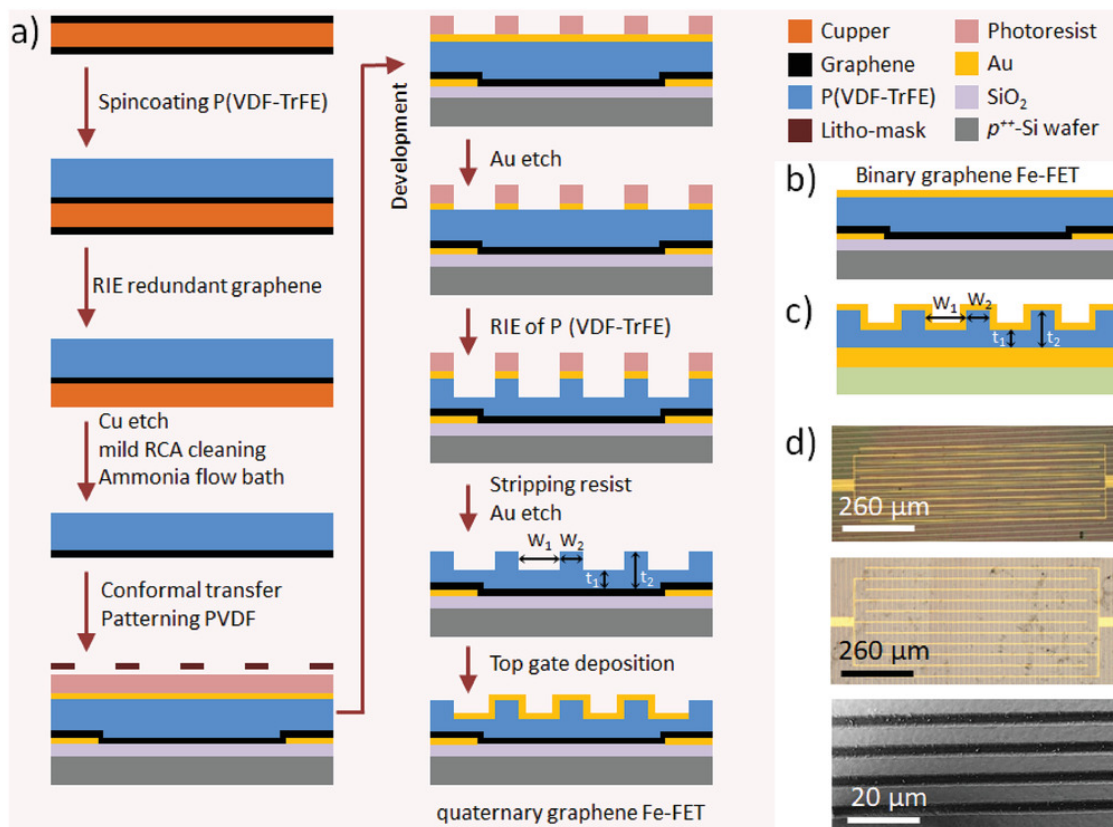
Figure 4.1. a) Process flowchart of quaternary graphene Fe-FETs. b) Schematic of a conventional binary graphene Fe-FET. c) Cross-sectional schematics of the patterned P(VDF-TrFE) capacitors. d) Optical photograph of the graphene/P(VFD-TrFE) layer that is transferred on to prefabricated interdigitated Au electrodes with (top) pattern parallel and (middle) perpendicular to the graphene channel. Bottom: SEM image of the patterned P(VDF-TrFE) layer.

The stack was dried at 40 °C for 12 hours in a vacuum oven at 1 mbar, and then annealed at 140 °C for 2 hours to enhance crystallinity of the P(VDF-TrFE) layer. The fabrication process of Fe-FET was completed by evaporation of a 100 nm gold top gate electrode through a shadow mask. Patterned P(VDF-TrFE) layers for capacitors and gate structures, **Figure 4.1c**, were realized by performing an additional photolithography step. A layer of Au was deposited onto the P(VDF-TrFE) film and patterned. The

underlying Au electrode lines were used as a cue for the alignment of the top patterns. It was noted that a slight misalignment of the etching lines with the Au contact lines would not affect the experimental observation. For a down-scaled device, proper alignment of the pattern with the electrodes is required. Patterns parallel and perpendicular to the graphene channel, as shown in **Figure 4.1d**, were realized. The exposed Au stripes were etched in $KI/I_2/H_2O$ (4:1:4) solution. Subsequently, the exposed P(VDF-TrFE) was etched using reactive ion etching (RIE) with a plasma power of 150 W, at a pressure of 0.08 mbar, and Oxygen/Argon flow of 30/10 sccm (etching rate of 330 nm s^{-1}). The etching depth was controlled by the RIE etching time. Note that the etching rate was chosen due to the large thickness of the P(VDF-TrFE) layer. For thinner P(VDF-TrFE) films, required in applications, the etching rate should be substantially lower to allow for good control of the etching depth. After the etching process, the redundant photoresist and Au cover layer were stripped and etched, and the substrates were thoroughly rinsed in DI water. The photoresist was removed after the RIE process because the resist remover solvent dissolves the P(VDF-TrFE) layer. Patterned graphene Fe-FETs and capacitors were finalized by evaporation of a top Au electrode (150 nm). The flow chart of the fabrication process is given in **Figure 4.1a**. Trenches are patterned parallel to the interdigitated electrodes as shown in **Figure 4.1d**. All electrical measurements were performed in high vacuum (10^{-6} mbar) using a Keithley 4200 semiconductor characterization system. The Fe-FET measurements were performed by application of a small bias of +50 mV to the drain, and the drain current was monitored while changing the gate bias. The retention measurements of the programmed states in Fe-FETs were performed at zero gate bias while a bias of +50 mV was applied to the drain.

4.2.1 Multi-Bit Graphene Memory through Design

An analytical model was previously developed that coupled voltage-dependent charge displacement of the ferroelectric gate layer with the charge transport across the graphene channel.[57] To extend the formalism to multi-bit graphene Fe-FET, the geometrical topography was incorporated in the charge displacement description of the ferroelectric gate layer. The displacement, D, of a ferroelectric gate layer with a constant thickness, t, is the sum of the linear dielectric response and the ferroelectric polarization and is given by

$$D = \varepsilon_0 \varepsilon_P E + P(V,t) \tag{4.1}$$

Where $E(= V/t)$ and $P(V)$ are the electric field and ferroelectric polarization, respectively. Voltage-dependent polarization of the ferroelectrics can be described phenomenologically using the description introduced in chapter 3:

$$P^+(V,t) = \varepsilon_0 \varepsilon_P \frac{V}{t} + \frac{P_2}{2} f(V,t) \tag{4.2}$$

with

$$f(V,t) = \left(tanh\left(\frac{V+V_c}{t.\delta}\right) + tanh\left(\frac{V-V_c}{t.\delta}\right) \right) \tag{4.3}$$

and

$$\delta = 2\frac{V_c}{t}\left[ln\left(\frac{1+P_r/P_S}{1-P_r/P_S}\right) \right]^{-1} \tag{4.4}$$

where V_c, P_S, and P_r are the coercive bias, saturation polarization, and remanent polarization of the ferroelectric layer, respectively. The $P^+(V)$ functional denotes the lower branch of the polarization loop, going from negative bias and polarization towards the positive values. The negative branch, $P^-(V)$, is calculated using $P^-(V) = -P^+(-V)$.[35, 36] Equation **4.2** describes the *D–V* loop of an unpatterned P(VDF-TrFE) ferroelectric capacitor with a good accuracy, as shown in **Figure 4.2 a**. [39-44] The best fit is obtained

using the following parameter values: $\varepsilon_P = 15$, $P_r = 75.09$ mC.m^{-2}, $P_r = 75.1$ mC.m^{-2}, and $E_c = (V_c/t) = 60$ MV m^{-1}, which are the typical, experimentally reposted values for P(VDF-TrFE).
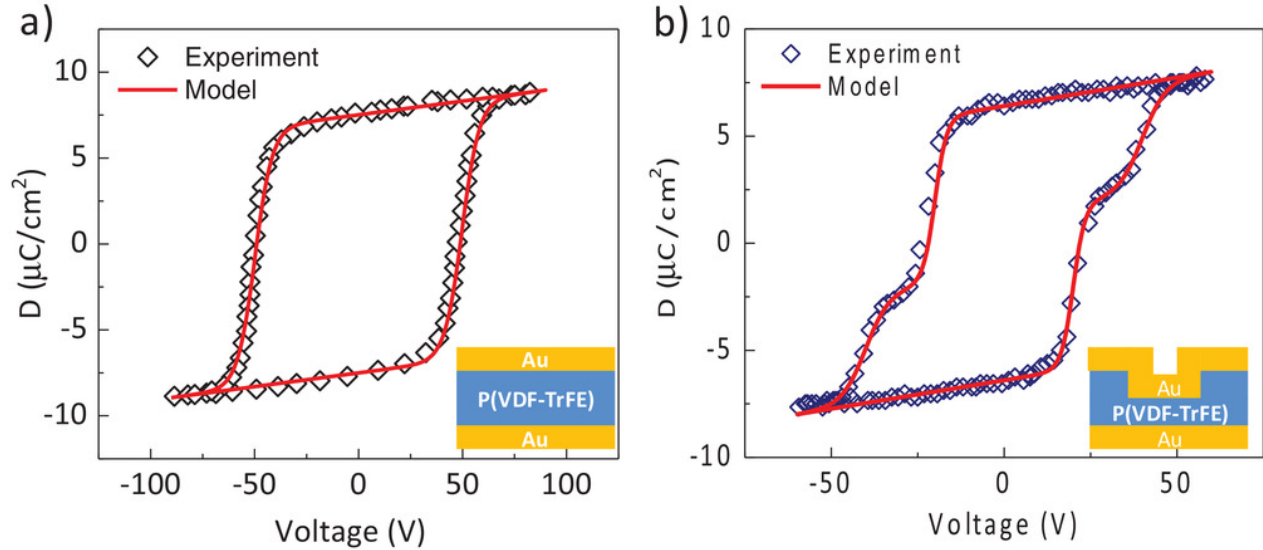
Figure 4.2. D–V loop of ferroelectric capacitors (insets) with a) a uniform and b) patterned P(VDF-TrFE) films. The solid red lines show the fits produced by the phenomenological model.

Writing the $P(V)$ functional in terms of voltage allows for generalizing the formalism for the patterned P(VDF-TrFE) capacitor as follows

$$P^+(V) = \sum_{i=1,2}\left(W_i \times P(V_i, t_i)\right) \qquad (4.5)$$

where W_i and t_i are areal fraction and thickness (nm) of the respective fraction of the patterned P(VDF-TrFE) film, as schematically shown in **Figure 4.1 c**. Capacitors with various fractional areas were tested. Representative experimental D–V loop of a capacitor with $W_1 = 0.25$ and $W_1 = 0.75$ is shown in **Figure 4.2b**. Using Equation **4.5** and the parameters resulting from the fit to **Figure 4.2 a**, combined with the geometrical parameters of $(W_1, t_1) = (0.25, 400$ (nm)) and $(W_2, t_2) = (0.75, 800$ (nm)), a good description of the D–V loop was obtained for the patterned P(VDF-TrFE) capacitor as shown in **Figure 4.2b**. The polarization of the ferroelectric gate layer changes the effective gate bias experienced by the graphene layer

$$V_{eff} = V_G - V_D + \frac{P^\pm(V_G)}{C_P} \qquad (4.6)$$

where V_G and V_D represent gate and Dirac voltage, respectively, $\frac{P^\pm(V_G)}{C_P}$ is the polarization-induced voltage, and C_P is the geometrical areal capacitance of the P(VDF-TrFE) gate layer in F.m^{-2}. Assuming that the remanent and saturated polarization of the ferroelectric gate in Fe-FET remains the same as those in the capacitor, and 100% coupling of the ferroelectric polarization with channel conductance, hence ignoring depolarization,[37] the gate bias-dependent carrier density can be written as

$$n(V_G) = \frac{C_P}{e}\left(V_{eff} + \frac{b^2}{2e}C_P - b\left(\frac{V_{eff}C_P}{e} + \frac{b^2}{4e^2}C_P^2\right)^{1/2}\right) \qquad (4.7)$$

where $b = \frac{\hbar v_f \sqrt{\pi}}{2e}$ appears due to taking into account the quantum capacitance of the graphene layer, $(2e^2\sqrt{n(V_G)}/(\hbar v_f \sqrt{\pi}))$ with $\hbar$ and v_f are reduced Plank's constant and Fermi velocity of the carriers, respectively. The source-drain current, I_{ds}, in the graphene Fe-FET is then given by

$$I_{ds}(V_G) = V_{ds} \times \left(R_c + N_{sq}\left(\mu e \sqrt{n_0^2 + n(V_G)^2}\right)^{-1}\right)^{-1} \qquad (4.8)$$

where R_c, N_{sq}, and μ are contact resistance of the metal–graphene junction, number of squares of the gated area, and charge carrier mobility of the graphene layer, respectively.

The model was experimentally validated by fitting the transfer curves for the graphene Fe-FETs with a plane, unpatterned P(VDF-TrFE) gate layer. The parameters obtained from the fits of the *D–V* loops of the P(VDF-TrFE) capacitor, **Figure 4.2 a**, were used as the input parameters for the gate layer of the Fe-FETs. The model accurately describes the transfer characteristics of the graphene Fe-FET with constant mobility of μ = 800 cm^2 V^{-1} s^{-1}, and V_D = 285 V, as shown in **Figure 4.3**. The model describes well the Fe-FETs with unpatterned gate, and is therefore experimentally validated.
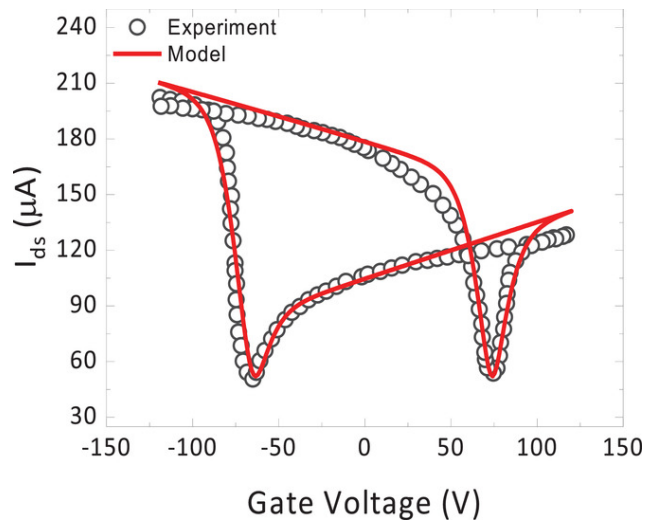
Figure 4.3. Transfer characteristics of a graphene Fe-FET with unpatterned plane P(VDF-TrFE) gate layer. The solid line shows the fit obtained using the analytical device model.

Based on the model, the operation of the graphene Fe-FET with a plane, unpatterned ferroelectric layer can now be accurately explained. Application of −125 V to the gate sets the P(VDF-TrFE) gate to its full positive polarization state, which is accompanied by accumulation of holes in the graphene channel. The hole current is persistent upon sweeping the gate bias toward zero and then further to positive gate bias. At about +75 V, the gate bias reaches $+E_c$, and P(VDF-TrFE) reverses its polarization. The negative polarization state is fully compensated by electron accumulation in the graphene channel, and the electron current prevails as the gate voltage increases further toward +125 V. The electron current persists upon sweeping back the gate bias to zero and down towards negative biases. At nearly −75 V, the gate bias reaches $-E_c$, and the polarization of the P(VDF-TrFE) gate layer switches back to the initial positive polarization state, re-establishing the hole current. The presence of both electron and hole channels in the graphene Fe-FET is due to the ambipolarity of the CVD-graphene layer by removal of the unintentional doping. [58]

Following the experimental validation, the model is used to make predictions for Fe-FETs with patterned gates. To produce transfer curves, the parameters that are obtained for the graphene Fe-FET with un-patterned P(VDF-TrFE) gate are used. The transfer characteristics are calculated for the patterned structure perpendicular to the graphene channel by varying the factional area of W_1 (and W_2) from 0 to 0.50. A representative calculated D–V loop is given in **Figure 4.2b** for W_1 = 0.25 and W_2 = 0.75. The calculated transfer characteristics of the comprising graphene Fe-FETs with the same patterned P(VDF-TrFE) are shown in **Figure 4.4a**. The Fe-FET clearly shows four different conductance levels depending on the polarization configuration of the patterned gate layer. Due to the ambipolarity of the graphene layer,

the intermediate polarization states are compensated and therefore stable in time, hence no depolarization of the gate layer is expected. [32, 34]
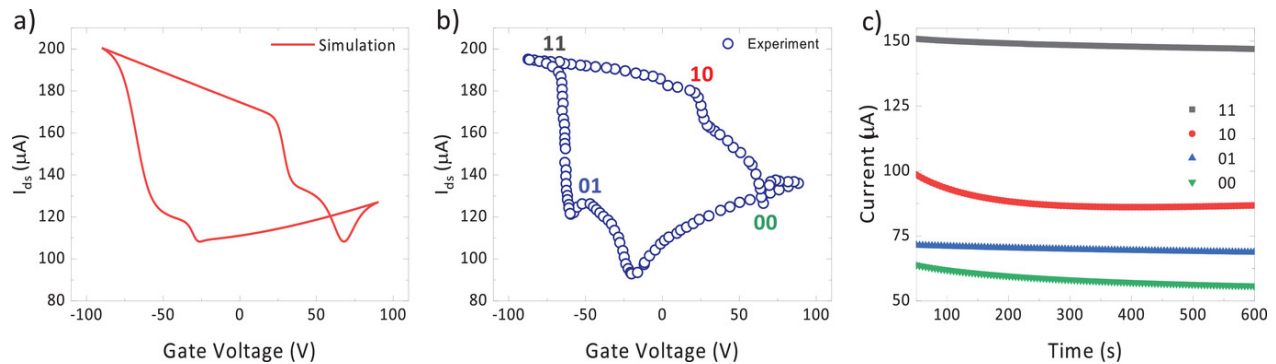
Figure 4.4. a) Model prediction of the quaternary graphene Fe-FET and b) experimental demonstration of the same device using a patterned P(VDF-TrFE) ferroelectric gate. c) Retention time of different states of the quaternary graphene Fe-FET measured at zero gate bias and a drain bias of +50 mV.

The experimental transfer characteristics of the graphene Fe-FETs with patterned P(VDF-TrFE) perpendicular to the graphene channel is shown in **Figure 4.4b**. The P(VDF-TrFE) layer has the same pattern (W_1 = 0.25 and W_2 = 0.75) with a thickness of t_1 = 600 nm and t_2 = 1200 nm, respectively. Application of negative gate bias of −90 V sets the patterned P(VDF-TrFE) layer in the fully positive polarization state, and hole accumulation is formed in the graphene layer. Upon sweeping the gate bias towards positive biases, the drain current shows a sudden drop at a gate bias of ≈+30 V. The thin part of the P(VDF-TrFE) gate layer is now in negative polarization state. As gate bias approaches nearly +60 V, the thick part of the P(VDF-TrFE) layer is now in positive polarization state, and therefore the P(VDF-TrFE) layer is homogeneously in positive polarization. As a result, a uniform electron accumulation channel is formed in the graphene layer. Upon back sweeping the gate bias, the electron current persists. At a gate bias of ≈−30 V, the hole accumulation channel is partly retrieved. At gate bias −60 V, P(VDF-TrFE) gate layer is again in full negative polarization. The Fe-FET, depending on the programming of the gate layer, shows four different conductance levels that are stable in time as shown in **Figure 4.4c**, in the absence of the external gate bias. Therefore, the graphene Fe-FET has a quaternary output.

The Fe-FETs with parallel alignment of the pattern with respect to the graphene channel have shown similar transfer characteristics. A parallel alignment would yield series connection of the channel portions, where the highest resistive portion of the channel would dominate the transfer characteristics. The perpendicular alignment would produce channels that are connected in parallel, and where the currents add up. In the case of graphene, the difference between the high and low resistance states, as shown in **Figure 4.3**, is a factor of two, which apparently is not large enough to yield different transfer characteristics. Dissimilarity between the two alignments is expected when more resistive semiconductors than graphene are used.

It should be noted that for a relatively large-area device, where the ferroelectric layer is composed of many domains, multi-level resistance [61, 62] can also be realized by partial polarization of the ferroelectric layer into its intermediate polarization states [59, 60] using a pulsing scheme. However, downscaling of the devices as eventually needed for neuromorphic applications can limit multi-value resistance. At device dimensions comparable with the ferroelectric domain size, partial polarization of the ferroelectric layer, as to produce multi-levels of resistance, becomes challenging.[63] However, for a patterned ferroelectric

gate, the precise control over the polarization, and therefore channel conductance, is straightforward, whereas for partial polarization, precise control of the polarization level can become challenging.

Realization of differentiable intermediate "01" and "10" states depends very much on the geometrical features, that is, the height and width of the pattern in the ferroelectric layer. To investigate the effect of the geometry on the transfer curve of the Fe-FET, both height and width are varied. In **Figure 4.4a**, the effect of variation in the height for a fixed W_1/W_2 of 0.25/0.75 is shown. The intermediate regime becomes more apparent as the height difference increases, as highlighted for the enlarged section of the transfer curve, where state "10" emerges. Since almost all ferroelectric thin-films are polycrystalline, they have a distributed coercive voltage. As a result, a single switching voltage is absent and there is always a voltage distribution around V_C. For the Fe-FETs with a patterned gate dielectric to have differentiable intermediate states, the height difference should be large enough to ensure that the V_{C1} and V_{C2} are well-separated and do not overlap. Therefore, as a design guide, an optimal height difference of 50% is suggested for clearly discernable "01" and "10" intermediate states in the transfer characteristics of the Fe-FET.

The influence of the width of the patterns on the transfer curve is presented in **Figure 4.4b** for a fixed height difference of 50%, and variable ratio of W_1/W_2. Changes in W have a distributing effect on the polarization, and consequently the current level of the intermediate "01" and "10" states. The minimum W, an important factor for downscaling of the patterned devices, could be as small as tens of nanometers because it was demonstrated that the ferroelectric domain can be stabilized down to tens of nanometer.[65]

The methodology of patterning the ferroelectric gate defines various switching voltages that allow for creating multiple number of resistance states that can be controlled deterministically. As a demonstration, the designs are provided for capacitors with three and four steps in the thickness of the ferroelectric layer, as presented in **Figure 4.6a–c**, respectively. The details of the design, namely the thicknesses and the fractional areal coverage of every thickness, are given in the legends of the **Figure 4.6**. Three steps in the ferroelectric film topography led to six different polarization states, as shown in **Figure 4.5a**. Implementation of the ferroelectric layer as the gate insulator yields a Fe-FET that clearly shows six different resistance states, as shown in **Figure 4.6b**. Similarly, four steps in the ferroelectric film topography leads to eight different polarization states, **Figure 4.5b**, and consequently eight different resistance states in the Fe-FET, as shown in **Figure 4.6d**. It should be noted that the intermediate states are determined by measuring the current at zero gate bias, not at the coercive bias of the intermediate states. Since polarization of the intermediate states is compensated and, therefore, stabilized, the current level of the intermediate states will be, therefore, different and the intermediate states can be easily differentiated from one another.

A brief note should be given about the switching voltages in multi-level resistance states in patterned graphene Fe-FETs. For many applications, including memory and neuromorphic, low-voltage operation of the resistance switching devices is required. The demonstrated patterned graphene Fe-FET operates at rather large voltages, because the primary goal is to demonstrate multi-level resistance switching and to establish the device physics. Nonetheless, the switching voltage of P(VDF-TrFE)-based memory devices could be reliably reduced to sub -3 V[38] upon reducing the thickness to below 20 nm. Therefore, low-voltage operation for the patterned Fe-FET could be realized by preparation of thinner P(VDF-TrFE) gate layers, which necessitated adoption of the P(VDF-TrFE) etching process to low etch rates.
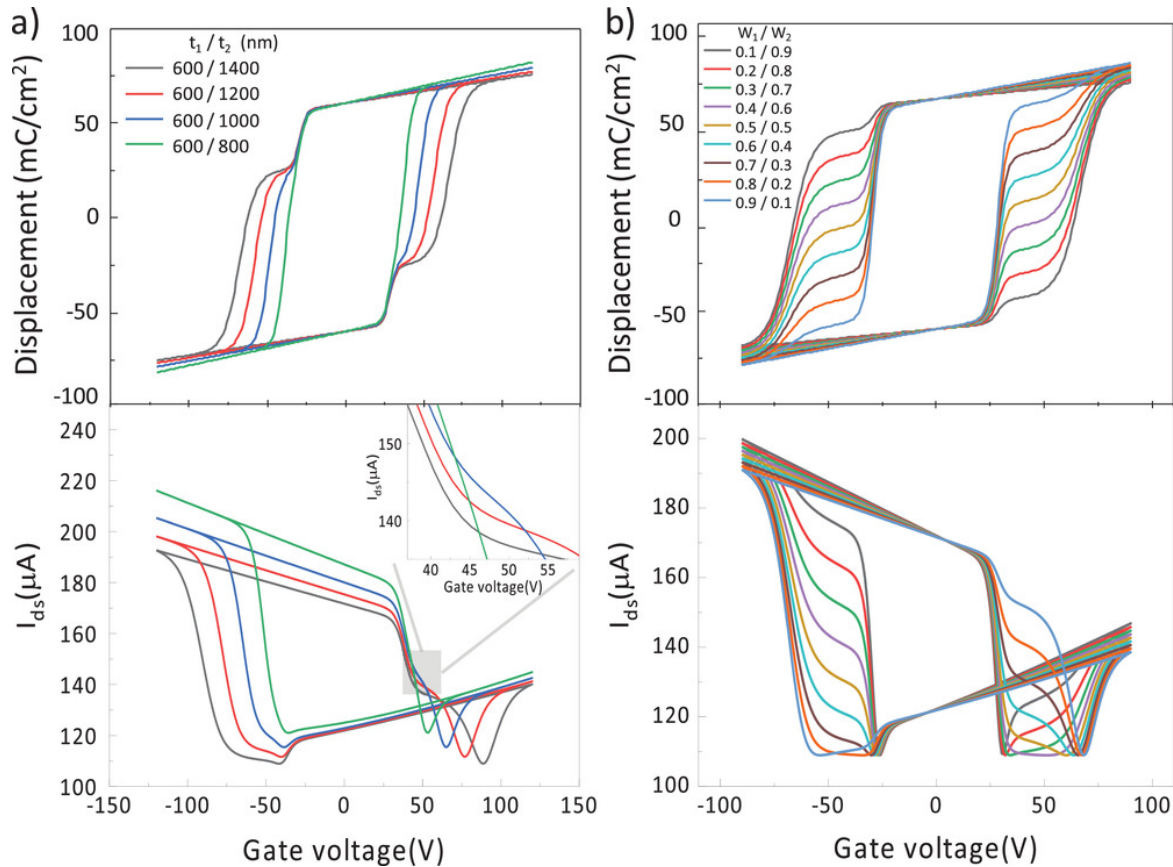
Figure 4.5. The effect of height and width of the patterns in the ferroelectric gate layer on the transfer characteristics of the graphene Fe-FET. a) The influence of different thickness for W_1/W_2 ratio of 0.25/0.75 and b) the effect of the width for t_1/t_2 ratio of 600/1200 nm.

4.3. Conclusion

Using an experimentally validated device model, we have outlined design rules for a quaternary graphene Fe-FET and experimentally demonstrated four stable resistance states of the designed graphene Fe-FET. By introducing a well-defined topographical pattern in the ferroelectric layer, four different switching voltages appear that enable programming of the gate polarization into four different states simply by application of an appropriate gate bias. We have predicted transistors with six and eight different deterministic resistance states. Based on the insight gained from the model, we propose introducing several trenches with various thicknesses within the ferroelectric gate layer to achieve multiple (>2) resistance states in a single transistor with deterministic resistance switching voltages. The device model presented here is generic, and can be adopted for graphene Fe-FETs that are fabricated with inorganic ferroelectrics or dual-gate ferroelectric transistors.[64] Analytical description for the dielectric displacement of the ferroelectric gate layer renders the proposed model applicable to other Fe-FETs based on various 2D materials. When the electrostatic description of the gate is coupled with an appropriate charge transport model, the model can determine the best operational conditions for the Fe-FETs based on the 2D material under study. The next level of complexity would be to enhance the model to include multiferroic and employ the model for the study of multiferroic devices such as multiferroic transistors.
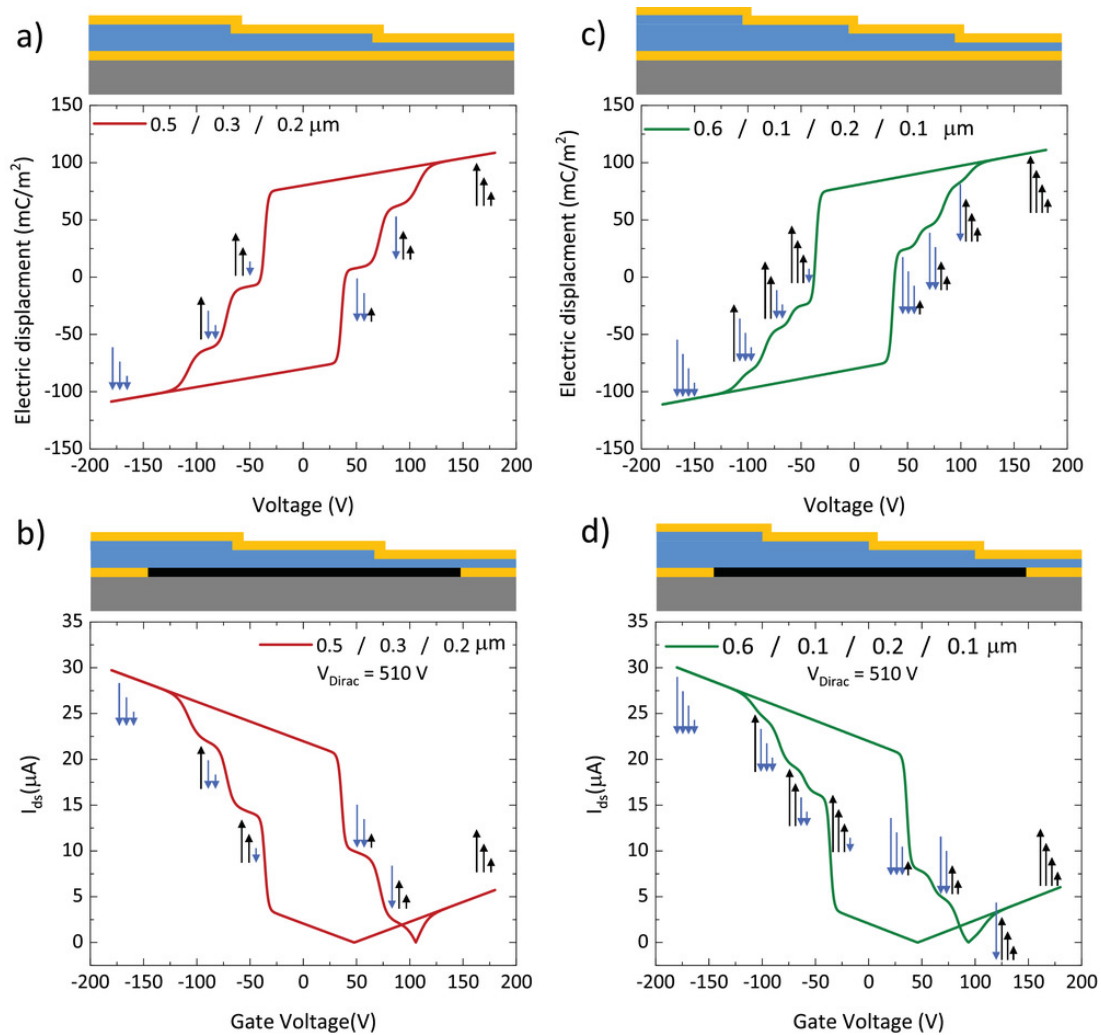
Figure 4.6. a) Schematic of ferroelectric layer with three topographic steps (top) and the simulated corresponding displacement–voltage characteristics in a capacitor (bottom). b) Schematic of ferroelectric transistor with three topographic steps (top) and the simulated corresponding transfer characteristics (bottom), clearly demonstrating six different resistance levels. c) Schematic of ferroelectric layer with four topographic steps (top) and the simulated corresponding displacement–voltage characteristics in a capacitor (bottom). d) Schematic of ferroelectric transistor with four topographic steps (top) and the simulated corresponding transfer characteristics (bottom), clearly demonstrating eight different resistance levels. The first row of the legend in every panel shows the fractional areal coverage for different thicknesses that are given in the second row below it.

Reference

1) Y. J. Doh, G. C. Yi, *Nanotechnology* 2010, **21**, 105204.
2) I. Jung, J. Y. Son, *Carbon* 2012, **50**, 3854.
3) H. S. Lee, S. W. Min, M. K. Park, Y. T. Lee, P. J. Jeon, J. H. Kim, S. Ryu, S. Im, *Small* 2012, **8**, 3111.
4) Y. T. Lee, D. K. Hwang, W. K. Choi, *J. Korean Phys. Soc.* 2016, **69**, 1347.
5) G. D. Belletti, S. D. Dalosto, S. Tinte, *J. Phys.: Condens. Matter* 2016, **28**, 435002.
6) Y. Chen, X. Wang, P. Wang, H. Huang, G. Wu, B. Tian, Z. Hong, Y. Wang, S. Sun, H. Shen, *ACS Appl. Mater. Interfaces* 2016, **8**, 32083.
7) X. Wang, C. Liu, Y. Chen, G. Wu, X. Yan, H. Huang, P. Wang, B. Tian, Z. Hong, Y. Wang, *2D Mater.* 2017, **4**, 025036.
8) C. Yin, X. Wang, Y. Chen, D. Li, T. Lin, S. Sun, H. Shen, P. Du, J. Sun, *Nanoscale* 2018, **10**, 1727.
9) D. Li, X. Wang, Y. Chen, S. Zhu, F. Gong, G. Wu, C. Meng, L. Liu, L. Wang, T. Lin, *Nanotechnology* 2018, **29**, 105202.
10) H. J. Hwang, J. H. Yang, Y. G. Lee, C. Cho, C. G. Kang, S. C. Kang, W. Park, B. H. Lee, *Nanotechnology* 2013, **24**, 175202.
11) H. Zhang, Y. Chen, S. Ding, J. Wang, W. Bao, D. W. Zhang, P. Zhou, *Nanotechnology* 2018, **29**, 244004.
12) F. A. McGuire, Y. C. Lin, K. Price, G. B. Rayner, S. Khandelwal, S. Salahuddin, A. D. Franklin, *Nano Lett.* 2017, **17**, 4801.
13) D. Jin, A. Kumar, K. H. Fung, J. Xu, N. X. Fang, *Appl. Phys. Lett.* 2013, **102**, 201118.
14) X. Wang, P. Wang, J. Wang, W. Hu, X. Zhou, N. Guo, H. Huang, S. Sun, H. Shen, T. Lin, *Adv. Mater.* 2015, **27**, 6575.
15) C. Baeumer, D. Saldana-Greco, J. M. P. Martirez, A. M. Rappe, M. Shim, L. W. Martin, *Nat. Commun.* 2015, **6**, 6136.
16) Y. Zheng, G. X. Ni, C. T. Toh, M. G. Zeng, S. T. Chen, K. Yao, B. Özyilmaz, *Appl. Phys. Lett.* 2009, **94**, 163505.
17) Y. L. Lee, S. Kim, C. Park, J. Ihm, Y. W. Son, *ACS Nano* 2010, **4**, 1345.
18) Y. Zheng, G.-X. Ni, C.-T. Toh, C.-Y. Tan, K. Yao, B. Özyilmaz, *Phys. Rev. Lett.* 2010, **105**, 166602.
19) S. Raghavan, I. Stolichnov, N. Setter, J. S. Heron, M. Tosun, A. Kis, *Appl. Phys. Lett.* 2012, **100**, 023507.
20) S. Lee, Y. Lee, *Carbon* 2018, **126**, 176.
21) M. Dragoman, M. Modreanu, I. M. Povey, A. Dinescu, D. Dragoman, A. Di Donato, E. Pavoni, M. Farina, *Nanotechnology* 2018, **29**, 425204.
22) M. Zhu, J. Wu, Z. Du, R. Y. Tay, H. Li, B. Özyilmaz, E. H. T. Teo, *Nanoscale* 2015, **7**, 14730.
23) Y. Zheng, G.-X. Ni, S. Bae, C.-X. Cong, O. Kahya, C.-T. Toh, H. R. Kim, D. Im, T. Yu, J. H. Ahn, *EPL* 2011, **93**, 17002.
24) W. Lee, O. Kahya, C. T. Toh, B. Özyilmaz, J. H. Ahn, *Nanotechnology* 2013, **24**, 475202.
25) G. X. Ni, Y. Zheng, S. Bae, C. Y. Tan, O. Kahya, J. Wu, B. H. Hong, K. Yao, B. Özyilmaz, *ACS Nano* 2012, **6**, 3935.
26) X. Wang, M. Tang, Y. Chen, G. Wu, H. Huang, X. Zhao, B. Tian, J. Wang, S. Sun, H. Shen, *Opt. Quantum Electron.* 2016, **48**, 345.
27) J. Heidler, S. Yang, X. Feng, K. Müllen, K. Asadi, *Solid-State Electron.* 2018, **144**, 90.
28) A. Rajapitamahuni, J. Hoffman, C. H. Ahn, X. Hong, *Nano Lett.* 2013, **13**, 4374.
29) E. B. Song, B. Lian, S. Min Kim, S. Lee, T. K. Chung, M. Wang, C. Zeng, G. Xu, K. Wong, Y. Zhou, Appl. *Phys. Lett.* 2011, **99**, 042109.
30) H. Wang, Y. Wu, C. Cong, J. Shang, T. Yu, *ACS Nano* 2010, 4, 7221.
31) J. F. Scott, *Science* 2007, **315**, 954.
32) a) P. Zubko, D. J. Jung, J. F. Scott, *J. Appl. Phys.* 2006, **100**, 114112; b) S. Oh, H. Hwang, I. K. Yoo, *APL Mater.* 2019, **7**, 091109.

33) M. H. Yusuf, B. Nielsen, M. Dawber, X. Du, *Nano Lett.* 2014, **14**, 5437.

34) W. Jie, J. Hao, *Nanoscale* 2018, **10**, 328.

35) Y. L. Sun, D. Xie, J. L. Xu, X. M. Li, C. Zhang, R. X. Dai, X. Li, X. J. Meng, H. W. Zhu, *Carbon* 2016, **96**, 695.

36) R. C. G. Naber, K. Asadi, P. W. M. Blom, D. M. De Leeuw, B. De Boer, *Adv. Mater.* 2010, **22**, 933.

37) K. Asadi, E. C. Timmering, T. C. T. Geuns, A. Pesquera, A. Centeno, A. Zurutuza, J. H. Klootwijk, P. W. M. Blom, D. M. De Leeuw, *ACS Appl. Mater. Interfaces* 2015, **7**, 9429.

38) a) M. Li, I. Katsouras, K. Asadi, P. W. M. Blom, D. M. De Leeuw, *Appl. Phys. Lett.* 2013, **103**, 072903; b) R. C. G. Naber, P. W. M. Blom, A. W. Marsman, D. M. de Leeuw, *Appl. Phys. Lett*. 2004, **85**, 2032; c) R. C. G. Naber, B. de Boer, P. W. M. Blom, D. M. de Leeuw, *Appl. Phys. Lett.* 2005, **87**, 203509; d) M. Li, N. Stingelin, J. J. Michels, M.-J. Spijkman, K. Asadi, R. Beerends, F. Biscarini, P. W. M. Blom, D. M. de Leeuw, *Adv. Funct. Mater.* 2012, **22**, 2750; e) M. Kumar, D. G. Georgiadou, A. Seitkhan, K. Loganathan, E. Yengel, H. Faber, D. Naphade, A. Basu, T. D. Anthopoulos, K. Asadi, *Adv. Electron. Mater.* 2020, **6**, 1901091.

39) R. C. G. Naber, J. Massolt, M. Spijkman, K. Asadi, P. W. M. Blom, D. M. De Leeuw, *Appl. Phys. Lett.* 2007, **90**, 113509.

40) S. L. Miller, J. R. Schwank, R. D. Nasby, M. S. Rodgers, *J. Appl. Phys.* 1991, **70**, 2849.

41) J. J. Brondijk, K. Asadi, P. W. M. Blom, D. M. de Leeuw, *J. Polym. Sci., Part B: Polym. Phys.* 2012, **50**, 47.

42) K. Asadi, P. W. M. Blom, D. M. De Leeuw, *Appl. Phys. Lett.* 2011, **99**, 053306.

43) S. Kim, J. Nah, I. Jo, D. Shahjerdi, L. Colombo, Z. Yao, E. Tutuc, S. K. Banerjee, *Appl. Phys. Lett.* 2009, **94**, 062107.

44) F. Xia, V. Perebeinos, Y. M. Lin, Y. Wu, P. Avouris, *Nat. Nanotechnol.* 2011, **6**, 179.

45) G. W. Burr, *Nat. Mach. Intell.* 2019, **1**, 10.

46) S. H. Jo, T. Chang, I. Ebong, B. B. Bhadviya, P. Mazumder, W. Lu, *Nano Lett.* 2010, **10**, 1297.

47) Z. Wang, H. Wu, G. W. Burr, *Nat. Rev. Mater.* 2020, **5**, 173.

48) M. Prezioso, F. Merrikh-Bayat, B. Hoskins, G. C. Adam, K. K. Likharev, D. B. Strukov, *Nature* 2015, **521**, 61.

49) H. Tsai, S. Ambrogio, P. Narayanan, R. M. Shelby, G. W. Burr, *J. Phys. D: Appl. Phys.* 2018, **51**, 3001.

50) S. Ambrogio, P. Narayanan, H. Tsai, R. M. Shelby, Boybat, C. di Nolfo, S. Sidler, M. Giordano, M. Bodini, N. C. P. Farinha, B. Killeen, C. Cheng, Y. Jaoudi, G. W. Burr, *Nature* 2018, **558**, 60.

51) M. Courbariaux, Y. Bengio, J. P. David, *in Advances in Neural Information Processing Systems* 28 (Eds: C. Cortes, N. D. Lawrence, D. D. Lee, M. Sugiyama, R. Garnett), Curran Associates, Inc., New York 2015, p. 3123.

52) W. Tang, G. Hua, L. Wang, presented at *Proc. of the Thirty-First AAAI Conf. on Artificial Intelligence, San Francisco*, CA February 2017.

53) B. Tian, L. Liu, M. Yan, J. Wang, Q. Zhao, N. Zhong, P. Xiang, L. Sun, H. Peng, H. Shen, T. Lin, B. Dkhil, X. Meng, J. Chu, X. Tang, C. Duan, *Adv. Electron. Mater.* 2019, **5**, 1800600.

54) Y. Chen, Y. Zhou, F. Zhuge, B. Tian, M. Yan, Y. Li, Y. He, X. S. Miao, *npj 2D Mater. Appl.* 2019, **3**, 31.

55) E. J. Kim, K. A. Kim, S. M. Yoon, *J. Phys. D: Appl. Phys.* 2016, **49**, 075105.

56) S. M. Yoon, S. Yang, C. W. Byun, S. W. Jung, M. K. Ryu, S. H. K. Park, B. Kim, H. Oh, C. S. Hwang, B. G. Yu, *Semicond. Sci. Technol.* 2011, **26**, 034007.

57) M. Hassanpour Amiri, J. Heidler, K. Müllen, K. Asadi, *ACS Appl. Electron. Mater.* 2020, **2**, 2.

58) M. Hassanpour Amiri, J. Heidler, A. Hasnain, S. Anwar, H. Lu, K. Müllen, K. Asadi, *RSC Adv.* 2020, **10**, 1127.

59) T. C. Macleod, T. A. Philips, F. D. Ho, *Integr. Ferroelectr.* 2007, **89**, 12.

60) A. K. Tripathi, A. J. J. M. van Breemen, J. Shen, Q. Gao, M. G. Ivan, K. Reimann, E. R. Meinders, G. H. Gelinck, *Adv. Mater.* 2011, **23**, 4146.

61) J. Lee, A. J. J. M. van Breemen, V. Khikhlovskyi, M. Kemerink, R. A. J. Janssen, G. H. Gelinck, *Sci. Rep.* 2016, **6**, 24407.

62) D. Zhao, I. Katsouras, K. Asadi, W. A. Groen, P. W. M. Blom, D. M. de Leeuw, *Appl. Phys. Lett.* 2016, **108**, 232907.

63) H. Mulaosmanovic, T. Mikolajick, S. Slesazeck, *ACS Appl. Mater. Interfaces* 2018, **10**, 23997.

64) I. Katsouras, D. Zhao, M.-J. Spijkman, M. Li, P. W. M. Blom, D. M. de Leeuw, K. Asadi, *Sci. Rep.* 2015, **5**, 12094.

65) R. Xu, S. Liu, S. Saremi, R. Gao, J. J. Wang, Z. Hong, H. Lu, A. Ghosh, S. Pandya, E. Bonturim, Z. H. Chen, L. Q. Chen, A. M. Rappe, L. W. Martin, *Nat. Commun.* 2019, **10**, 1282.

Chapter 5

Design of a multiferroic/piezoelectric Energy-harvesting measurement setup

Abstract

Multiferroic energy harvesting devices have been proposed as a promising sustainable energy source for delivering electricity to low-power electronics, where delivering electricity using conventional means is not feasible nor desirable. To gauge the potential of the multiferroics, the performance of the harvesting devices should be evaluated reliably. In this chapter, some of the basic concepts are introduced, and software is developed and experimentally validated that can be reliably employed for the evaluation of the energy piezoelectric and multiferroic energy harvesting devices. At the end of the chapter, a protocol is suggested that standardise data collection and analysis for the piezoelectric and multiferroic energy harvesting devices.

5.1. Introduction

Piezoelectric and multiferroic materials have been recently the topic of extensive research activities for application in energy harvesting devices. [1-12] They are considered as promising candidates for implementing battery-less and miniaturized electronic systems for internet of the things (IoT) modules [13-17], body-mounted and wearable health monitoring gadgets, and body-implanted microsystems. [18-26,29]

A wide range of inorganic and organic piezo/multiferroic materials with various geometry, structure, composition, etc., have been suggested in pursuit of a plausible candidate for energy harvesting applications. The suggested candidates have advantages and disadvantages depending on the specifics of the application domain. Ceramic-based materials like Lead zirconate titanate (PZT) produce relatively large voltage outputs at the cost of being brittle.[27] The polymer-based materials, like polyvinylidene fluoride (PVDF) and its copolymer with trifluoroethylene (P(VDF-TrFE)), show good merits for integrating conformable and body implantable systems due to their inherent flexibility and bio-compatibility.

Having a reliable and accurate measuring framework is a prerequisite to compare the performance of the energy harvesting materials and devices. The ambiguity arises when comparing literature data. It is found that many of the reported piezoelectric energy harvesting devices show their best performance at nearly identical internal impedance values of 1 MΩ despite being fabricated from different materials. The identicality between various reports stems from the fact that all reports have used commercially available voltmeters and oscilloscopes for the electrical characterization of the piezo/triboelectric materials. [28]

Almost all piezoelectric materials and polymer-based multiferroics are insulators. Under an external excitation, being an external mechanical force or a variable magnetic field, these materials show displacement of charges, which can be measured (or collected and stored) when the comprising device is connected to an external circuit. The piezoelectric/multiferroic material should have a poor conductance so that the accumulated charges remain intact and are not lost. The resulting electrical potential between the poles (electrodes) of the piezoelectric/multiferroic device can be measured with various instruments ranging from voltmeter and oscilloscope to electrometer. However, the actual value of the voltage developed between the two electrodes measured using different instruments is not necessarily the same due to the variation in the input impedance of the measuring instruments. [28] Because of the insulating nature of piezoelectrics and multiferroics, particularly the polymer-based systems, the impedance of their comprising devices is typically high and can be up to a few orders of magnitude larger than the input impedance of the measurement instruments, which demands for extra attention.

This chapter presents a setup that is designed to perform reliable measurements on piezoelectric and multiferroic energy harvesters, and to confidently compare the harvested power. The design starts with an equivalent electric model of a typical piezoelectric element and continues by expressing the conditions imposed by the theory of maximum power transfer from circuit theorem to optimize the harvested power. In addition, various configurations are presented to evaluate different scenarios to maximize the harvested power. A setup is home-built that allows for measuring the voltage and power output of the piezoelectric generators. Moreover, the detailed design and realization of an electronic measuring system are discussed. Note that in what follows, the focus is on piezoelectric harvesters. Nevertheless, the same setup can be adopted for a multiferroic harvester.

5.2. Electric model of piezoelectric energy harvester

From a system point of view, a piezoelectric energy harvester can be considered as a transducer, transforming mechanical energy into electricity. [30,32] **Figure 5.1** shows a simple drawing of this transformation. The mechanical part consists of σ_{in}, m, and r, which represent the energy source, mechanical potential energy storage element, and mechanical energy loss, respectively. The internal electric impedance of the piezoelectric generator is modelled by the parallel combination of R_L and C_P where the output voltage appears across them. The transducing ratio between the mechanical and electric parts is given by α:1 and is illustrated by two mutually coupled transformers.
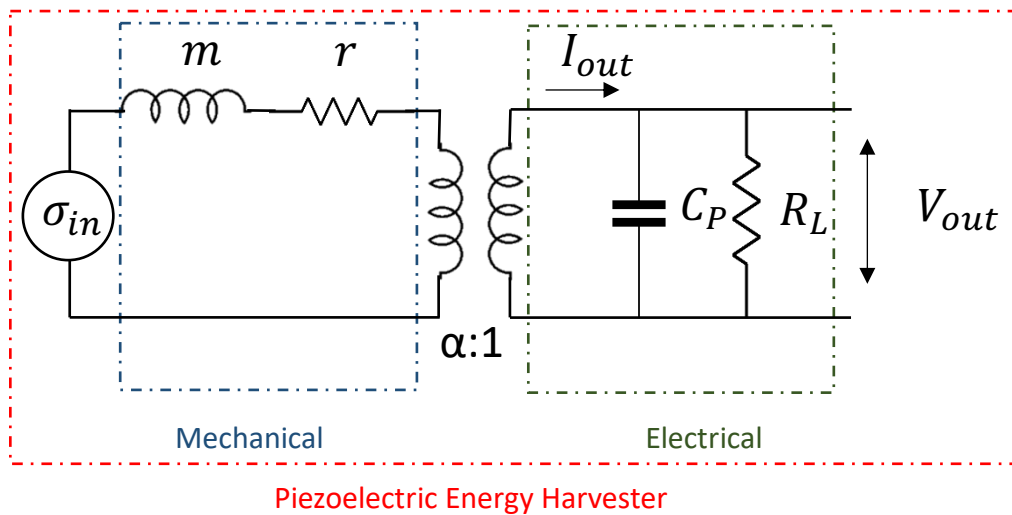
Figure 5.1. *systemic electric model of a piezoelectric energy harvester, two mutually coupled inductors represent the coupled nature of mechanical and electrical properties of piezoelectric materials.*
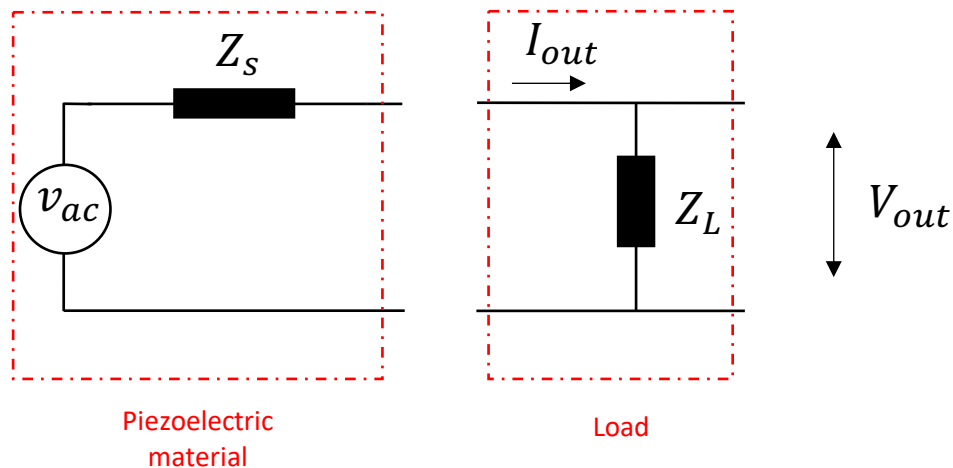
Figure 5.2. *A piezoelectric energy source with a connected electrical consumer modeled as a load.*

Figure 5.1 depicts the piezoelectric energy harvester in an unloaded scenario. In reality, there is always an electronic consumer connected to the energy source, as shown in **Figure 5.2**. Z_s and Z_L are the equivalent internal impedance of the source and input impedance of the load, respectively. The ratio of these two variables is relevant for maximizing the transferred power from the source to the consumer. This is the subject of the maximum power transfer theorem in electrical engineering.[33]

5.3. Maximum power transfer theorem

It is common to evaluate the merit of a piezoelectric energy source by measuring the open-circuit voltage V_{oc} and short-circuit current I_{SC} between its terminals. According to the definition, while measuring the V_{oc}, no current should pass through the circuit. This implies that the input impedance of the measuring instrument, voltmeter or oscilloscope, should be ideally infinite to block current flow, as it would result in a voltage drop across the terminals of the measuring instrument. **Figure 5.3** shows the equivalent circuit of the piezoelectric source, which consists of an ideal voltage source in series with an equivalent impedance Z_{piezo}. On the right, a typical input stage of a measuring instrument is pictured. It includes some sub-circuits like signal conditioning stage, sample and holds stage, and transimpedance amplifier, to name a few. The input impedance is designated as Z_{input}.
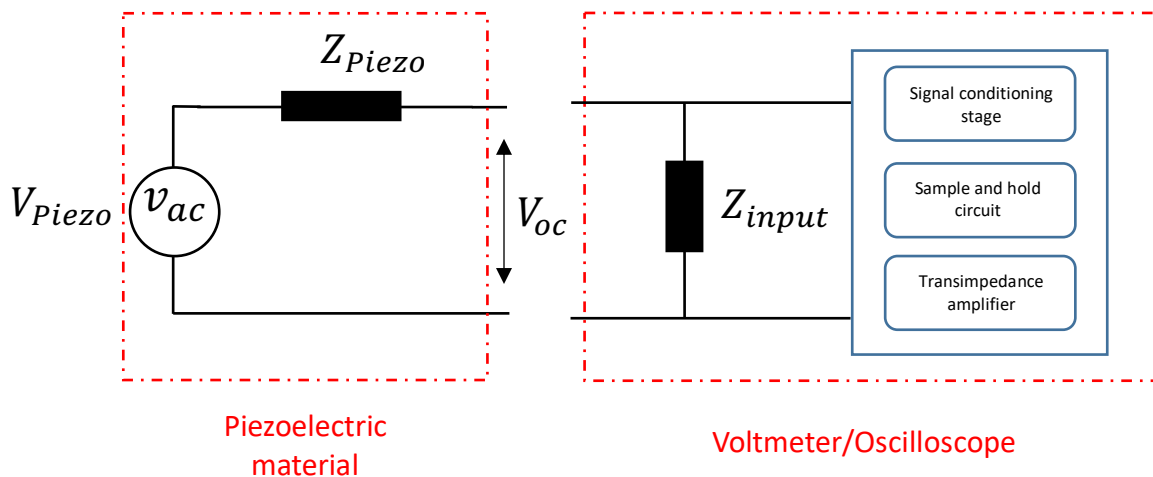
Figure 5.3. Interfacing the piezoelectric energy harvester with a voltmeter or oscilloscope, with some of internal blocks and sub circuits.

The measurement instrument, voltmeter or oscilloscope measures:

$$V_{oc} = V_{Piezo} \times \frac{Z_{input}}{Z_{Piezo} + Z_{input}} \tag{5.1}$$

Therefore, the condition for an accurate measurement is:

$$Z_{input} \gg Z_{Piezo} , V_{OS} \approx V_{Piezo} \tag{5.2}$$

The above condition is almost always fulfilled during the voltage measurement of typical voltage sources since the Thevenin impedance of the voltage sources is usually very small and negligible. However, this assumption is no longer valid during the measurement of the open-circuit voltage of a piezoelectric source since its impedance is considerably high and comparable with the input impedance of the measuring instrument. Therefore, care must be taken during the measurement of V_{oc}.

Similarly, when the piezoelectric source is connected to an energy consumer, as illustrated in **Figure 5.4**, it is always desired to transfer the maximum possible amount of power to the consumer. This requires the following:

$$V_{out} = V_{Piezo} \times \frac{Z_L||Z_{input}}{Z_s + (Z_L||Z_{input})}$$

$$I_L = I_{out} \times \frac{Z_{input}}{Z_L + Z_{input}} \tag{5.3}$$

$$I_{out} = \frac{V_{Piezo}}{Z_s + (Z_L||Z_{input})}$$
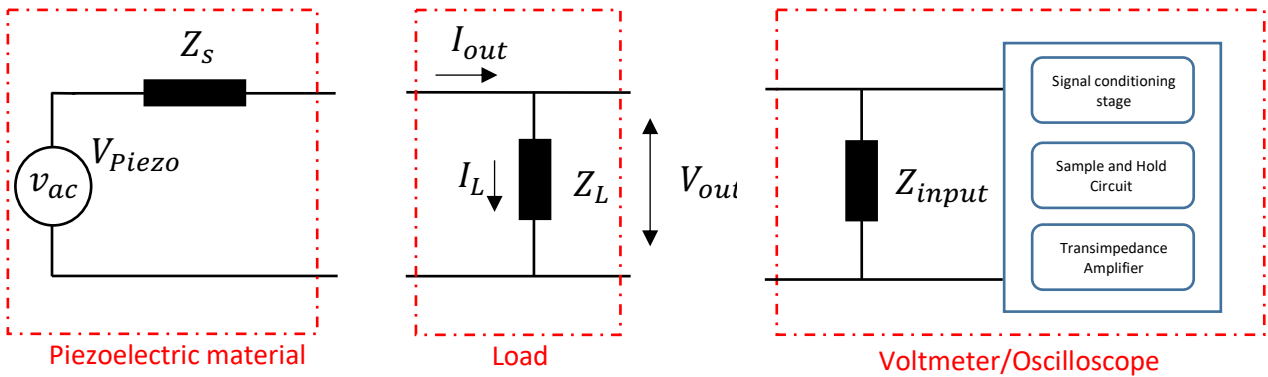
Figure 5.4. Piezoelectric energy source, connected to a load and a voltmeter or an oscilloscope.

Therefore, the power that the harvester can deliver is a function of the internal impedances as follows:

$$P_L = I_L \times V_{out} = \frac{V_{Piezo}}{Z_s + (Z_L||Z_{input})} \times \frac{Z_{input}}{Z_L + Z_{input}} \times V_{Piezo} \times \frac{Z_L||Z_{input}}{Z_s + (Z_L||Z_{input})} \tag{5.4}$$

Taking the derivative of P_L with respect to Z_L, gives the following conditions which guarantee the maximum power delivery to the load:

$$Re\{Z_s\} = Re\{Z_L||Z_{input}\}$$

$$Im\{Z_s\} = -Im\{Z_L||Z_{input}\} \tag{5.5}$$

$$Z_L \ll Z_{input}$$

In other words, impedance matching theory implies that the load's impedance should be the complex conjugate of the internal impedance of the piezoelectric source. It means that, regarding the capacitive behavior of the piezoelectric source, the resistance of the load should be equal to the resistance of the source, while the imaginary part of the load needs to be inductive to cancel out the capacitance of the piezoelectric element.

5.4. Voltage rectification

Figure 5.5 shows the voltage output of a piezoelectric polymer subject to a periodic mechanical strain. It can be seen that the polarity of the voltage continuously alters in time. This is due to the switching of the charges developed across the sandwiching electrodes of the piezoelectric material during the compression and expansion.
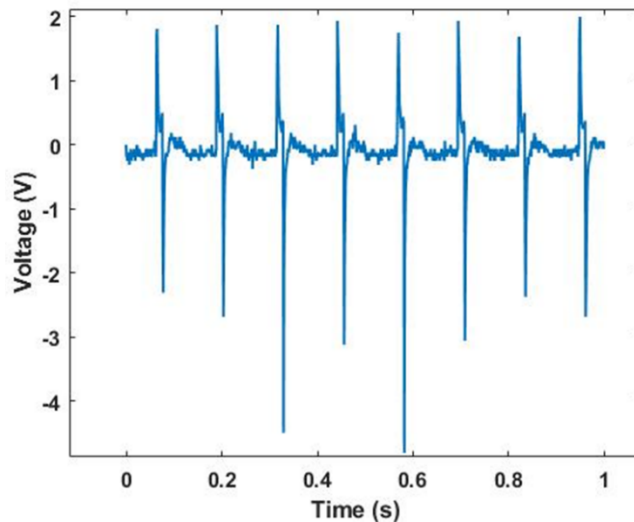
Figure 5.5. *Voltage response of a piezoelectric polymer subject to periodic mechanical force in a truncated time window.*

Typical electronic circuits require a direct current (DC) voltage source to operate. Therefore, piezoelectric energy harvesters need to be accompanied by a voltage rectifier circuit to supply the consumers during both positive and negative half-cycles. Voltage rectifiers are usually implemented utilizing rectifying diodes. **Figure 5.6a** shows a full-wave voltage rectifier using a p-n junction diode bridge. When the polarity of the voltage is positive, diodes 1 and 2 conduct, while diodes 3 and 4 are off, similarly, diodes 3 and 4 are on and diodes 1 and 2 are off, in the negative cycle. This configuration guarantee that V_{out} is always equal or larger than zero volt.
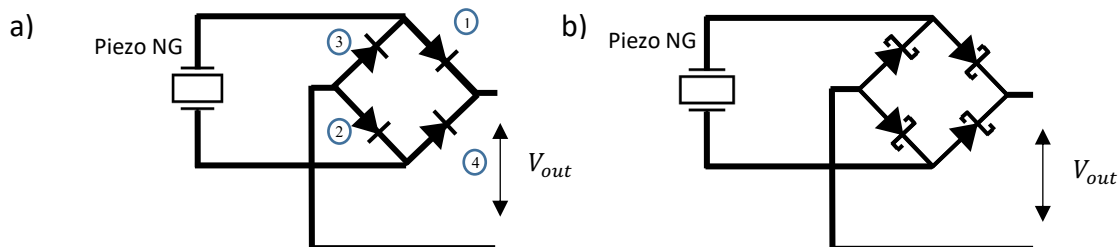
Figure 5.6. *Full wave voltage rectifier diode bridge using a) conventional Si diodes and b) Schottky diodes.*

For any forward-biased p-n junction diode, a voltage drop of 0.6 to 0.7 V is inevitable, resulting in a 1.4 volts dead zone in the voltage output of the diode bridge. Although it may be negligible for electronic consumers connected to the grid, it is a massive energy loss for an electronic consumer intended to be fed by a piezoelectric or multiferroic energy harvester. An immediate solution to mitigate the problem is replacing the Si diodes with Schottky diodes with a lower threshold voltage at around 0.3 to 0.4 volt. This is also beneficial for piezoelectric energy harvesters, actuated with high-frequency acoustic waves, since

metal-semiconductor junctions in a Schottky diode exhibit a lower junction capacitance than conventional Si diodes, making them more responsive in the high-frequency regime. However, the higher leakage current of the Schottky diodes is a major drawback and has a negative impact on the overall energy efficiency of the harvesting system.

Besides the solutions based on passive components like diodes, it is also possible to realize a voltage rectifier based on actively controlled switching elements like MOSFETs. These so-called active or synchronous voltage rectifiers guarantee a rectified wave-shape on output voltage terminals by actively turning the MOSFETs in the circuit, on and off. An integrated comparator detects the polarity of the voltage and accordingly turns on and off the corresponding MOSFET switches. The advantage of this method is that due to the low resistance of MOSFETs in their on state, $R_{DS(on)}$, which can be as low as 10 mΩ, the rectifier's voltage drop and energy loss are significantly reduced. Since there are always two transistors in either positive and negative cycles in the on state, the total resistance in the path is always 2x$R_{DS(on)}$. **Figure 5.7a** shows the LT4320 from *Linear Technology* as an example of a commercial active voltage rectifier using MOSFETs.[34]

The Thermograph of **Figure 5.7b** manifests the energy-efficiency superiority of active rectification over a passive one. Therefore, an active rectifier can be a good candidate for applications emphasizing energy efficiency of piezoelectric or multiferroic energy harvesters. [35-37] **Figure 5.8a** presents a comparison between the three suggested rectification methods above, wherein the voltage output of a piezoelectric energy harvester based on nylon-11 is presented when the material is under exactly similar mechanical stress. The voltage signal appears upon the application and release of the mechanical stress. **Figure 5.8b** depicts the rectified voltage in an ideal scenario when there are no losses due to the rectification circuits. However, there are losses as explained above, shown in **Figure 5.8c**, where the outputs of various passive and active rectifying options are compared. As expected, active rectification has a lower voltage drop and is a more power-efficient solution.
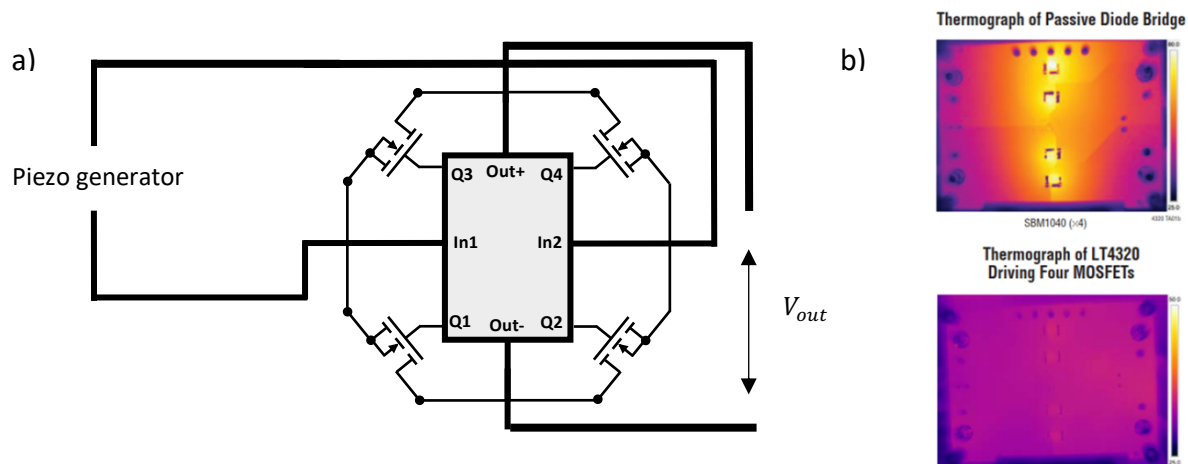
Figure 5.7. a) Circuit diagram of a commercial active rectifier IC based on four MOSFETs b) Comparison between thermographs of the active and passive rectifier bridges. Data presented in b) were obtained from LT4320 data sheets from Linear Technology IC manufacturer.

a)

b)

c)
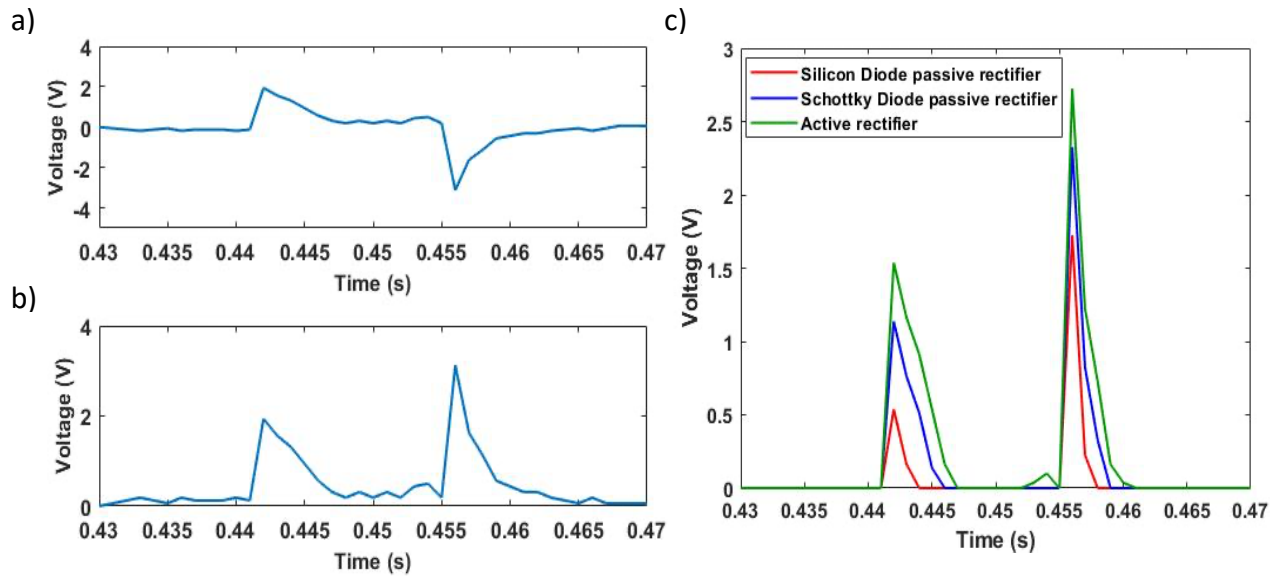
Figure 5.8. *a) A typical voltage trace produced by a piezoelectric material (in this case nylon-11). b) Ideal rectified voltage without any loss and voltage attenuation. c) Comparison between the voltage output of active and passive voltage rectifiers.*

5.5. An energy harvesting (piezoelectric) test system

Following the discussion on the measurement principles and basic circuit consideration, we are now in a position to design a measurement system. Here, a detailed design of a home-built computerized measurement system is presented that enables the evaluation of piezoelectric and multiferroic materials for energy harvesting. It should be noted that for the evaluation of the proposed setup we used mechanical excitation produced by impact from a hammer head attached to a sewing machine. Nevertheless, the electronics can be used for a multiferroic harvester. **Figure 5.9** shows the schematic of the system consisting of the modified sewing machine, a designed analogue front-end (AFE) circuit, a commercial Arduino Due circuit board, and a custom controlling software hosted by a computer.
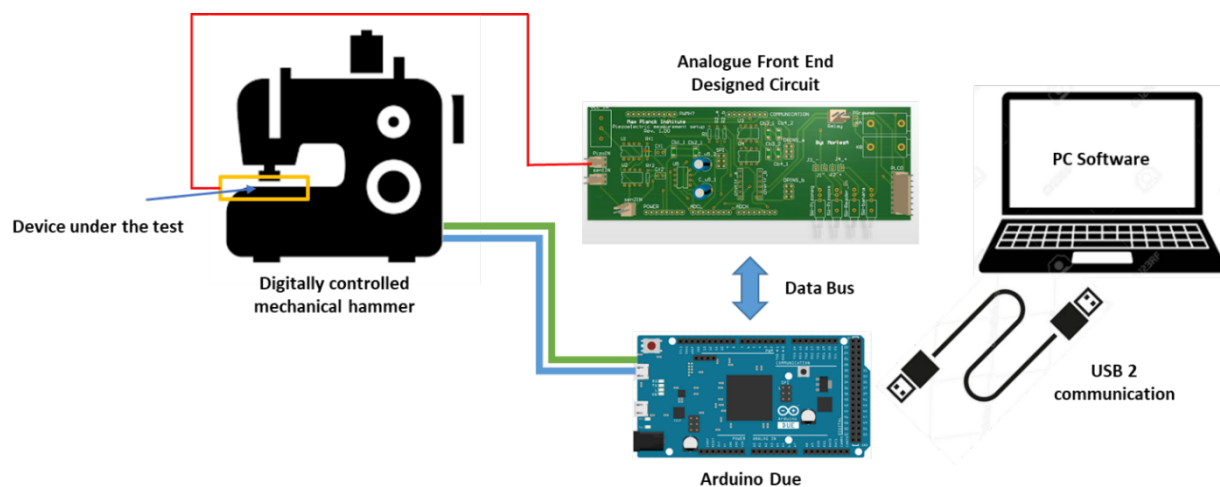
Figure 5.9. *Schematic of the designed system for piezoelectric (or multiferroic) energy harvester evaluation.*

5.5.1. Arduino Due circuit board

We used a commercially available Arduino Due circuit board as the digital heart of the system. The clock of the board is 86 MHz and is fast enough to capture the transient response of the device under test (DUT). It has several general-purpose input/output (GPIO) pins to control the peripherals of the system. One of these GPIO pins is used to feed an electromechanical relay to turn on and off the digital hammer. Three multiplexed channels of the board's analogue to digital converters (ADC) are utilized to digitalize the device response and two pressure sensors implemented in the system. Finally, the board communicates with the host PC and its software to receive the commands and send the measurement data for analysis and presentation.

5.5.2. Digitally controlled mechanical hammer

A hammerhead is designed and fabricated by 3D printing and replaced with the moving needle section of the sewing machine. We used this rigid head to apply the mechanical impact on the DUT. The Arduino Due board can electronically turn on/off the board via a relay upon receiving a command from the PC. Frequency of the impacts can be controlled by a potentiometer and can be varied in a 1 to 10 Hz interval.

5.5.3. Analogue front-end circuit

An analog front-end circuit hosts the signal-conditioning sub-circuits for the DUT's response signal and the accompanying calibration pressure sensors. **Figure 5.10** depicts the schematic of the circuit with its blocks. Block A consists of the pressure sensor readout circuit, section B illustrates the shift and scale circuit, and section C is the sub-circuit to generate negative voltage used for biasing the pressure sensors.
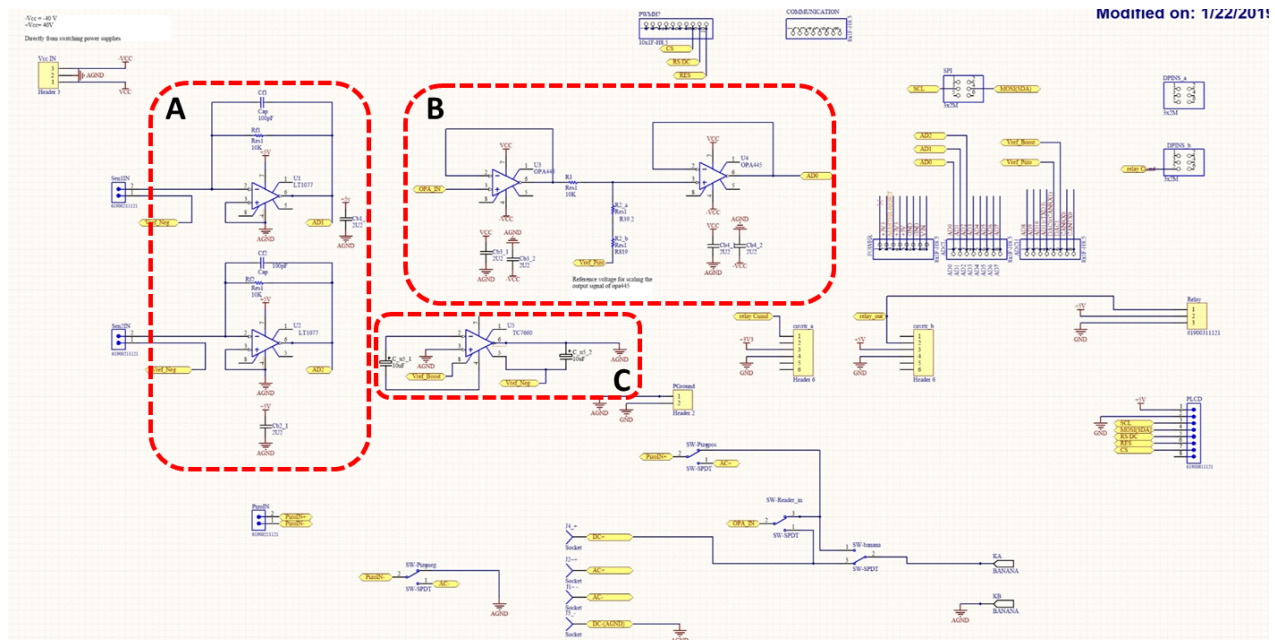
Figure 5.10. Schematic of the AFE circuits and its sub blocks, section "A" shows the pressure sensor inputs and the corresponding amplifiers, section "B" designates the shift and scale stage for interfacing the board with the piezoelectric energy harvesting element and section "C" indicates the charge pump DC-DC converter.

5.5.3.1. Calibrating pressure sensor readout

Designated black A in **Figure 5.10** is the biasing circuit for two commercial pressure sensors, which sandwich the DUT. We used the read values from the sensors to calibrate the exerted pressure on the piezoelectric DUT. **Figure 5.11** shows the circuit and the selected values in the design. The component values are determined based on the required range of responsivity of the pressure sensors. The circuit is calibrated with some known weights to build a look-up table and piecewise-defined function, reflecting the relationship between the applied pressure and the sensor's voltage output. Two ADC channels read the output of the sensors.
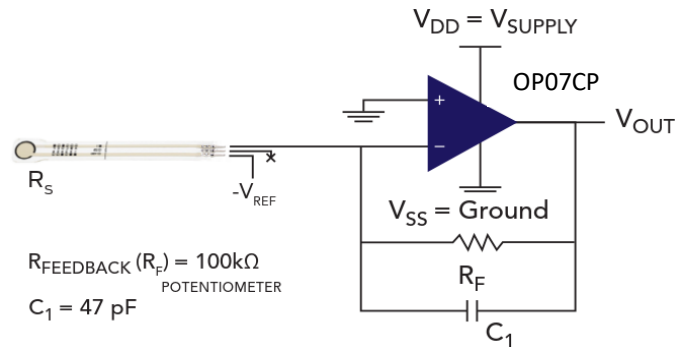
Figure 5.11. *Schematic of the biasing circuit of the pressure sensors and accompanying components.*

5.5.3.2 Shift and scale circuit

The shift and scale stage consist of two back-to-back connected operational amplifiers (Opamp), U3 and U4, as pictured in **Figure 5.12**. The non-inverting input of the U3 Opamp is fed by the voltage output of the piezoelectric DUT.
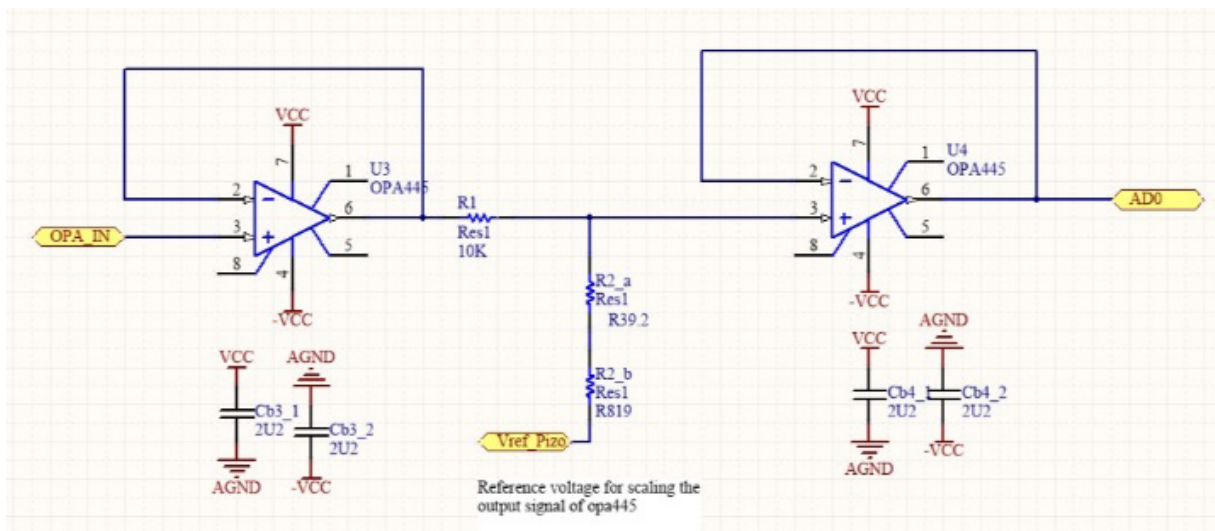
Figure 5.12. *The shift and scale block diagram consisting of two OPA445 Opamps from Linear Technology© with the resistors.*

OPA445 Opamp is chosen for this circuit since its input impedance is extremely high, due to the JFET differential pair in the input stage of the Opamp. Based on the data from the datasheet from the manufacturer, in both differential and standard modes, the input impedance of OPA445 is larger than tens of TΩ ($10^{14} \sim 10^{13}$ Ω) which should alleviate the loading effect that was discussed in section 5.3. Moreover, OPA445 benefits from a wide voltage range of ±45 V, giving a full voltage swing of almost 85 V. The voltage swing is therefore large enough for a wide range of piezoelectric (as well as multiferroic) elements with high voltage transient candidate for following the high-frequency input signals. In addition, the slew rate of the OPA445 is 15V/μs, which is fast enough for the targeted application.

We used the AD0 channel of Arduino Due's internal ADC to convert the analogue response of the DUT into a digital signal. Since this ADC has 12 bits resolution and can convert analogue voltages between 0 to 3.3 V, the DUT voltage output should be shifted and scaled to fit this interval. To fulfil this requirement, U3 is used as a voltage buffer with unity gain, which delivers the DUT's voltage to the resistive network, consisting of R1, R2_a, and R2_b. These resistors, accompanied with U4, attenuate and shift the input voltage response in the interval of ±40V to map it into the acceptable range of 0 ~ 3.3V. A reference voltage is also required at the pin, designated with V_{Ref_Piezo} in **Figure 5.12**. This pin is connected to the digital to analogue (DAC) output of the Arduino Due board. Values of the resistors and V_{Ref_Piezo} were chosen accordingly to meet the requirement imposed by those above-mentioned constrains of ADC.

5.5.3.3. Charge pump DC-DC voltage converter

The pressure sensor biasing and readout circuit requires a negative reference voltage to operate. Since the board is supplied only with a positive voltage source, a charge pump DC to DC voltage converter converts the +5V voltage to -5V. TC7660 from Microchip© is used for this purpose in the designated black C, as shown in **Figure 5.10**. Two 10μF electrolyte capacitors are added to make the unit working properly.

5.6. Load resistors

As described in section 5.3, one of the widespread investigations of energy harvesters is the amount of delivered power at different loads. **Figure 5.12** shows a typical graph showing the harvested power for various resistive loading. We discussed that the deteriorative effect of the low impedance oscilloscope might lead to inaccurate measurement. To address this need, two banana-cable inputs are placed on the PCB, and the user can connect an externally adjustable potentiometer to calculate the harvested power while sweeping the resistance of the load. Alternatively, an array of digital potentiometers can be employed to sweep several decades of resistance. This is readily applicable thanks to predicted controlling pins on the PCB.
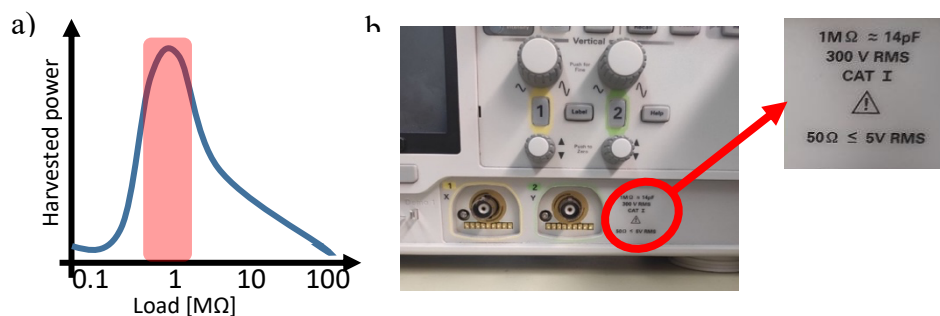
Figure 5.13. *a) Schematic plot of harvested power vs. resistive load b) A typical oscilloscope and its input impedance written on the body of the instrument.*

5.7. The final board and the PC software

Figure 5.15 shows the final design board with some auxiliary peripheral components like a small LCD to show the system's status.
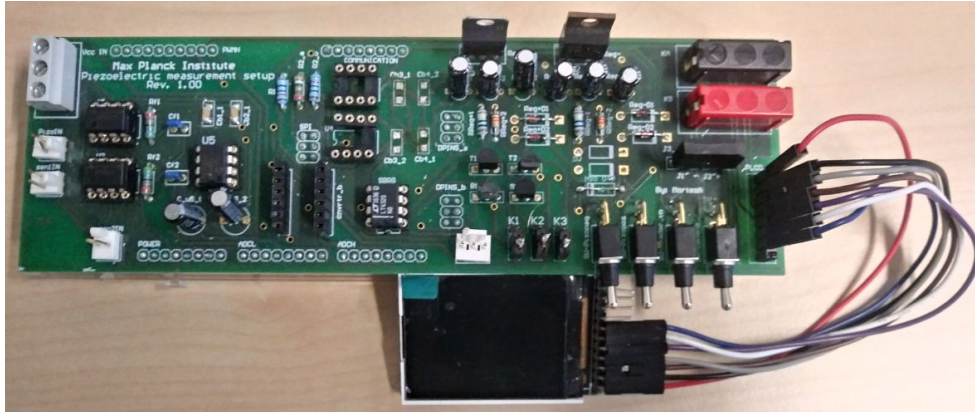
Figure 5.14. Assembled PCB with connected LCD.

A graphical user interface (GUI) is designed for data communication, sending the user-defined commands to the circuit board, and plotting the measurement results. **Figure 5.7a** shows the GUI designed by the C# programming language. Two digital gauges show the applied pressure profile to the piezoelectric film. The user defines the load resistance in a text box in the GUI and, according to the equation below, the software calculates and plot the output voltage and harvested power in real-time:

$$P(t) = \frac{V(t)_{out}^2}{R_L} \tag{5-6}$$

Figure 5.14b show the real-time harvested power and accumulated harvested energy for a load resistance of R_L=100 KΩ. Harvested energy is the time integration of the Instantaneous harvested power.
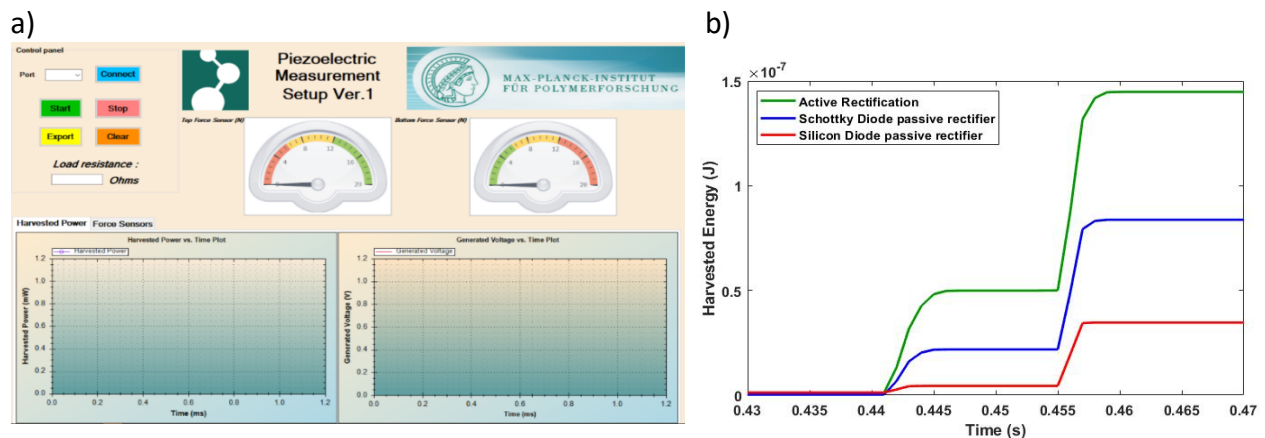
Figure 5.15. a) Graphical user interface of the software developed for data acquisition. b) accumulative harvested energy for three rectification methods for R_L=100 KΩ.

This can be confirmed by comparing the **Figure 5.14b**, which demonstrate the superiority of active rectification in comparison to the other two passive methods by harvesting higher amount of energy in a truncated time frame.

5.8. Conclusion

This chapter covered some of the critical issues for interfacing the piezoelectric and multiferroic energy harvesters with electronic circuits, and measurement instruments. By introducing the equivalent electric circuit of the piezoelectric energy harvester, criteria for maximum power transfer are discussed. Next, the details of designing and realizing an electromechanical measurement system to evaluate the piezoelectric and multiferroic materials is presented. All the subsystems and necessary components are introduced, and their working mechanism is explained in detail. Finally, three different rectification circuits are discussed and compared for maximizing the harvested energy.

Reference

1) S. R. Ganapathy, H. Salleh, M. K. A. Azhar, *Sci. Rep.* 2021, **11**, 4458.

2) S. Yu, Y. Zhang, Z. Yu, J. Zheng, Y. Wang, H. Zhou, *Nano Energy* 2021, **80**,105519.

3) X. Liu, Y. Liu, T. Cheng, Y. Gao, Z. Yang, *Nano Energy* 2022, **92**, 106699.

4) Y. Guo, X. Zhang, Y. Zang, W. Gong, Q. Zhang, H. Wang, J. Brugger, *Nano Energy* 2018, **48**, 152-160.

5) M. Zhu, Qi. Shi, T. He, Z. Yi, Y. Ma, B. Yang, T. Chen, C. Lee, *ACS Nano* 2019**, 13** (2), 1940-1952.

6) Q. Zheng, B. Shi, Z. Li, Z. L. Wang, *Adv. Sci.* 2017, **4**, 1700029.

7) H. Askari, A. Khajepour, M. B. Khamesee, Z. Saadatnia, Z. L. Wang, *Nano Today* 2018, **22**, 10-13.

8) L. Zhao, Hu Li, J. Meng, Y. Zhang, H. Feng, Y. Wu, Z. Li, *Sci. Bull.* 2021, **66**, 14, 1409-1418.

9) B. Mahapatra, K. K. Patel, Vidya, Piyush K. Patel, *Mater. Today: Proc.* 2021, **46**, 11, 5523-5529.

10) D.M. Wardhana, H. Mutsuda, Y. Tanaka, T. Nakashima, T. Kanehira, Sh. Maeda, M. Yamauchi, *Sustain. Energy Technol. Assess.* 2022, **50**, 101757.

11) D. Heo, J. Chung, G. Shin, M. Seok, C. Lee, S. Lee, *Energies* 2021, **14**, 1798.

12) Ch. Song, K. Xia, Zh. Xu, *Microelectron. Eng.* 2022, **256**, 111723.

13) L. Liu, X. Guo, Ch. Lee, *Nano Energy* 2021, **88**, 106304.

14) Q. Shi, Zh. Sun, Z. Zhang, Ch. Lee, *Research* 2021, **30**, 6849171,

15) M. Zhu, Zh. Yi, B. Yang, Ch. Lee, Nano *Today* 2021, **36**, 101016.

16) X. Zhao, H. Askari, J. Chen, *Joule* 2021, **5**, 1391-1431.

17) K.V. Kumar, M. Omer, S.S. Singh and M.A. Nayrah, *Analytics, Big Data, Security (FABS)* 2021,1-5

18) X. Wang, B. Yang, J. Liu, Y. Zhu, Ch. Yang, Q. He *Sci. Rep.* 2016, **6**, 36409.

19) K. Dong, X. Peng, Z. L Wang, *Adv. Mater.* 2020, **32**, 1902549.

20) T. Huang, C. Wang, H. Yu, H. Wang, Q. Zhang, M. Zhu, *Nano Energy*, 2015, **14**, 226-235.

21) M. Ha, J. Park, Y. Lee, H. Ko, *ACS Nano* 2015, **9** (4), 3421-3427.

22) L. Liu, X. Yang, L. Zhao, W. Xu, J. Wang, Q. Yang, Q. Tang, *Nano Energy* 2020, **73**, 104797.

23) J. Chen, S. K. Oh, N. Nabulsi, H. Johnson, W. Wang, J.H. Ryou, *Nano Energy* 2019, **57**, 670-679.

24) J. Liu, D. Yu, Z. Zheng, G. Huangfu, Y. Guo, *Ceram. Int.* 2021, **47**, 3573-3579.

25) X.S Zhang, M. Han, B. Kim, J.F Bao, J. Brugger, H. Zhang, *Nano Energy* 2018, **47**, 410-426.

26) S. H. Ji, W. Lee, J. S. Yun, *ACS Appl. Mater. Interfaces* 2020**, 12**, 18609-18616.

27) P. Zhang, W. Zhang, L. Deng, H. Zhang, *Nano Energy*, 2021, **87**, 106176.

26) Y. Su, C. Dagdeviren, R. Li*, Adv. Funct. Mater.*, 2015, **25**, 5320-5325.

27) T. Starner *IBM Syst. J.* 1996, **35**, 618.

28) B. Richter, J. Twiefel, J. Wallaschek, *Piezoelectric Equivalent Circuit Models*. In: Priya S., Inman D.J. (eds) *Energy Harvesting Technologies*, Springer, Boston, 2009**.**

29) J. Kim, B. L. Grisso, J. K. Kim, D. S. Ha, D. J. Inman, *IEEE Sensors App. Symposium* 2008, 122-127

30) Yang Y, Tang L., *J. Intell. Mater. Syst. Struct.* 2009, **20**, 2223-2235

31) C. A. Desor , E.S. Koh, *Basic Circuit Theory*, McGraw-Hill, 1969**.**

32) Analog Devices, "*Ideal Diode Bridge Controller*", *LT4321 datasheet*, Nov. 2013 [Revised Feb. 2014].

33) R. Srinivasan, U. Mangalanathan, U. Gandhi, L.R. Karlmarx, *IET Circuits Devices Syst.* 2019, **13**, 1078-1085.

34) L. Wassouf, E. Jamshidpour and V. Frick, 2020 *IEEE International Conference on Environment and Electrical Engineering and 2020 IEEE Industrial and Commercial Power Systems Europe (EEEIC / I&CPS Europe)* 2020,1-5.

35) G. Singh, Devices *for Integrated Circuit (DevIC)*, 2021, 383-387.

Chapter 6

Enhancing the voltage output of piezoelectric harvesters: a simulation study

Abstract

It is experimentally demonstrated that introducing pores in the structure of piezoelectric nanogenerators improves the output power of this class of energy harvesters. This is due to the Strain-confinement effect, which enables the porous piezoelectric nanogenerators to deliver higher output power when subject to an identical mechanical stress relative to the same structure without porosity. In this chapter with a theoretical introduction about dielectric constant of porous media, we used a finite element method to answer questions regarding the effect of pore's size, mechanical deformability, electrical break down voltage, etc. which can be used as guidelines to design more efficient porous piezoelectric energy harvesters.

6.1. Introduction

Realization of billions of transistors in integrated circuits (ICs) and electronic chips is now possible with state-of-the-art photolithography techniques and high-k dielectric materials. With the development of energy-efficient architectures for microprocessors, new horizons have been opened now regarding diversification of the application of low-cost low-power electronic devices that can range from wearable electronics to remote sensors.[1] As outlined in the previous chapter, multiferroic and piezoelectric energy harvesters have emerged as a practical energy source to power up the modern low-power electronic circuits.

Wearable, implantable electronics, and internet of things (IoT) are among the envisioned application areas, which need a lightweight, flexible, and cost-effective energy solutions beyond currently available batteries. The need for recharging in relatively short time intervals and the size of the packs limit the practicality of batteries for the above-mentioned applications. Therefore, alternative energy (electricity) sources have been considered and piezoelectric and multiferroic energy harvesters have emerged as a promising candidate for energy generation from mechanical vibrations or stray magnetic field, respectively. Piezoelectrics are especially interesting when environmental mechanical actuation is omnipresent. For instance, body-mounted and wearable electronic gadgets are constantly exposed to body motions. For distributed sensory networks for environmental monitoring purposes, the sensors are exposed to various forms of mechanical vibrations in the environment or stray magnetic field. The piezoelectric materials can convert the mechanical energy to electricity, hence piezoelectric energy harvesters, and the generated electricity can be stored in capacitors to be available for electronic circuit consumption. [5,6] Piezoelectric materials relevant for applications are typically polycrystalline whose net polarization is zero. Therefore, after their preparation piezoelectric are commonly poled under the application of a high external electric field to align dipoles of various domains.

The electromechanical coupling coefficient and relative permittivity are the two important criteria that should be optimized in the pursuit of high-performance piezoelectric energy harvesters. The electromechanical coupling coefficient is related to the capability of the material to convert mechanical strain to electricity and depends on the material's stiffness and piezoelectrical properties. The relative permittivity on the one hand determines the capacitance and the impedance of the comprising piezoelectric capacitor.[7-11] On the other hand, the relative permittivity affects the piezoelectric voltage coefficient, g, through

$$g_{ij} = \frac{d_{ij}}{\varepsilon_0 \varepsilon_{ij}} \qquad (6.1)$$

where i and j indices denote directions and d_{ij} and ε_{ij} are the piezoelectric charge coefficient and relative permittivity along the ij direction. The invers proportionality indicates that materials with lower relative permittivity exhibit larger piezoelectric voltage coefficient. On the contrary, piezoelectric materials typically show large relative permittivity. Consequently, their voltage coefficient can be small which negatively impacts their prospect in energy harvesting applications. Therefore, many efforts have been invested in reducing the relative permittivity (or the effective permittivity) of the piezoelectric in a device such as a capacitor with the aim to enhance the electrical output of the piezoelectric generators.

Porosity has been suggested as an efficient structuring tool to enhance the electrical power output of the piezoelectric harvesters because the introduction of pores inside the material can substantially decrease the effective relative permittivity. [12-13] Trapped pockets of air in the bulk of the piezoelectric material have a lower dielectric constant and as a result improve the piezoelectric response of the material by decreasing the overall capacitance of the generator. Introducing pores raises at least five questions:

i) Does the performance of the porous harvester depend on the size of the pores?
ii) How does the performance change with the degree of porosity?
iii) How does the presence of pores affect the electromechanical coupling?
iv) What is the influence of positioning the pores, surface versus bulk?
v) What is the effect that porosity play when poling the porous piezoelectric materials?

This chapter presents an attempt to answer these questions using three- (3D) and two-dimensional (2D) numerical simulations. After providing the required theoretical background, by the means of 3D finite element method (FEM) we numerically investigate the effect of pores in (polymeric) piezoelectric materials. Various porous scenarios have been considered, e.g., i) pores in the bulk and ii) pores on the surface of the piezoelectric. Furthermore, the influence of fractional porosity, pore geometry, and size have been modeled and studied for the optimization of the piezoelectric generators. The 2D FEM simulations have been performed to address the effect of porosity on the electrical properties of the piezoelectric, particularly on poling and break down voltage of the porous piezoelectric.

6.2. Model of dielectric constant for porous materials

The effect of porosity in reducing the "effective" relative permittivity of the materials can be understood through the textbook example below. A simple case of one spherical closed pore (cavity) inside a piezoelectric matrix is assumed. The effective relative permittivity of the structure is predominantly determined by interfacial polarization between pores and the matrix, which can be expressed as [15]:

$$P_s = P_{air} - P_m = (\varepsilon_{air} - \varepsilon_m)\varepsilon_0 E \qquad (6.2)$$

Where P_s, P_{air} and P_m are the polarization of the entire structure, pores and matrix, respectively, ε_0 is the permittivity of vacuum, ε_{air} and ε_m are relative permittivity of air and the piezoelectric matrices, and E is the external electric field.
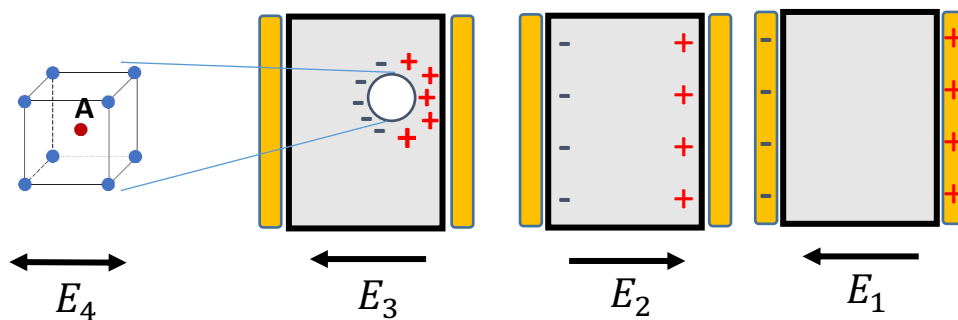
Figure 6.1. *Electric field components effecting on atom A at the center of a cavity in a dielectric material placed in a parallel plate capacitor, consisting E_1 as external applied field, E_2 as polarization field in opposite direction, E_4 as near field which vanishes in homogenous materials and E_3 as internal surface polarization in the cavity.*

The internal field in a dielectric material with a spherical cavity can be calculated as pictured in **Figure 6.1**. The electric field inside the dielectric material placed between the parallel plates of a capacitor can be

assumed as the superposition of four components, named E_1, E_2, E_3 and E_4, where E_1 is the field intensity at atom site "A" shown in **Figure 6.1** due to charges on the plates of the capacitor and can be written as follows:

$$E_1 = \frac{D}{\varepsilon_0}$$
$$D = P + \varepsilon_0 E \qquad (6.3)$$
$$E_1 = E + \frac{P}{\varepsilon_0}$$

where D is electric displacement. E_2 is the depolarization field due to charge density induced on the two sides of the dielectric given by:

$$E_2 = -\frac{P}{\varepsilon_0} \qquad (6.4)$$

and E_3 is the electric field due to polarization of charges on the surface of the cavity, which can be shown to be equal to $\frac{P}{3\varepsilon_0}$ as follows:
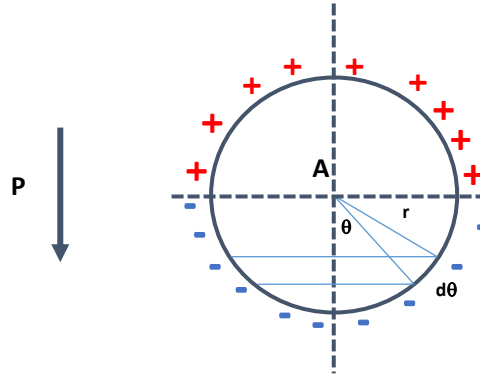
Figure 6.2. *Integration of accumulated surface charge on the outer surface of the cavity with the atom "A" at its center.*

As shown in **Figure 6.2,** the accumulated charge on the surface element between polar angel interval of θ and $\theta + d\theta$ can be written as:

$$dq = -P_s \cos \theta \, dA \qquad (6.5)$$

where θ is the angle reference to the polarization vector P and dA is the surface element. By placing a positive test charge at the atom site "A", the effective electric field can be calculated by the following integration:

$$E_3 = \int \frac{dq \cos\theta}{4\pi \varepsilon_0 \varepsilon_m r^2} = \int \frac{-P_s \cos\theta \; 2\pi r^2 \sin\theta \, d\theta}{4\pi \varepsilon_0 \varepsilon_m r^2} = \frac{-P_s}{2\varepsilon_0 \varepsilon_m} \int_0^\pi \cos^2 \theta \sin\theta \, d\theta = \frac{P_s}{3\varepsilon_0 \varepsilon_m} \qquad (6.6)$$

Additionally, E_4 is equal to $\frac{E}{3}$ since two third of the degrees of freedom of E vanishes due to the symmetry of the geometry with closed pores.[15] Thus, the total internal field E_i at atom site "A" can be written as the summation of the all above-mentioned components as follows:

$$E_i = E_1 + E_2 + E_3 + E_4 = E + \frac{P_s}{3\varepsilon_0 \varepsilon_m} + \frac{E}{3} \qquad (6.7)$$

The polarization per unit volume of the dielectric, P_s can be calculated using the Equations **6.7**:

$$P_s = N\alpha E_i = (\varepsilon_{air} - \varepsilon_m)\varepsilon_0 E \qquad (6.8)$$

where N, V and α are number of interfaces per unit volume, volume of the unit and interface polarizability, respectively. Using Equations **6.7** and **6.8**, one can write:

$$\alpha = \frac{1}{N}(\varepsilon_{air} - \varepsilon_m)\varepsilon_0 \frac{3\varepsilon_m}{\varepsilon_{air}+\varepsilon_m} = V(\varepsilon_{air} - \varepsilon_m)\varepsilon_0 \frac{3\varepsilon_m}{\varepsilon_{air}+\varepsilon_m} \qquad (6.9)$$

Finally, a revised form of Clausius-Mosotti relation can be employed as follows:

$$\frac{\varepsilon_{eff}-\varepsilon_m}{\varepsilon_{eff}+3\varepsilon_m} = \frac{N_{eff}\alpha}{3\varepsilon_0\varepsilon_m} \qquad (6.10)$$

Replacing α in equation **6.10** using equation **6.9** leads to equation **6.11** which relates the effective electric permittivity of the porous material, ε_{eff}, as a macroscopic quantity, to α_e, which is the microscopic quantity designating the polarizability of the material. [15,18]

$$\frac{\varepsilon_{eff}-\varepsilon_m}{\varepsilon_{eff}+2\varepsilon_m} = f \frac{\varepsilon_{air}-\varepsilon_m}{\varepsilon_{air}+3\varepsilon_m} \qquad (6.11)$$

with $f = NV$ designating the fractional porosity of the material.

6.3. Brief theory of piezoelectricity

Constitutional equations that describe the piezoelectric effect in materials are expressed in the form of vectors. Vector calculation is preferred for solving problems regarding electric, magnetic and mechanical stress fields, since it provides the amplitude and the directionality of variables in a compact and efficient form. In this approach, the material parameters governing the piezoelectric property will have a tensor form. Therefore, the simulations can provide a clearer insight and spatial information about the material under investigation. **Figure 6.3** demonstrates the six possible degrees of freedom in a typical problem in its general form, comprising three components parallel with each Cartesian coordinate directions of **X**, **Y,** and **Z** accompanied by three rotational directions designated by (4), (5) and (6).
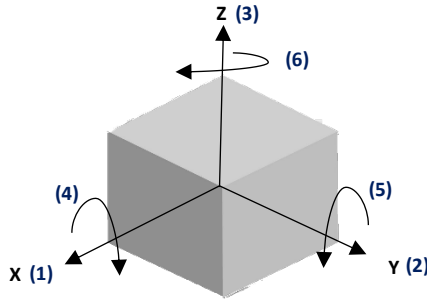
Figure 6.3. Demonstration of the six degrees of freedom used in matrix calculations.

The electrostatic equations governing the modeled device are as follows:

$$\nabla . D = \rho_V \tag{6.12}$$

$$E = -\nabla \phi \tag{6.13}$$

where ρ_V is volumetric charge density and D, E and ϕ are electric displacement, field, and potential respectively. A piezoelectric material is constantly under stress, T, or strain, s. Hence, it is necessary to consider the equations related to the structural mechanics of the material, which are expressed as:

$$\rho \frac{\partial^2 u}{\partial t^2} = \nabla . T + F_V \tag{6.14}$$

$$s = \frac{1}{2}[(\nabla u)^T + \nabla u] \tag{6.15}$$

where ρ, u and F_V are density of the material, mechanical displacement and the volumetric force, respectively. The Equations **6.14** and **6.15** are the differential forms of Newton's second law, that describes the material's deformation under an applies stress and strain, respectively. Finally, the equations governing piezoelectricity can be written either in stress-charge form as in Equation **6.16** or in strain-charge form as in Equation **6.17**:

$$\begin{pmatrix} T \\ D \end{pmatrix} = \begin{pmatrix} c_E & -e^T \\ e & \varepsilon_S \end{pmatrix} \begin{pmatrix} S \\ E \end{pmatrix} \tag{6.16}$$

$$\begin{pmatrix} S \\ D \end{pmatrix} = \begin{pmatrix} s_E & d^T \\ d & \varepsilon_T \end{pmatrix} \begin{pmatrix} T \\ E \end{pmatrix} \tag{6.17}$$

where T and S denote mechanical stress and strain, and D and E represent electrical displacement and electrical field, respectively. The stiffness matrix is given by c_E (in Pa) and e is the coupling matrix expressed in C/m^2. Coefficients of matrix ε_S are directional dielectric permittivity and e^T designates the transposed of matrix e. Similarly, the proportionality matrix in Equation **6.17** comprises s_E as compliance matrix at a constant electric field expressed in Pa^{-1} and ε_T is the electric permittivity at zero stress. Note that stress and strain are 6 by 1 matrices to include rotational mechanical deformation whereas electrical displacement and field are 3 by 1 vectors. In their most general form, the expanded form of the above-mentioned equations can be rewritten as in **6.18** and **6.19**:

$$\begin{pmatrix} T_{xx} \\ T_{yy} \\ T_{zz} \\ T_{yz} \\ T_{xz} \\ T_{xy} \end{pmatrix} = \begin{pmatrix} c_{E11} & c_{E12} & c_{E13} & c_{E14} & c_{E15} & c_{E16} \\ c_{E21} & c_{E22} & c_{E23} & c_{E24} & c_{E25} & c_{E26} \\ c_{E31} & c_{E32} & c_{E33} & c_{E34} & c_{E35} & c_{E36} \\ c_{E41} & c_{E42} & c_{E43} & c_{E44} & c_{E45} & c_{E46} \\ c_{E51} & c_{E52} & c_{E53} & c_{E54} & c_{E55} & c_{E56} \\ c_{E61} & c_{E62} & c_{E63} & c_{E64} & c_{E65} & c_{E66} \end{pmatrix} \begin{pmatrix} S_{xx} \\ S_{yy} \\ S_{zz} \\ S_{yz} \\ S_{xz} \\ S_{xy} \end{pmatrix} - \begin{pmatrix} e_{11} & e_{21} & e_{31} \\ e_{12} & e_{22} & e_{32} \\ e_{13} & e_{23} & e_{33} \\ e_{14} & e_{24} & e_{34} \\ e_{15} & e_{25} & e_{35} \\ e_{16} & e_{25} & e_{36} \end{pmatrix} \begin{pmatrix} E_x \\ E_y \\ E_z \end{pmatrix}$$

(6.18)

$$\begin{pmatrix} D_x \\ D_y \\ D_z \end{pmatrix} = \varepsilon_0 \begin{pmatrix} \varepsilon_{rS11} & \varepsilon_{rS12} & \varepsilon_{rS13} \\ \varepsilon_{rS21} & \varepsilon_{rS22} & \varepsilon_{rS23} \\ \varepsilon_{rS31} & \varepsilon_{rS32} & \varepsilon_{rS33} \end{pmatrix} \begin{pmatrix} E_x \\ E_y \\ E_z \end{pmatrix} + \begin{pmatrix} e_{11} & e_{12} & e_{13} & e_{14} & e_{15} & e_{16} \\ e_{21} & e_{22} & e_{23} & e_{24} & e_{25} & e_{26} \\ e_{31} & e_{32} & e_{33} & e_{34} & e_{35} & e_{36} \end{pmatrix} \begin{pmatrix} S_{xx} \\ S_{yy} \\ S_{zz} \\ S_{yz} \\ S_{xz} \\ S_{xy} \end{pmatrix}$$

$$\begin{pmatrix} S_{xx} \\ S_{yy} \\ S_{zz} \\ S_{yz} \\ S_{xz} \\ S_{xy} \end{pmatrix} = \begin{pmatrix} s_{E11} & s_{E12} & s_{E13} & s_{E14} & s_{E15} & s_{E16} \\ s_{E21} & s_{E22} & s_{E23} & s_{E24} & s_{E25} & s_{E26} \\ s_{E31} & s_{E32} & s_{E33} & s_{E34} & s_{E35} & s_{E36} \\ s_{E41} & s_{E42} & s_{E43} & s_{E44} & s_{E45} & s_{E46} \\ s_{E51} & s_{E52} & s_{E53} & s_{E54} & s_{E55} & s_{E56} \\ s_{E61} & s_{E62} & s_{E63} & s_{E64} & s_{E65} & s_{E66} \end{pmatrix} \begin{pmatrix} T_{xx} \\ T_{yy} \\ T_{zz} \\ T_{yz} \\ T_{xz} \\ T_{xy} \end{pmatrix} + \begin{pmatrix} d_{11} & d_{21} & d_{31} \\ d_{12} & d_{22} & d_{32} \\ d_{13} & d_{23} & d_{33} \\ d_{14} & d_{24} & d_{34} \\ d_{15} & d_{25} & d_{35} \\ d_{16} & d_{26} & d_{36} \end{pmatrix} \begin{pmatrix} E_x \\ E_y \\ E_z \end{pmatrix}$$

(6.19)

$$\begin{pmatrix} D_x \\ D_y \\ D_z \end{pmatrix} = \varepsilon_0 \begin{pmatrix} \varepsilon_{rT11} & \varepsilon_{rT12} & \varepsilon_{rT13} \\ \varepsilon_{rT21} & \varepsilon_{rT22} & \varepsilon_{rT23} \\ \varepsilon_{rT31} & \varepsilon_{rT32} & \varepsilon_{rT33} \end{pmatrix} \begin{pmatrix} E_x \\ E_y \\ E_z \end{pmatrix} + \begin{pmatrix} d_{11} & d_{12} & d_{13} & d_{14} & d_{15} & d_{16} \\ d_{21} & d_{22} & d_{23} & d_{24} & d_{25} & d_{26} \\ d_{31} & d_{32} & d_{33} & d_{34} & d_{35} & d_{36} \end{pmatrix} \begin{pmatrix} T_{xx} \\ T_{yy} \\ T_{zz} \\ T_{yz} \\ T_{xz} \\ T_{xy} \end{pmatrix}$$

In many cases, the geometrical and crystallographic symmetries in the piezoelectric materials result in the elimination of many of the coefficients, which greatly simplifies the above equations. By a simple

transformation, material properties in the stress-charge form equation can be modified to be used in the strain-charge form following:

$$c_E = s_E^{-1}$$

$$e = ds_E^{-1} \tag{6.20}$$

$$\varepsilon_S = \varepsilon_0 \varepsilon_{rS} = \varepsilon_0 \varepsilon_{rT} - ds_E^{-1} d^T$$

6.4. Defining the geometry of the device

Two different geometries are needed to evaluate the effect of porosity. First, a uniform piezoelectric cubic layer with $x = y = z = 440$ nm is defined. Two metallic electrodes (gold) are introduced at $z = 0$ and $z = 400$ nm. The thickness of the gold electrode is 10 nm. This geometry is considered as the benchmark device. Porous piezoelectric are realized by introducing pores inside the piezoelectric cube. Pores are generated by a computer script. It is assumed that the pores are spherical and randomly distributed in the piezoelectric matrix using a random number generator producing the coordinates of the center of the spheres. An extra condition is implemented to avoid merging pores by setting a minimum distance between every two neighbor pores using the following equation:

$$R_n + R_{n-1} \leq \sqrt{(X_n - X_{n-1})^2 + (Y_n - Y_{n-1})^2 + (Z_n - Z_{n-1})^2} \tag{6.21}$$

Equation **6.21** ensures that the algorithm always avoids any potential overlap between the neighboring spheres by guaranteeing a center-to-center distance that is larger than the sum of the radiuses. Fractional porosity, depending on the context, is controlled by incorporating more pores of the same size in the piezoelectric cube or by changing the pore size. For the samples with surface porosity an extra condition is implemented that the distance of the pores' center from the surface of the cube should be less than pore radius. The script is discussed in more detail in appendix A.

For all devices, the cube and spheres are partitioned into a fine mesh, and a finite element method analysis is used to solve the governing equations numerically using *COMSOL Multiphysics* at every node. A typical example of the simulated porous structure is given in **Figure 6.4a**. A time-domain FEM analysis is carried out by applying a time-variant pressure on the boundary of the geometry at z=440 nm. The applied pressure has a sine wave shape with the following amplitude and frequency:

$$P(t) = P_{amp} \sin(2\pi f_0 t) \tag{6.22}$$

where amplitude of P_{amp} and f_0 are $100 \frac{N}{m^2}$ and 100 Hz, respectively. The bottom of the cube is fixed with zero-displacement and the bottom electrode is electrically grounded. The side faces of the cube are free to move upon excretion of the pressure.

6.5. Simulation of electric response of a porous piezoelectric

A piezoelectric cube made of PVDF is considered and the effects of porosity on the voltage output in a comprising capacitor is studied.

a) $P(t)$ **b)**
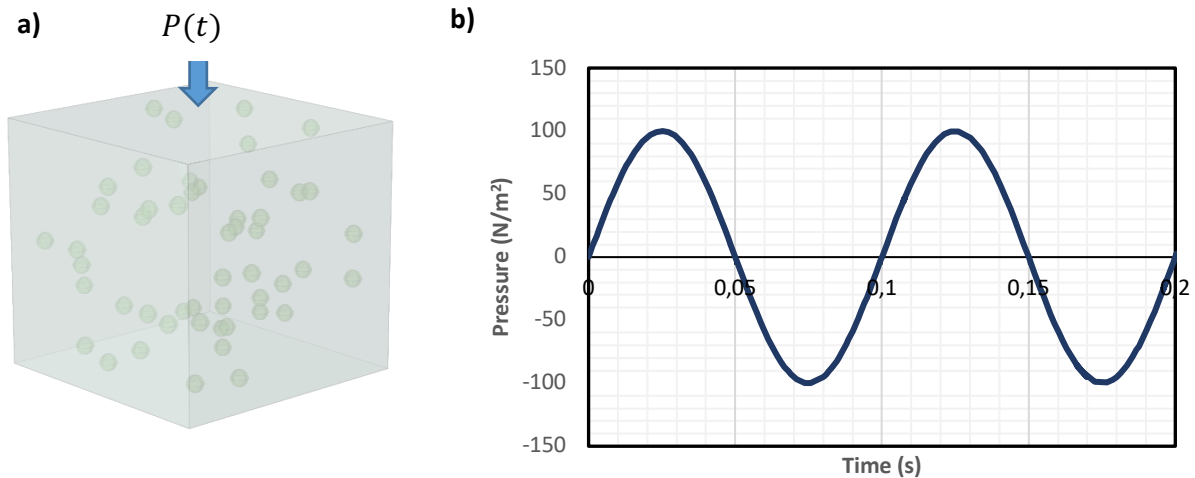
Figure 6.4. a) Geometry of a porous PVDF-based piezoelectric energy harvester. PVDF forms the matrix and the green spheres are the embedded air-filled pores. b) Temporal voltage response of the piezoelectric layer upon application of a periodic force to the top boundary of the cube.

6.6. Effect of pore size and fractional porosity

A representative example of the calculation for pore size of 20 nm and fractional porosity of 11.8 % is given in **Figures 6.5a** and **b**, where the structural internal stress (von Mises stress) and electric field, induced by the excreted external pressure have been shown, respectively. The figure indicates that local maximum spots appear at the interface between the pores and the polymer matrix, as indicated by the color-coded variable in both figures. The impact of these local extremums shall be discussed later in the context of structural and electrical breakdown. **Figure 6.5c** demonstrates the calculated voltage that the porous piezoelectric capacitor generates under a cyclic mechanical stress. The generated voltage is 180° out of phase with the applied stress because PVDF has a negative d_{33} charge coefficient of -30 pC/N.

Next, a series of simulations are performed with pores sizes of 10 nm, 20 nm, 25 nm, 30 nm, and 35 nm where for each case, the fractional porosity is systematically varied by increasing the number of pores inside the cube. Apart from pore size and the number of pores in the cube (fractional porosity) all the other parameters are kept constant. The piezoelectric response for two complete force cycles are calculated and the average peak-to-peak voltage for every case are obtained and compared in **Figure 6.6** where the *y*-axis shows the percentage of improvement in the generated voltage, V_{porous} , in comparison to the non-porous case, V_{bulk}, defines as percentage of improvement $= \frac{V_{porous} - V_{bulk}}{V_{bulk}} \times 100$.

a)   N/m²

b)   V/m

c)
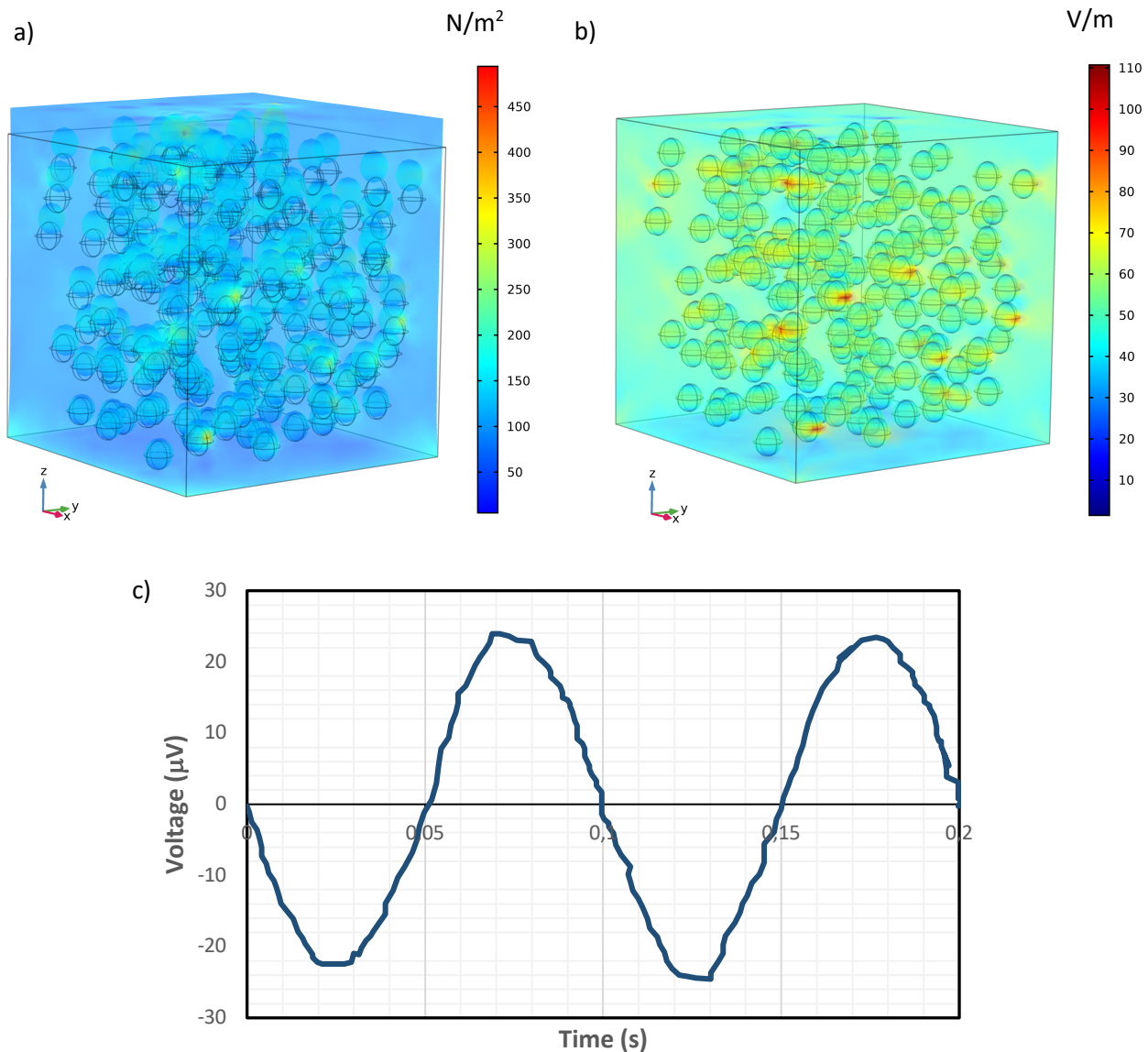
Figure 6.5. a) von-Mises Stress profile of a porous piezoelectric capacitor under mechanical stress. b) Electric field distribution of the device subject to a periodic external force along the Z axis. c) Voltage output of the porous piezoelectric device as a function of time.

Figure 6.6 shows that introducing pores increases the voltage output of a PVDF piezoelectric generator. However, the pore size has no influence on the increased voltage. The only influential parameter is the fractional porosity. Interestingly, the calculation shows 90% increase in the output voltage for a fractional porosity as low as 25%. It should be noted the curve shows a linear relationship with fractional porosity at low porosity. At higher porosity fractions, the increase in voltage output is superlinear. Hence, it can be argued that for very large porosity, approaching 50% and beyond, a much larger increase in the output voltage far beyond 100% is expected. Experimentally, similar nonlinear fractional improvement in the voltage output has been reported for PVDF-based nanofibers. It should be noted for similar nanofiber systems, a fractional increase of the order of 2000% has been reported for nanofibers with fractional porosities in excess of 45%.[14]
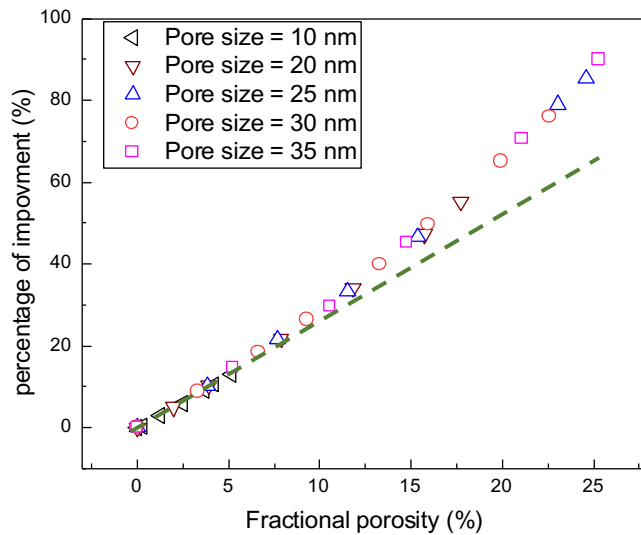
Figure 6.6. *Improved voltage output of porous piezoelectric PVDF energy harvesters as a functional fractional porosity for various pore sizes. The improvements are given in percentages compared with a non-porous sample.*

6.7. Poling and breakdown of porous piezoelectrics

Increasing the porosity of the structure increases the voltage output of the piezoelectric nanogenerator by means of improving its mechanical deformability and decreasing the effective dielectric constant of the medium. In simulations performed so far, it is assumed that the piezoelectric material, is readily poled and all dipoles are aligned, regardless of the presence of the pores. Experimentally, piezoelectric are polycrystalline where the crystallite has randomly oriented microscopic polarization thereby giving a net zero polarization to the as-prepared piezoelectric layers. Therefore, the piezoelectric is poled before any application to align all microscopic dipoles to achieve a macroscopic polarization. The poling process can become problematic for the porous piezoelectric because porosity reduces the effective electric breakdown voltage of the capacitor comprised of the porous material. The reduction in break down voltage is due to larger localized internal electric fields inside the pores and between two neighboring (almost touching) pores. The breakdown causes an electric short circuit and discharge of the accumulated electric charges between the electrodes. Hence, the issue of electrical breakdown deserves close attention as it has a deteriorative effect on the overall power output of the piezoelectric generator.

It is, however not clear how the electrical breakdown is affected by the pore size and fractional porosity, and how the breakdown can be mitigated. Understanding the breakdown fields requires inspection of the electric field distribution inside the porous structure. We adopt 2D models in this case because using 3D geometries for this purpose are computationally intensive. Moreover, the 3D computations do not contribute much to forming an understanding about the breakdown process. A schematic of the device is depicted in **Figure 6.7.** A 2D square slab of PVDF is assumed with $x = y = 440$ nm. The Pore size and position, porosity ratio and polymer matrix's geometrical properties are controlled by a script written in JAVA programming language in the method section of the finite element solver software package. The geometry-generating script can be found in the appendix B. The pore size varies from 10, 15, 20, 25 and 30 nm. For each pore size, various fractional porosities, ranging from ~ 7% up to ~44% are studied. We

note that the computation time substantially increases for samples with small pore sizes at high fractional porosities. A voltage ramp signal, **Figure 6.7a**, is applied to the top electrode of the device while the bottom electrode is grounded. The occurrence of local voltage breakdown is probed for various fractional porosities in the structure.
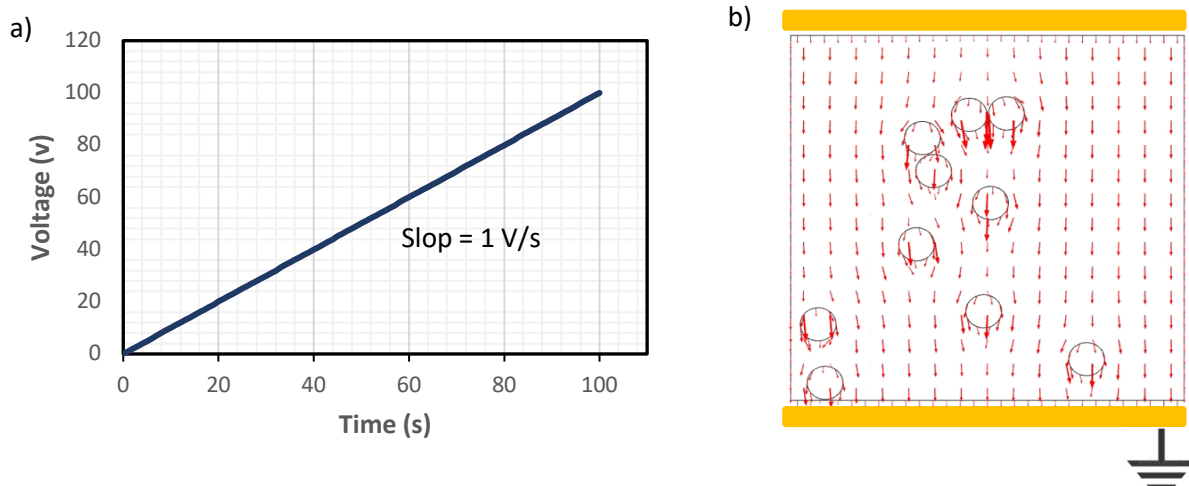
Figure 6.7. *2D simulation of the electrical breakdown of the capacitor. a) Applied ramp voltage signal to the top electrode is linearly increased in time while the bottom electrode grounded. b) The calculated electric field inside the porous piezoelectric. The arrows indicate the direction of the field and their length reflect the local field strength.*

A representative 2D simulation of the porous PVDF capacitor is given in **Figure 6.7b**. It is shown that the presence of pores in the matrix alter the uniformity and the direction of the electric field inside the porous piezoelectric, which is otherwise parallel to the z-direction in the non-porous piezoelectric. Furthermore, **Figure 6.7b** shows that the electric field perturbation is more pronounced at the vicinity of the pores. Interestingly, for two almost touching pores, the field strength shows a substantial increase. Hence it is clear that the breakdown in both pores (air cavities) and PVDF matrix should be considered.

In a series of simulations, occurrence of the electric breakdown is studied for various pore sizes and fractional porosities. It is assumed that the breakdown in pores occur when the field inside the pores is larger than the breakdown field of air, namely 3 MV/m. [16] The breakdown field of the PVDF piezoelectric matrix is around 420 MV/m. [17] **Figure 6.8a-c** demonstrate the field line distribution of the device under the test with three different porosity ratios. To improve the clarity, the x and y component of the electric field inside the matrix are depicted separately. **Figure 6.8d-f** demonstrate the E_x-component of the electric field while **Figure 6.8g-I** show the E_y-component. It is worth to mention that in the absence of the pores, no E_x-component exist inside the polymer and adding pores yields the appearance of a non-zero field along the x direction. Strong vertical electric field can be seen in **Figure 6.8a** very close to the border of the geometry of the simulated device. These strong local field can be attributed to the fringing field and were not taken into the account for the calculation of the breakdown field.
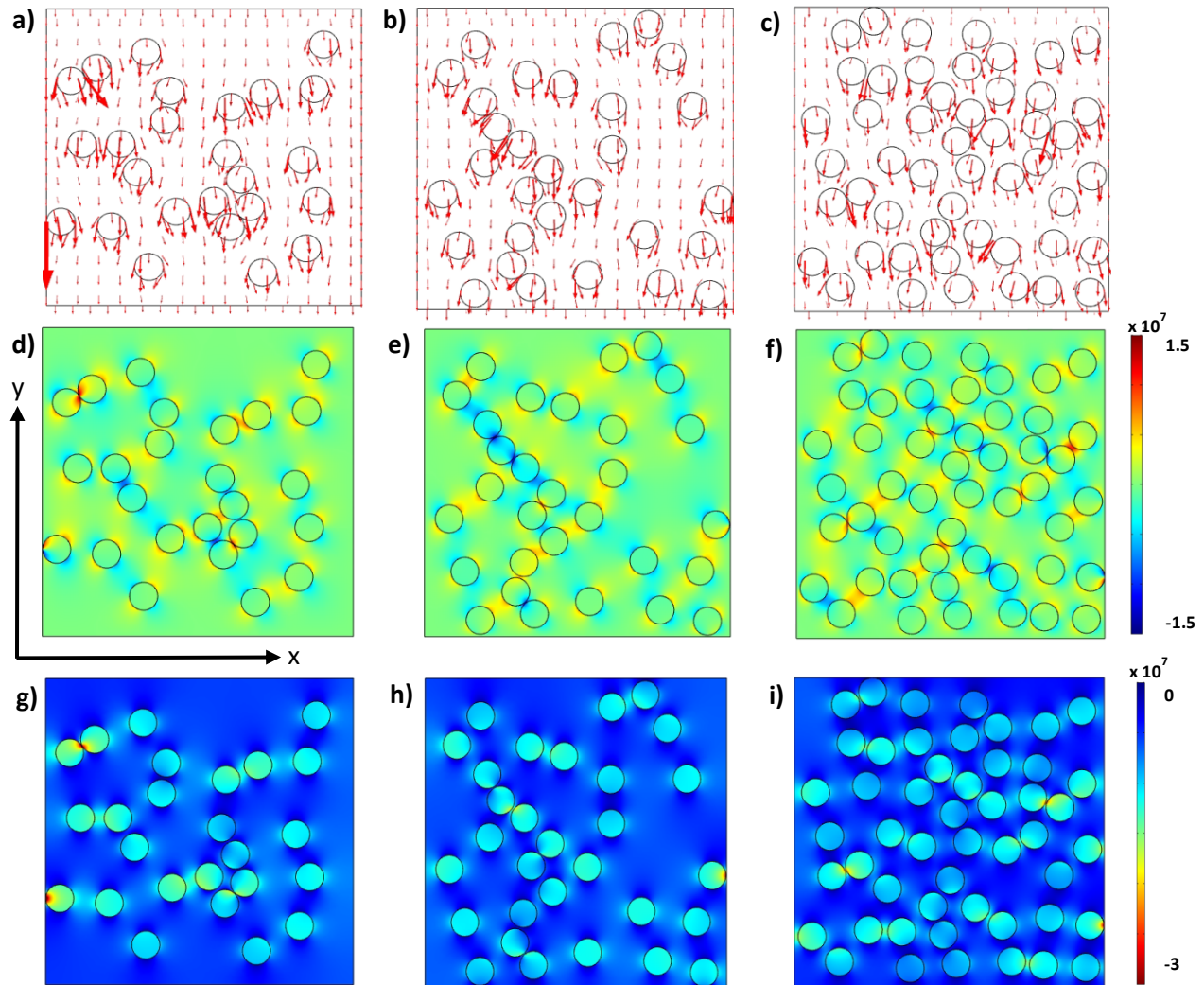
Figure 6.8. *a-c) Presence of 20nm porous disrupts the uniformity and direction of the vertical electric field inside the sample, length of the arrows indicates the strength of the field d-f) distribution of x component of electric field inside a polymeric matrix with trapped packets of air as a porous dielectric material with various porosity ratios. The voltage on the top electrode increased linearly from 0 to 100 V with the slope of unity while the bottom electrode kept grounded. g-i) Distribution of y component of electric field inside same devices. For the sake of clarity, the top and bottom electrodes are not shown.*

By increasing the number of pores, it can be observed that the uniformity of the internal field along the y axis deteriorates. This is due to appearance of fringing fields at the vicinity of the pores.

Finally, the breakdown voltage of the porous piezoelectric layer is studied as a function of fractional porosity and pore size. A summary of the simulation results is given in **Figure 6.9**. Two poling environments are considered, poling in air, and poling in vacuum. It is assumed that the sample undergoes breakdown as soon as a predefined threshold electric field is reached. The voltage at which the threshold field appears in the structure is recorded as the breakdown voltage.

For the poling experiment in air, the pores are filled with air, and the break down field of air is defined as the threshold electric field. As shown in **Figure 6.9a**, the breakdown field is very low for the porous

structure. Even for a factional porosity as low as 5%, the breakdown voltage is well below 1 V. Note that the breakdown voltage for samples with smaller pores is lower because of the smaller size of the pores. It is therefore challenging to pole porous piezoelectric samples in air. To mitigate this issue, we propose poling the sample in vacuum.

According to Paschen's law, the voltage necessary to create an arc across the gap, which is kept constant, decreases initially as the pressure is reduced, goes through a minimum and then substantially increases. Therefore, placing the samples in high vacuum, eliminates the issue with the breakdown of the air trapped in the pores. In this case, the breakdown voltage is limited by the breakdown field of the piezoelectric, which in this case is PVDF. **Figure 6.9b** shows the simulation results, by assuming a breakdown field of 5 x 10^{10} V/m for vacuum. It is shown that the breakdown voltage of the porous piezoelectric is increased by more than two orders of magnitude, reaching voltage as high as 50 V for samples with 45% porosity.

It is interesting to note that the breakdown voltage for samples with larger pores drops faster with fractional porosity in comparison with the samples with smaller pore size. As shown in **Figure 6.9**, the increase in the voltage output of the porous piezoelectrics is independent of the pore size. Hence, it is critical to create pores with as small size as possible to achieve the same enhanced performance but at the same time, also avoid breakdown issues.
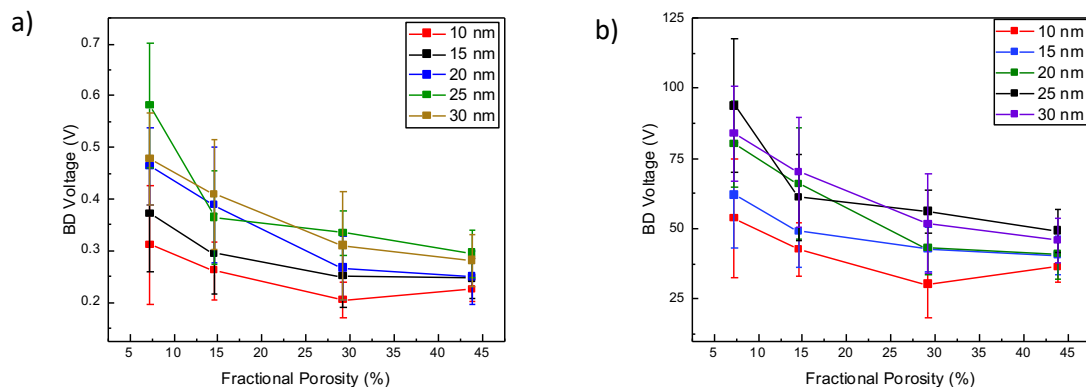
Figure 6.9. *Evaluation of breakdown voltage of the device under poling condition in a) air, and b) vacuum.*

6.7. Conclusion

In this chapter, we employed a finite element method to numerically investigate and compare the effect of different pore sizes and fractional porosity on the voltage output of porous piezoelectric energy harvesters based on PVDF. It is shown that the voltage increases with fractional porosity in a nonlinear manner. However, there is no dependency between the increased voltage and the pore size. Furthermore, it is shown that the presence of pores substantially alters the field distribution in the porous piezoelectric when the material undergoes poling condition. The simulations suggest that the poling of a porous piezoelectric should be carried out in vacuum. It is also shown that, at high fractional porosities, samples with large pore sizes may suffer from lower breakdown voltages. Hence it is recommended that high fractional porosity is achieved only with small pores.

Finally, these findings are highly beneficial for optimization of PVDF-based multiferroics, because of their relatively low magnetoelectric coupling coefficients, as shall be discussed in chapter 8. Creating a

porous PVDF-based multiferroic is suggested as way forward to substantially enhance the voltage response of the PVDF multiferroic devices.

Reference

1) S. K. Moore, *IEEE Spectr.* 2020, **57**, 24-30.
2) H. Khanbareh, K. de Boom, B. Schelen, R.B.N. Scharff, C.C.L. Wang, S. van der Zwaag, P. Groen, *Sens. Actuator. A Phys.* 2017, **263**, 554-562.
3) M. A. P. Mahmud, S. R. Bazaz, S. Dabiri, A. A. Mehrizi, M. Asadnia, M. E. Warkiani, Z. Wang, *Adv. Mater. Technol.* 2022, **7,** 2101347.
4) T. T. Biswas, J. Yu, V. A. Nierstrasz, *Sci. Rep.*, 2019, **9**, 18252.
5) U. Sezer, M. Koç, *Nano Energy*, 2021, **80**, 105567.
6) Y. -W. Chong, W. Ismail, K. Ko and C. -Y. Lee, *IEEE Sens. J.*, 2019, **19**, 9047-9062.
7) R. Kar-Gupta, T. A. Venkatesh, Appl. *Phys. Lett.*, 2007, **91**, 062904.
8) R. Kar-Gupta, T. A. Venkatesh, *J. Appl. Phys.* 2005, **98**, 054102.
9) C. Marcheselli, T. A. Venkatesh, *Appl. Phys. Lett.*, 2008, **93**, 022903.
10) S. Iyer, T. A. Venkatesh, *Appl. Phys. Lett.*, 2010, **97**, 072904.
11) S. Iyer, T. A. Venkatesh, *J Appl. Phys.*, 2011, **110**, 034109.
12) A.K. Yang, C.A. Wang, R. Guo,Y. Huang, *Appl. Phys. Lett.*, 2011, **98**, 152904
13) Z. Zhang, C. Yao, Y. Yu, Z. Hong, M. Zhi, X. Wang, *Adv. Funct. Mater.* 2016, **26**, 6760-6765.
14) M. M. Abolhasani, M. Naebe, M. Hassanpour Amiri, K. Shirvanimoghaddam, S. Anwar, J. J. Michels, K. Asadi, *Adv. Sci.* 2020, **7**, 2000517
15) L. Xing-Da, H. Zhi-Ling, Z. Bao-Xun, Zh. Ke-Tao, H. Peng, Zh. Kai-Lun, S. Wei-Li, *Appl. Phys. Lett.*, 2016, **108**, 102902
16) J. S. Rigden, *Macmillan Encyclopedia of Physics.* Simon & Schuster, **1996**: 353.
17) Y. Zhong, W. Jing, H. Yiliang, D. Chaoyong, Z. Kongjun, Q. Jinhao *Compos. Part A Appl. Sci.* 2020, **128**, 105675.
18) K. K. Karkkainen, A. H. Sihvola, K. I. Nikoskinen, *IEEE Trans Geosci Remote Sens*, 2000, **38**, 3, 1303-1308.
19) J. Yang, *An Introduction to the Theory of Piezoelectricity*, Springer Science and Business Media, N.Y., 2005
20) A.F. Bower, *Applied Mechanics of Solids*, CRC Press, Boca Raton, 2010.

Chapter 7

Measuring coupling coefficient in multiferroic materials using a lock-in technique

Abstract

Establishing of a standardised method that enables reliable measurement of the multiferroic coupling coefficient in an actual device, namely a multiferroic capacitor, would highly facilitate the research in the multiferroic devices. This necessity stems from the fact that thin-films of multiferroic materials typically show relatively small responses, which are susceptible to be overshadowed by the noise floor of the measurement setup, especially magnetoelectric interference, which can lead to inaccurate measurements with irreproducible coupling coefficient values. Hence, the theory of the magnetoelectric measurement is investigated in this chapter and some of the most common pitfalls are being discussed and provide several experimentally validated suggestions to avoid them.

7.1. Introduction

A thorough investigation of multiferroics requires various characterization techniques ranging from structural studies, microscopy and crystallography methods to magnetoelectric measurements, which provide insight into the magnetic, ferroelectric and dielectric behaviour of the material under different mechanical, electrical and magnetic external stimuli at different temperatures. [1-4]

Optical and scanning probe microscopy techniques shed light on the crystallographic structure structural symmetries, phase transitions, and existing relaxations states. Magnetoelectric measurements provide extensive information about the magnetization, polarization, and strain behaviour of the structure and provide proof of the existence of cross-coupling between the mechanical, electrical, and magnetic properties in this class of materials. The magnetoelectric coupling coefficient is, therefore, the most interesting physical property since it directly addresses the strength of the coupling between electrical polarization and the magnetization state of the underlying material at the macroscopic scale. [3-6]

Measurement of the magnetoelectric coupling coefficient is not straightforward. Among the various measurement methods, the dynamic method possesses higher accuracy and lower noise susceptibility. [7-10] This chapter outlines the challenges during a reliable direct magnetoelectric measurement and provides a reliable platform for magnetoelectric measurement using the dynamic method.

7.2. Dynamic method of magnetoelectric effect measurement

The primary figure of merit for a typical multiferroic material is the strength of the magnetoelectric coupling, derived from the dynamic method of measurement of the magnetoelectric effect. In this method, as can be seen in **Figure 7.1**, an AC magnetic field is superimposed on a DC magnetic field and is applied to the device under the test. Each field component has a separate coil with an independent driving current source. While DC magnetic field coils are fed by a DC power supply, a function generator supplies the small-signal voltage to the AC coils to generate a time-variant magnetic field. The magnetically induced voltage developed across the DUT is very small and susceptible to magnetoelectric interference. Therefore, a lock-in amplifier is used to increase the signal-to-noise ratio of the measurement by narrowing the frequency window where we are looking for the device response.[11]
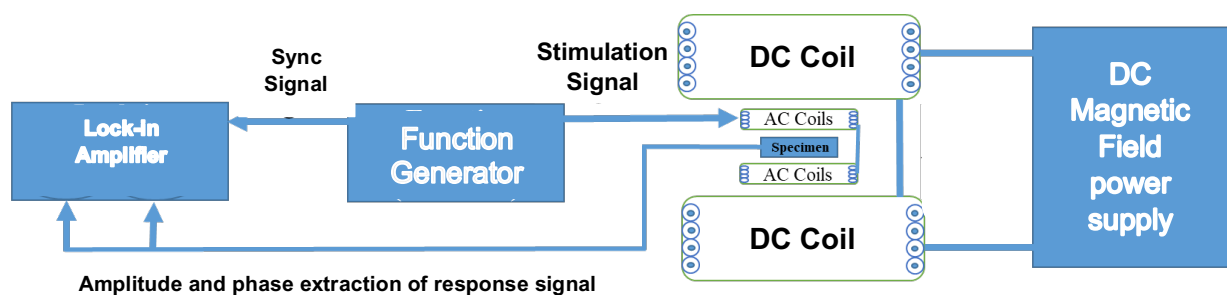
Figure 7.1. *Block diagram of a magnetoelectric measurement setup.*

The magnetoelectric coefficient is inherently a tensor with embedded spatial information in the following form:

$$\alpha_{ME\,ij} = \begin{pmatrix} \alpha_{ME_{xx}} & \alpha_{ME_{xy}} & \alpha_{ME_{xz}} \\ \alpha_{ME_{yx}} & \alpha_{ME_{22}} & \alpha_{ME_{yz}} \\ \alpha_{ME_{zx}} & \alpha_{ME_{zy}} & \alpha_{ME_{zz}} \end{pmatrix} \tag{7.1}$$

This can be simplified as follows:

$$\alpha_{ME\,ij} = \frac{\partial E_j}{\partial H_i} = \frac{1}{d}\frac{\partial V}{\partial H} = \frac{1}{d}\frac{V_{ac}}{H_{ac}} \tag{7.2}$$

Where α_{ME} is the magnetoelectric coupling coefficient, E and H are electric and magnetic fields, respectively, and d is the thickness of the DUT film. Additionally, V_{ac} and H_{ac} are amplitude of small-signal and time-variant developed voltage and magnetic stimulation, respectively.

7.3. Lock-in technique

The magnetoelectric response of the multiferroic material is vulnerable to magnetic induction, electromagnetic interference and ambient noise. This is especially important since a time-variant magnetic field is present in the measurement setup and can generate an electromotive force in any closed loop of currents in the cables. Based on Lenz law, the induced electromotive force has an opposite polarity and can overshadow the device response and deteriorate the accuracy of the reported values. In the simplified scenario depicted in **Figure 7.2**, a sine-wave voltage signal is generated by the function generator. This signal is fed to a current amplifier. The amplified signal supplies the coil to generate an AC magnetic field, along with its axis of symmetry in the Z direction.
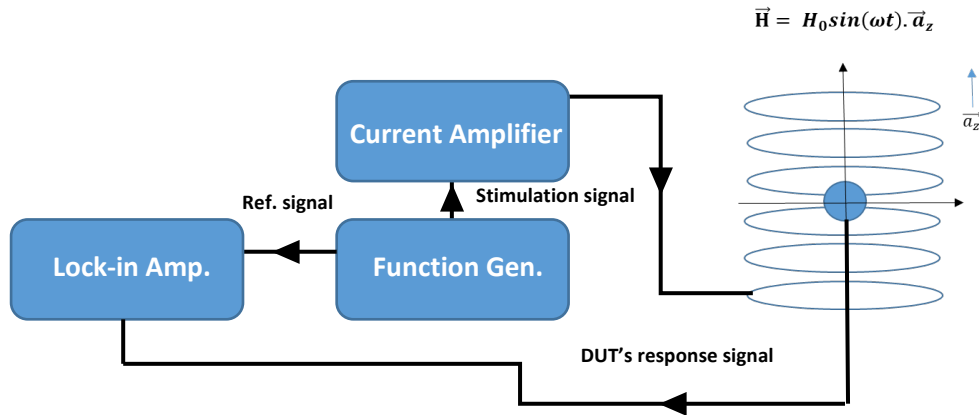
Figure 7.2. *Schematic of the excitation of the AC magnetic field and the measurement setup.*

we have:

$$H_{ac}(t) = \mu_0 n I(t) = \mu_0 n I_0 cos(\omega_{ac} t) \tag{7.3}$$

$$B_{solenoid}(t) = \mu_r H(t) = \mu_r n I(t) = \mu_r \mu_0 n I_0 cos(\omega_{ac} t) \tag{7.4}$$

Where I is the pumped current into the coil, n is the number of turns of the coil per unit of length, B is the density of magnetic flux and ω_{ac} is the angular frequency of the excitation of the coil, set by the function generator. Equations **7.3** and **7.4** relate the generated magnetic field with the injected current to the coil. It can be seen that the frequency of electric excitation of the coil and generated magnetic field are identical. Moreover, the magnetic flux, φ passing through closed loops made by current-carrying cables generates an electromotive force with a phase lag of $\pi/2$ as follows:

$$\varphi = \oiint \vec{B}.d\vec{A}$$
$$\tag{7.5}$$
$$emf = -N\frac{d\varphi}{dt}$$

We can rewrite the v_{ac} as the summation of the magnetoelectric response of the DUT and the electromotive force generated across the terminals of the DUT as follows:

$$v_{ac}(t) = emf + v_{ME}(t) \tag{7.6}$$

The above equation pinpoints the necessity of proper signal conditioning and noise suppression strategies for a reliable measurement. Using proper shielding and minimizing the length of the cables are two immediate solutions to mitigate the effect of cross-talks and ambient noise. Additionally, the lock-in amplification method is a suitable technique to reduce the noise floor in the measurement by truncating the DUT's response in a narrow frequency spectrum window of interest. The technique is mainly relying on the orthogonality of triangular functions by multiplication of an instance of the stimulation signal and the measured device response. The instantiated signal is called the reference signal and is the duplicate of the function generator voltage as shown in **figure 7.3**.
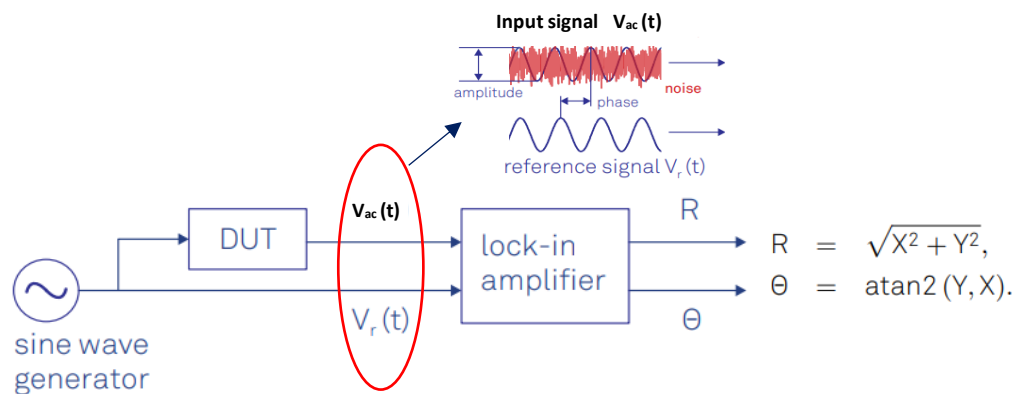
Figure 7.3. *Working principle of a lock-in amplifier to improve the SNR by truncating the frequency window. Figure has been adapted from reference 11.*

The above figure shows the DUT's response, $v_{ac}(t)$ and reference signal $v_r(t)$ as inputs of the lock-in amplifier. The instrument multiplies these two signals and extracts the phase and amplitude components

of $v_{ac}(t)$ that has the exact frequency of $v_r(t)$. In the frequency domain, the product of two signals can be written as follows [11]:

$$Z(t) = R.e^{i[(\omega_s-\omega_r)t+\theta]} + R.e^{i[(\omega_s+\omega_r)t+\theta]} \tag{7.8}$$

A high-order low-pass filter effectively eliminates the second term in equation **7.8**, and only the first term remains. We are looking for device response at the frequency of stimulation, assuming $\omega_s = \omega_r$, the time-dependent term vanishes, and we have:

$$Z = R.e^{i\theta}$$

$$X = Re\ \{Z\}\ = R\ cos\theta \tag{7.9}$$

$$Y = Im\ \{Z\}\ = R\ sin\theta$$

The lock-in amplifier reports the demodulated signal in the form of R and Θ as amplitude and phase or pair of X and Y as real and imaginary parts of the signal in a complex plane. Equation set **7.9** explains the relations between these parameters.

Although the above derivation theoretically ensures the validity and accuracy of the reported value of the magnetoelectric response of the device in terms of suppression of noise floor in frequencies other than the frequency of interest, we still need to be cautious to discern between the magnetoelectric response of the device and generated electromotive force at the frequency of the time-variant magnetic field, H$_{ac}$. Rewriting the equations **7.3, 7.5** and **7.6** in Euler notation, assuming N=1, we have:

$$H_{ac}(t) = \frac{H_{ac}}{2}(e^{i\omega_{ac}t} + e^{-i\omega_{ac}t})$$

$$emf = -\frac{d\varphi}{dt} = -\frac{d(B.A)}{dt} = -A\frac{d(\mu H)}{dt} = -\mu A\frac{dH}{dt} = -\mu A\frac{H_{ac}}{2}\ i\omega_{ac}\ (e^{i\omega_{ac}t} - e^{-i\omega_{ac}t}) \tag{7.10}$$

$$v_{ME}(t) = \frac{V_{ME}}{2}(e^{i\omega_s t} + e^{-i\omega_s t})$$

and:

$$v_{ac}(t) = v_{ME}(t) + emf = \frac{V_{ME}}{2}(e^{i\omega_s t} + e^{-i\omega_s t}) - \mu A\frac{H_{ac}}{2}\ i\omega_{ac}\ (e^{i\omega_{ac}t} - e^{-i\omega_{ac}t}) \tag{7.11}$$

Multiplication of the above signal with the reference signal with an arbitrary amplitude of 2 for simplification results in:

$$v_r(t) = V_r\cos\ (\omega_r) = e^{i\omega_r t} + e^{-i\omega_r t} \tag{7.12}$$

$$Z(t) = v_{ac}(t) \times v_r(t) = (e^{i\omega_r t} + e^{-i\omega_r t})\left[\frac{V_{ME}}{2}(e^{i\omega_s t} + e^{-i\omega_s t}) - \mu A\frac{H_{ac}}{2}\ i\omega_{ac}\ (e^{i\omega_{ac}t} - e^{-i\omega_{ac}t})\right]$$

$$= \frac{V_{ME}}{2}\left(e^{i(\omega_r+\omega_s)t} + e^{i(\omega_r-\omega_s)t} + e^{-i(\omega_r-\omega_s)t} + e^{-i(\omega_r+\omega_s)t}\right)$$

$$- \mu A\frac{H_{ac}}{2}\ i\omega_{ac}(e^{i(\omega_r+\omega_{ac})t} + e^{i(\omega_r-\omega_{ac})t} + e^{-i(\omega_r+\omega_{ac})t} + e^{-i(\omega_r-\omega_{ac})t}) \tag{7.13}$$

Since the reference signal is duplicated from the function generator, $\omega_r = \omega_{ac} = \omega_s$, eliminating higher frequency components by a digital filter, we can rewrite as follows:

$$Z = V_{ME} - i\ \mu AH_{ac}\omega_{ac} \tag{7.14}$$

Note that the time dependency of Z vanishes, and what remains are a DC term as the real part of Z and an imaginary part, which is a linear function of the frequency of stimulation, H_{ac}. According to these

calculations, only the real part of the demodulated value by the lock-in amplifier should be considered as the magnetoelectric response of the device, as the imaginary part is the contribution of *emf* that appears in the measured voltage. **Figure 7.4** demonstrates the self-consistency of the above derivation for a multiferroic capacitor made of thin films of 38 wt% PMMA-grafted $Co_{0.7}Fe_{2.3}O_4$ nanoparticles in P(VDF-TrFE) as prepared in the previous chapter.
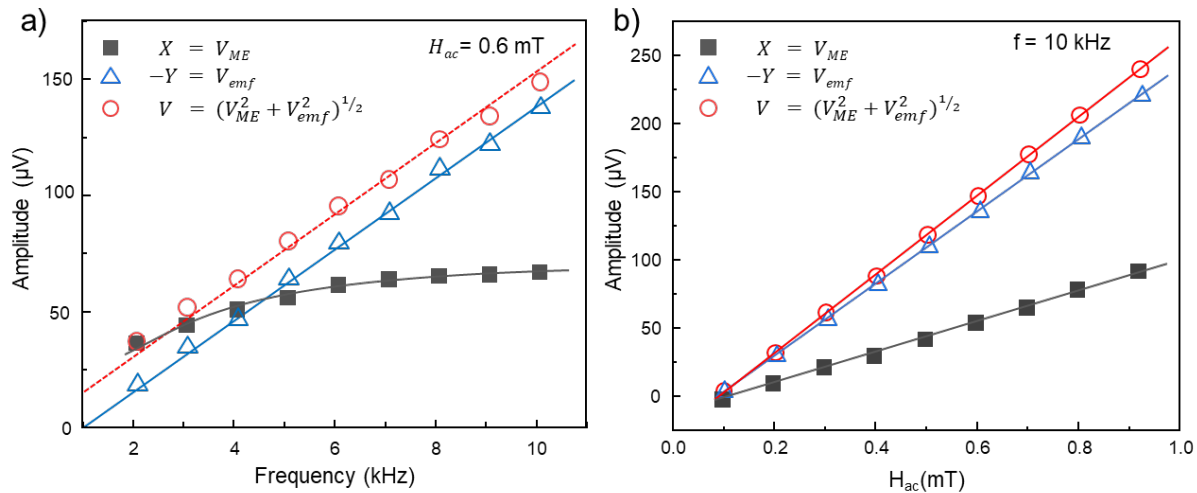
Figure 7.4. *Frequency and amplitude response of the measured voltage by the lock-in amplifier at two different H_{ac}. The Y component shows perfect linearity with frequency, as expected from theory. The X component shows a saturating trend with increasing frequency. The correct value for ME voltage is the X component. Applied H_{dc} is 0.5 T.*

According to **Figure 7.4a**-**b,** *emf* shows a very distinctive linear relation both with frequency and amplitude of the time-variant magnetic field stimulation, whereas the *X* component of the demodulated signal, which indicates the magnetoelectric response of the multiferroic response, doesn't show a strong correlation to the frequency sweep of the H_{ac}.

Further evidence for a distinction between the magnetoelectric component and inductive voltage built-up of the lock-in amplifier's demodulated voltage can be shown in **Figure 7.5**. The linear relation between the *Y* component of the demodulated voltage and $H_{ac}\omega_{ac}$ is pictured in **Figure 7.5a**, while **Figure 7.5b** presents the magnetoelectric voltage built-up on plates of the multiferroic capacitor. The magnetoelectric component of the demodulated voltage initially shows a relatively sharp linear dependency, and as $H_{ac}\omega_{ac}$ increases, *X* shows saturating behaviour.

7.4. Magnetic field generation

Measurement of the magnetoelectric response of multiferroic materials requires the generation of the superposition of DC and AC magnetic fields. This is due to the inherent nonlinear behaviour of magnetization in magnetic materials. **Figure 7.6** shows the magnetization curve of *$Co_xFe_{3-x}O_4$* for various values of *x* at room temperature. Besides the effect of the composition ratio of cobalt and iron on the hysteresis behaviour of the magnetization curves, from the slope of the curves, it is apparent that the DC bias point of the system directly affects the amplitude of the small-signal response.
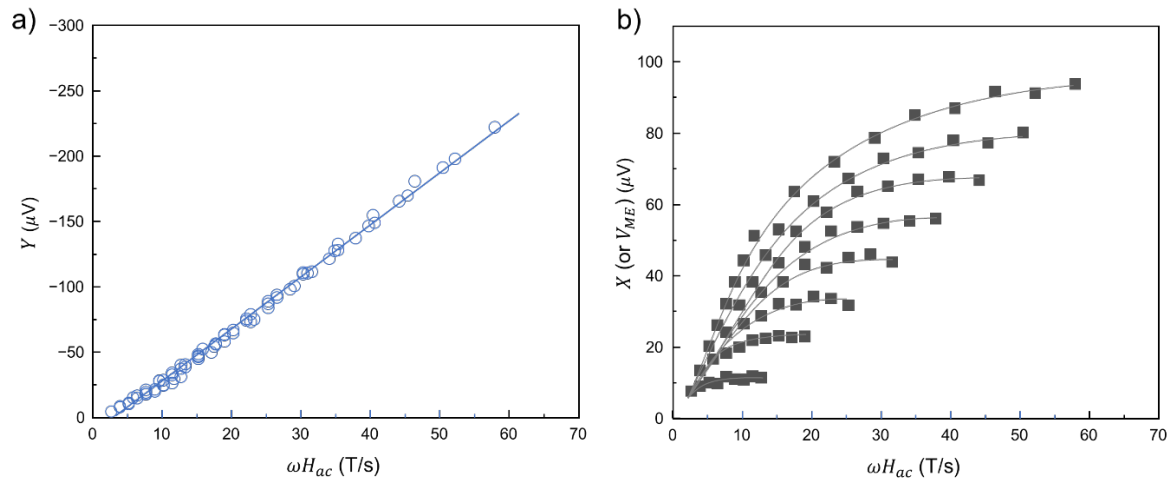
Figure 7.5. *Internal consistency check of the measurement protocol. A) Collapse of the Y components of the demodulated signals with ωH_{ac} indicating its inductive nature. The solid line is a linear fit to the data. B) The same plot obtained for the X component of the demodulated signal, which is the magnetoelectric coupling voltage, V_{ME}. The lines are provided as a guide to the eye.*

The above derivations and presented plots highlight the importance of distinguishing between the magnetoelectric response of the DUT and induced electromotive force in the cables to prevent misleading conclusions about the strength of the magnetoelectric coupling and its coefficient, α_{ME}.

Two sets of coils are needed for AC and DC fields. The DC field is usually generated by an electromagnet fed by a DC source. While the AC magnetic field is made by a Helmholtz coil supplied by a time-variant current source. We had two different approaches to studying the magnetoelectric effect in the materials in our research. Initially, we used a commercial magnet system with integrated AC and DC coils for magnetic field generation and embedded measurement hardware. The system uses superconductors in the cryogenic regime, and it is capable of generating a DC field of up to 14 Tesla.
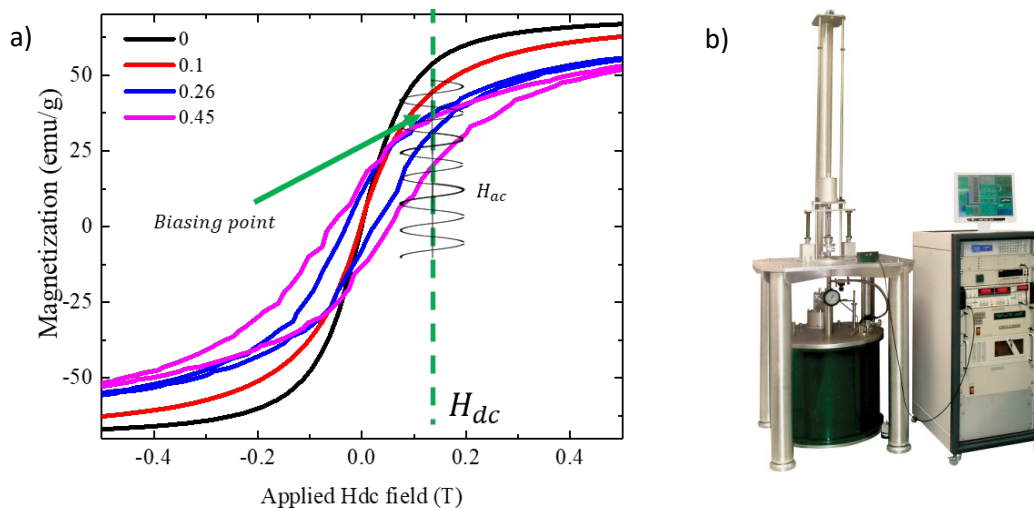
Figure 7.6. *Magnetization curve of $Co_xFe_{3-x}O_4$ at 300 K, The DC bias point alters the device response to small-signal perturbation b) commercial measuring instrument used for M-E measurements adopted from website of "cryogenic Limited ©".*

A LABVIEW virtual instrument software controls the operation and logs the measurement data. **Figure 7.6b** shows the system. The sample can be mounted on the probe and inserted into the magnet chamber. However, this approach did not lead to reliable measurements because the multiferroic test was not a standard and predefined measurement routine in the above-mentioned instrument. We made extra wiring and cable connections to perform the measurement. This, in turn, made the setup prone to magnetoelectric interference and deteriorated the signal-to-noise ratio. Alternatively, we also made a semi-custom setup for M-E measurements to mitigate the effect of unwanted magnetoelectric interference and fringe fields since the complexity of the commercial instrument can be avoided.

7.5. Custom setup

It is common to use a Helmholtz coil to generate a time-variant magnetic field. **Figure 7.7** shows a Helmholtz coil consisting of two identical circular windings with radius R which are placed at the distance of R from each other. Coils are connected in a series circuit.
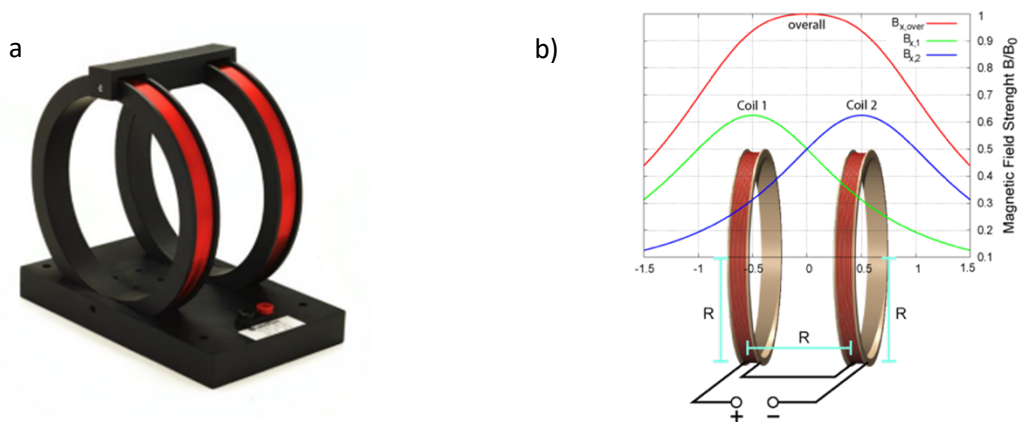
Figure 7.7. a) a Helmholtz coil with the housing b) field strength profile of the individual coils and total equivalent magnetic field at the centre. figures a and b are adopted from references 12 and 13, respectively.

It can be observed from the above figure that the superposition of the magnetic field generated by each of the coils results in a uniform magnetic field, exactly at the centre of the Helmholtz coil along the *Y*-axis. Therefore, the sample should be accurately placed in the middle of the coil for valid measurement. 3D simulation using the finite element method confirms the assumption of uniformity of the magnetic field, as is shown in **Figure 7.8**, below. Red arrows indicate the vectors of magnetic flux density, B.

7.5.1. Impedance lowering

Each Helmholtz coil has a current to magnetic field conversion coefficient, which depends on its geometrical parameters and the number of turns of the coils. This coefficient defines the ratio between the pumped current to the coils and the amplitude of the generated magnetic field at the centre of the setup. This conversion ratio for the Helmholtz coil that we used for our custom setup was 26.5 G/A. To generate a time-variant magnetic field, all we need is an AC source to supply the Helmholtz coil in the desired frequency range. We know that the impedance of a coil is frequency-dependent and increases linearly with respect to the frequency:

$$Z_L(f) = j2\pi f L = j\omega L \tag{7.10}$$
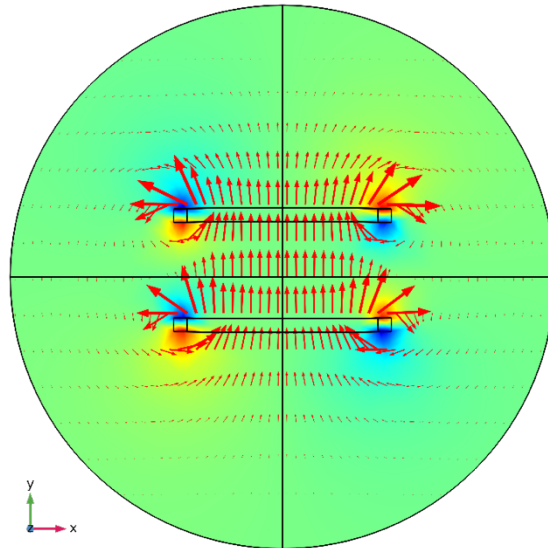
Figure 7.8. *COMSOL Multiphysics simulation of the Helmholtz coil with arrows indicating the magnetic flux density of the generated field.*

Where *L* and ω are the inductance of the coil and angular frequency of the supplied current. Using an LCR meter, the inductance of the coil was measured, and it demonstrates a relatively stable behaviour in our desired frequency window between 1 kHz to 10 kHz, as can be seen in the **Figure 7.9a**.

Consequently, one can conclude that the impedance of the Helmholtz coil, as expressed in equation **7.10**, is a single variable function of the frequency of the excitation with a linear trend. **Figure 7.9** shows the impedance spectroscopy measurement of the coil, which confirms this relation. It can be seen that at 10 kHz, the impedance is about 1300 Ω. This implies that the generation of a magnetic field with a given amplitude at a higher excitation frequency requires higher voltage in comparison to a lower frequency.
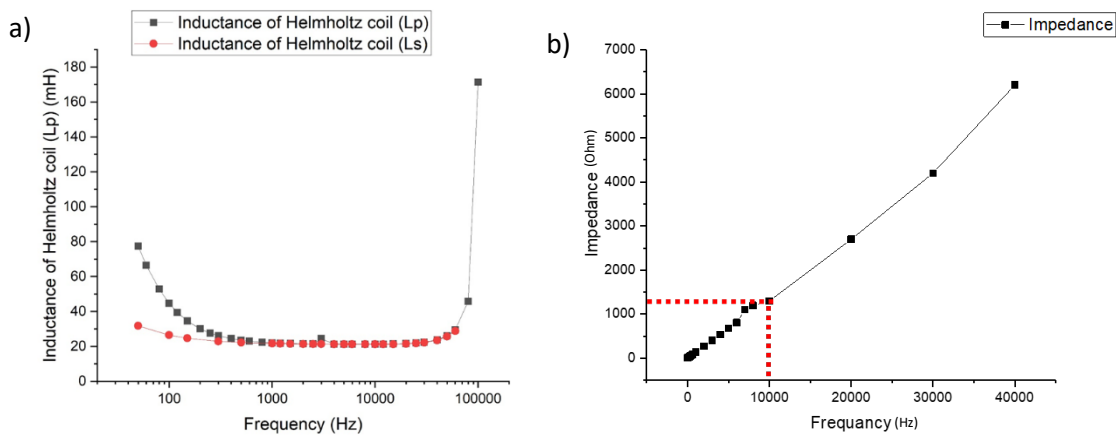
Figure 7.9. *a) Inductance of the Helmholtz coil measured to be at around 20 mH in desired frequency window. b) Impedance spectroscopy measurement of the coil, equal to 1300 Ω at 1 kHz.*

Assuming the compliance voltage of the current source to be equal to ±30 V, at 10 kHz we have:

$$V_{max} \, Z(10KHz) \approx 1300 \, \Omega$$

$$I_{max} = \frac{V_{max}}{Z(10KHz)} = 30/1300 = 0.0237 \, A \tag{7.11}$$

$$H_{ac-Max} = 0.0237 \, [A] * 26.5 \, [G/A] = 0.6 \, [G]$$

We need to generate at least 25 G for reliable magnetoelectric measurement in the interval of 1 kHz to 10 kHz. A straightforward solution for the above-mentioned problem is to compensate for the reactive component of the coil's impedance by utilizing a capacitor bank placed in series with the coil in the circuit. The impedance of a capacitor can be written as:

$$Z_C(f) = -j\frac{1}{2\pi f L} = -j\frac{1}{\omega c} \tag{7.12}$$

Since the imaginary component of the impedance of a capacitor is negative, the total impedance of the circuit depicted in **Figure 7.10a** seen from current source terminals, can be written as:

$$Z_{Total}(\omega) = R_1 + R_2 + j\omega(L_1 + L_2) - j\frac{1}{\omega c_s} \tag{7.13}$$

Where L_1, L_2, and R_1, R_2 are inductance and parasitic resistance of the coils, respectively. At the resonance frequency, the imaginary part of the above equation vanishes, and the total impedance of the circuit reduces to merely the resistive component. To fulfil the resonance condition, we should have:

$$C_s = \frac{1}{\omega^2(L_1+L_2)} \qquad f_{resonance} = \frac{1}{2\pi\sqrt{(L_1+L_2)}} \tag{7.14}$$

As these equations suggest, by choosing a proper series capacitor bank at any frequency, the total impedance can be greatly lowered to increase the pumped current to the Helmholtz coil at a constant voltage. **Figure 7.10b** and **c** reflect this fact for 740 Hz and 7.2 kHz.
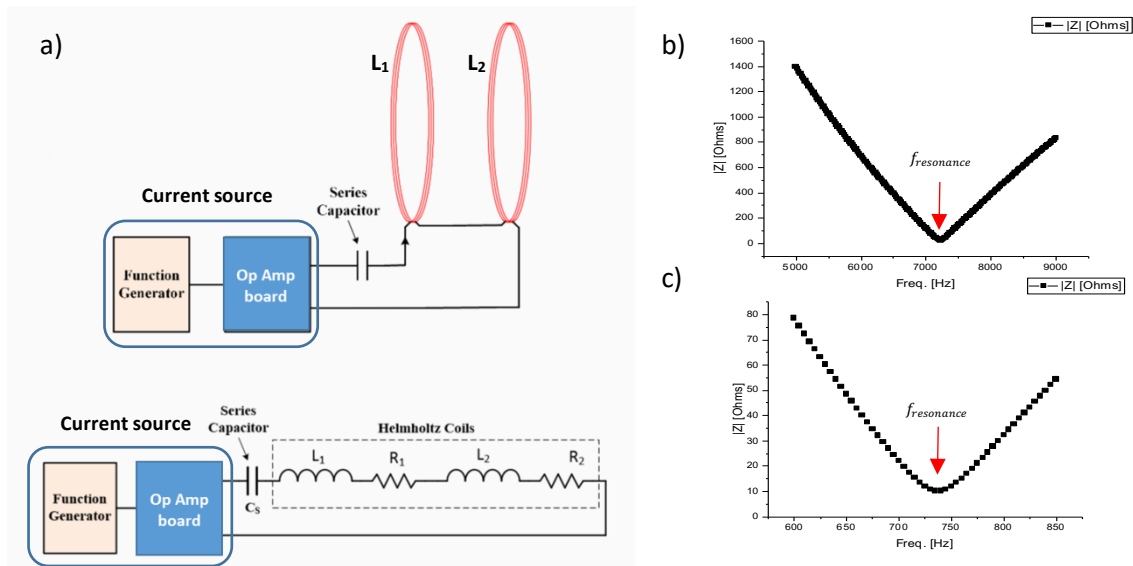
Figure 7.10. *a) Equivalent circuit of the Helmholtz coil with capacitor bank in the circuit, adapted from reference 15 b) and c) Impedance versus frequency of the circuit with different capacitor bank.*

We made several capacitor banks for various resonance frequencies in the 1 kHz to 10 kHz intervals. This technique helps to supply sufficient current for the Helmholtz coil to generate the required AC magnetic field in the desired frequency window. It can be done by overcoming the issue of the frequency dependence of the impedance of the coils. **Figure 7.11** shows several capacitor banks assembled on prototyping PCBs. Each board has its corner frequency when used in the circuit. Parallel and series combinations of the boards are also suitable for generating different resonance frequencies.
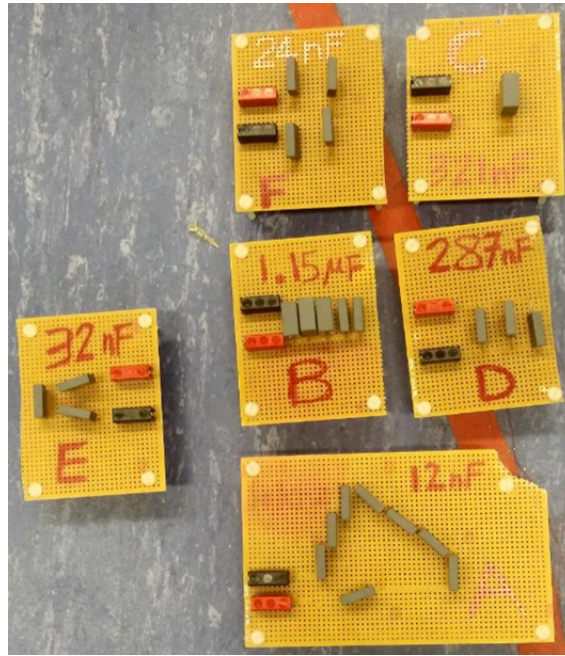
Figure 7.11. *Capacitor banks for various resonance frequencies, made using prototyping PCBs.*

Board Name	Capacitance [nF]	Max Current [A]	Resonance frequency [Hz]	Max Magnetic Field [G]
A	1500	1.702	739	45.18
B	320	1.62	1399	43.11
C	288	1.6	1480	42.48
D	32	1.24	4455	32.92
E	24	1.206	5119	32.01

Table 7.1. *A summary of the capacitance of each auxiliary board and some of the circuit parameters of the system. The resonance frequency of the boards and the sunk current and generated magnetic field can also be found in this table.*

7.5.2. Current source

In the previous section, we highlight the importance of reducing the impedance of the Helmholtz coil by adding a capacitor bank to generate sufficient magnetic field for the ME measurement. Besides the technique that we used, choosing a current source, which is capable of supplying enough current to the coil, is also important. Regarding the electromagnetic conversion ratio of the used Helmholtz coil which was 25 G/A, it was necessary to pick an AC source that could supply a few amperes in frequency intervals

between 1 kHz to 10 kHz. This was not available in the Lab. An available programmable AC current source from Keithley model 6220 could only supply 0.1 A, which is well below the requirement.

a)

b)
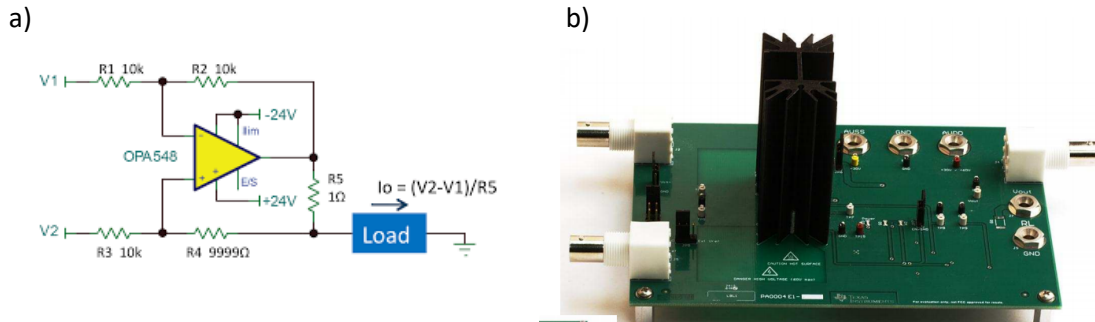
Figure 7.12. *a) Schematic of the non-inverting OPA548, adopted from reference 16. b) The circuit board of the Opamp output stage*.

To address this demand, we used an in-house made power supply to feed the coils. The design consists of a unity-gain power operational amplifier from Texas Instruments, **Figure 7.12,** a function generator, and a voltage amplifier. OPA548 is a high output current, high output voltage Opamp which can operate with a ±30V rail-to-rail voltage source and can source and sink up to 3 A in a continuous fashion.[12] **Figure 7.13** depicts the schematic of the completed setup. The output of the OPA548 Board can sink and source enough current to generate an adequate AC magnetic field required for the ME measurement. An Oscilloscope continuously monitors the wave shape of the delivered current to guarantee that the signal distortion remains in an acceptable range. A fan is mounted on the OPA548 current stage in the final setup to avoid any overheating issues during the high-power operation. **Figure 7.14** shows the custom setup used during the measurements.
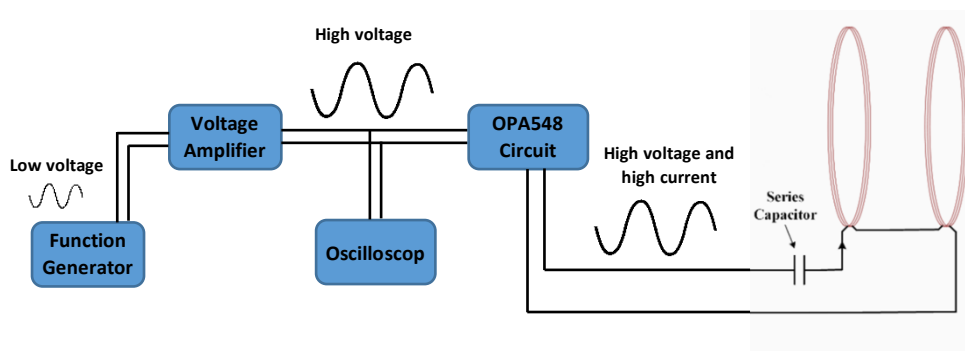
Figure 7.13. *Block diagram of the excitation circuit of the Helmholtz coil, schematic adapted from reference 15*
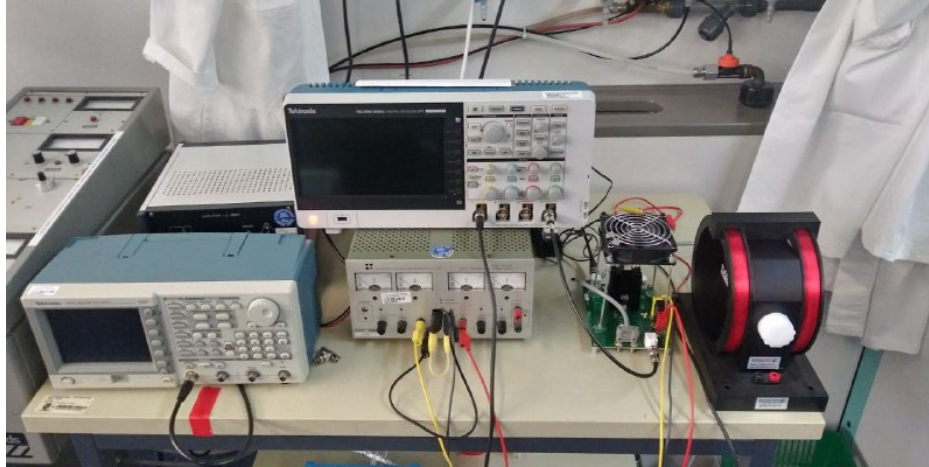
Figure 7.14. *Complete setup for M-E measurement for zero DC magnetic field.*

Reference

1) R. Ramesh, N. Spaldin, *Nat. Mater.* 2007, **6**, 21–29.
2) Y. Huang, D. Nikonov, C. Addiego ,R. Chopdekar, B. Prasad, L. Zhang, J. Chatterjee, H. Liu, A. Farhan, Y. Chu, M. Yang, M. Ramesh, Z. Qiu, B. Huey, C. Lin, T. Gosavi, J. Íñiguez, J. Bokor, X. Pan, , I. Young, L. Martin, R. Ramesh, *Nat. Commun.* 2020, **11**(1), 2836.
3) K. P. Jayachandran, J. M. Guedes, H. C. Rodrigues, *Sci. Rep.* 2020, **10**, 1276.
4) Ideue, T., Kurumaji, T., Ishiwata, S. and Tokura, Y. *Nat. Mat.* 2017, **16**(8), 797-802.
5) M. Mostovoy, Nat. *Mater* 2008, **7**, 269–270.
6) T. Lottermoser, D. Meier, *Phys. Sci. Rev.* 2021, **6**, 2, 20200032.
7) J. T. Evans, S. P. Chapman, S. T. Smith, B. C. Howard and A. Gallegos, Proceedings *of ISAF-ECAPD-PFM* 2012, 1-4.
8) M. M. Vopson, Y. K. Fetisov, G. Caruntu, G. Srinivasan *Materials* 2017, **10**, 963.
9) M. Mahesh Kumar, A. Srinivas, S. Suryanarayana, G. Kumar, T. Bhimasankaram, *Bull. Mater. Sci.*, 1998 **21**(3), 251-255.
10) G. V. Duong, R. Groessinger, M. Schoenhart, D. Bueno-Basques, *J. Mag. Mag. Mater.*, 2007, **316**, 2, 390-393.
11) White Paper Principles of lock-in detection and the state-of-the-art Zurich Instruments Release ,2016.
12) Lake Shore Cryotronics, Helmholtz Coils MH-6 application note, Revision A, 2 May 2014.
13) H . Shirzadfar, S. Dohani, M. Ghaedi, B. Edalati, *Int. J. Biosen. Bioelectro*. 2019, **5**, 179-183.
14) Texas Instruments, OPA548 datasheet, Oct. 1997 [Revised Dec. 2019].
15) "A CCEL instruments", A CCEL instruments *website*, accessed 26 July 2022, <https://www.accelinstruments.com/Helmholtz-Coil/Helmholtz-Coil.html >.
16) B. Trump, The Signal, A compendium of blog posts on op amp design topics, Texas instruments website, accessed 26 July 2022, <https://www.ti.com/amplifier-circuit/op-amps/the-signal-ebook.html?keyMatch=THE%20SIGNAL>

Chapter 8

Solution-processed multiferroic thin-films with large room-temperature magnetoelectric coupling

Abstract

A sizeable room-temperature magnetoelectric response, α_{ME}, in the absence of an external DC magnetic field has been theoretically predicted for polymer multiferroic nanocomposites (PMCs) thin-films, but its experimental realization has remained elusive. Here, by finite-element method simulation, we elucidate the detrimental effect of nanoparticle agglomeration in reducing α_{ME} and demonstrate that by grafting polymethylmethacrylate (PMMA) chains from the surface of the nanoparticles, uniform dispersion even in sub-micrometer thin-films is experimentally obtained because of the full miscibility of PMMA chains with the piezoelectric polymer matrix. The maximized interfacial interactions between the nanoparticles and the polymer matrix led to the experimental demonstration of large α_{ME} values in solution-processed thin-films. These results open the path towards flexible and printable multiferroic electronic devices for sensing and memory applications.

8.1. Introduction

The magnetoelectric coupling coefficient, α_{ME}, characterizes the strength of magnetoelectric interaction $\alpha_{ME} = \frac{\partial E}{\partial H_{AC}} = \frac{\partial V}{t \partial H_{AC}}$ (in mV Oe^{-1}cm^{-1}), where V is the voltage induced by a time-varying (AC) magnetic field, H_{AC}, across the multiferroic film with thickness, t. Single-phase multiferroic materials are rare and exhibit small α_{ME} values of just a few mV Oe^{-1} cm^{-1}, which is usually observed only at low temperatures.[1-5] Bi-phase multilayers have been suggested to increase the coupling coefficient [6-9], where the magnetoelectric coupling arises from interfacial stress-strain transfer between the ferroic phases.[9-12] Thick-films of piezoelectric polymers deposited on highly magnetostrictive materials, hence bilayer heterostructures, show relatively large α_{ME} values of several thousands of mV Oe^{-1} cm^{-1}. For many of the envisioned applications of the multiferroics composites as in sensors, memories, tunable filters, and signal processing technologies, thin-films are needed, which enable miniaturization and integration of the multiferroic devices with the semiconductor optoelectronic devices. However, thin-films of bilayer heterostructures exhibit weak magnetoelectric coupling and small α_{ME} values due to substrate clamping and thus not suited for the envisioned applications.[13]

Polymer-based multiferroic composites (PMCs) comprising a piezoelectric polymer with magnetic nanoparticle fillers have been proposed theoretically as a promising route toward obtaining significant coupling coefficients comparable to that of the bilayer heterostructures.[14] Advantageously, α_{ME} values as high as a thousand mV Oe^{-1}cm^{-1} have been predicted for PMCs at room temperature,[15-17] which if realized in thin-films, would render the PMCs viable for integrating with microelectronic devices. There has been a flurry of activities on the realization of PMCs, typically centered around mixing a piezoelectric polymer such as poly(vinylidene fluoride), PVDF, or its random copolymer with tri-fluoroethylene, P(VDF-TrFE), with various magnetic nanoparticles. In sharp contrast with the theoretical predictions, coupling coefficients of just a few mV Oe^{-1} cm^{-1}, as summarized in **Table 8.1**, have been experimentally reported so far.[14, 18-24] As it stands, the simple approach of mixing the piezoelectric polymer with different magnetic nanoparticles, regardless of their type and magnetic properties, has so far produced only weak α_{ME} values that are measured only when an external DC magnetic field is applied, and only when a thick-films of several tens of micrometers is used. Demonstration of large α_{ME} values in thin-films of PMCs in the absence of an external DC magnetic field, i.e., a self-biased PMC, is yet to be reported.

We suggest that the lack of PMC thin-films and the reported reduced coupling coefficient for PMCs thick-films are due to the agglomerations of magnetic nanoparticles in the piezoelectric polymer matrix. The reported theoretical predictions outline, although implicitly, that the prerequisite for achieving a significant α_{ME} coupling coefficients value in the PMCs is a uniform dispersion of isolated magnetic nanoparticles.[17] A careful inspection of the structural analysis for the reported PMCs, as in the **Table 8.1**, reveals that a uniform distribution of the individual nanoparticles (not their aggregatess) in the piezoelectric matrix is lacking in all reports. Therefore, the first step is to understand the origin of agglomeration even when colloidally stable nanoparticles are used.

PMCs are typically fabricated by mixing some types of magnetic nanoparticles with the PVDF or P(VDF-TrFE) in the solution phase. The nanoparticles, in general, tend to agglomerate due to their high surface area and van der Waals interactions.[73] For non-magnetic nanoparticles, interparticle interactions are mitigated using well-established and relatively simple interfacial modifications by small molecular organic surfactants (or ligands) such as oleic acid. For the magnetic nanoparticles, the agglomeration tendency is enhanced via the magnetic interactions, which are operational on larger length scales than the length of the ligand. For the reported PMCs (see for instance the references in **Table 8.1**, conventional surface modification using a small organic ligand only renders the nanoparticle colloidally stable in the solution

phase, whereas obtaining a uniform dispersion in the matrix requires compatibilization of the nanoparticles with the piezoelectric polymer matrix. Since the bare nanoparticles or those modified with small organic ligands are immiscible with the polymer matrix, upon processing the composite either from solution phase or melt, phase separation sets in, and large clusters of agglomerated nanoparticles are inevitably formed. The agglomeration is facilitated further by the inter-particle magnetic interactions. Besides reducing α_{ME} value, the agglomeration also increases the dielectric loss and the leakage current through the composite, thereby impeding a reliable evaluation of α_{ME}.[20] Circumventing agglomeration and achieving uniform dispersion of the magnetic nanoparticle is, therefore, the key to obtaining large α_{ME} in PMC thin-film and should be addressed.

Composite	α_{ME} (mV Oe^{-1} cm^{-1})	Reference
P(VDF-TrFE)/CoFe$_2$O$_4$(NPs)	40	21
P(VDF-TrFE)/CoFe$_2$O$_4$(NPs)	41.3	22
P(VDF-TrFE)/No$_{0.5}$Zn$_{0.5}$Fe$_2$O$_4$(NPs)	1.35	23
Polyurethane/Fe$_3$O$_4$(NPs)	11.4	24
Polyurethane/Ni (NPs)	6	24
PVDF/CoFe$_2$O$_4$ (NPs)	11.2	25
P(VDF-TrFE)/CoFe$_2$O$_4$ (NPs)	0.04	26
Dimines 2CN&OCN/CoFe$_2$O$_4$(NPs)	0.8	27
P(VDF-TrFE)/CoFe$_2$O$_4$ (NPs)	6.5	28
P(VDF-TrFE)/Fe$_3$O$_4$ (NPs)	0.8	28
P(VDF-TrFE)/Zn$_{0.2}$Mn$_{0.8}$Fe$_2$O$_4$	0.16	16
Polyurethane/Fe$_3$C (NWs)	2.4	29
P(VDF-TrFE)/Ni(NWs)	2.3	30
P(VDF-TrFE)/FeO(OH) (nanosheet)	0.4	28
P(VDF-TrFE)/SmFeO$_3$	45	31
PVDF/(Bi$_{0.5}$Ba$_{0.25}$Sr$_{0.25}$)(Fe$_{0.5}$Ti$_{0.5}$)O$_3$	18.4	32
PVDF/MnFe$_2$O$_4$	6.4	33
PVDF/BiFeO$_3$-CoFe$_2$O$_4$	22.18	34
PVDF/BaTiO$_3$	22.2	35
PVDF/CNT/CoFe$_2$O$_4$	16.7	36
P(VDF-TrFE)/ Terfenol-D	38	37
P(VDF-TrFE)/CoFe$_2$O$_4$	18.5	38
P(VDF-TrFE)/ Fe$_{72.5}$Si$_{12.5}$B$_{15}$	65	39
P(VDF-TrFE)/ Zn$_{0.2}$Co$_{0.8}$Fe$_2$O$_4$	17	40
P(VDF-TrFE)/ NiFe$_2$O$_4$	90	41

Table 8.1. *Overview of the magnetoelectronic (ME) coefficient of different polymer-based multiferroic composites.*

8.2. Operation mechanism and the detrimental effect of agglomeration
8.2.1. Finite-element simulations

Finite-element simulations of multiferroic composite have been performed Using COMSOL. To that end, three modules related to the electromagnetic, piezoelectric, and mechanical properties have been employed. Hence, the program solves Maxwell's equations at every grid point. The mechanical properties of the composite are calculated using the differential form of Newton's second law equation **8.2** and strain displacement equation **8.3**:

$$\rho \frac{\partial^2 u}{\partial t^2} = \nabla.s + F_V \tag{8.2}$$

$$\epsilon = \frac{1}{2}(\nabla u)^T + \nabla u. \tag{8.3}$$

Where u is displacement, ρ is material's density, s is stress, F_V is volumetric force and ϵ is strain. The Maxwell equations and the mechanical properties are coupled through the piezoelectric properties of the composite following:

$$S = s_E T + d^T E \tag{8.4}$$

$$D = \varepsilon_0 \varepsilon_{rT} E + dT \tag{8.5}$$

Where S is strain, T is stress, ε_0 is vacuum permittivity, s_E, ε_{rT} and d are compliance, relative permittivity, and piezoelectric charge coefficient tensors. Equations **8.4** and **8.5** describe strain-charge coupling.

To simulate the composite microstructure, spherical nanoparticles are assumed as in **Figure 8.1 a**. For the case of the PMMA-grafted nanoparticles, the surface of the particles is covered with an elastic non-magnetic shell with Young's modulus that is similar to that of PMMA, as shown in **Figure 8.1 b**. A P(VDF-TrFE) cube is defined wherein the nanoparticles are randomly distributed, **Figure 8.1 c**. It should be noted that the position of the nanoparticles is not fixed between different simulation runs and is fully randomized. The only constraint that is imposed is that the nanoparticles do not infuse. The following parameters were used for the piezoelectric phase:

Relative permittivity:

$$\varepsilon_{rT} = \begin{pmatrix} 7.4 & 0 & 0 \\ 0 & 9.3 & 0 \\ 0 & 0 & 7.6 \end{pmatrix} \tag{8.6}$$

Compliance:

$$sE = \begin{pmatrix} 3.781 & -1.482 & -1.724 & 0 & 0 & 0 \\ -1.482 & 3.781 & -1.724 & 0 & 0 & 0 \\ -1.724 & -1.724 & 10.92 & 0 & 0 & 0 \\ 0 & 0 & 0 & 14.28 & 0 & 0 \\ 0 & 0 & 0 & 0 & 11.1 & 0 \\ 0 & 0 & 0 & 0 & 0 & 11.1 \end{pmatrix} \times 10^{-10} \text{ Pa}^{-1} \tag{8.7}$$

Piezoelectric coupling:

$$d = \begin{pmatrix} 0 & 0 & 0 & 0 & 0 & 0 \\ 0 & 0 & 0 & 0 & 0 & 0 \\ 13.58 & 1.476 & -33.8 & 0 & 0 & 0 \end{pmatrix} \times 10^{-12} \text{ CN}^{-1} \tag{8.8}$$

Density: 1780 kg/m^3.

The electrical potential is calculated by placing two gold electrodes on the cube's top and bottom (along the z-direction). The construct is then placed in an air cube, **Figure 8.1c**, (or sphere, as will be discussed later) to evaluate the magnetoelectric response of the composite. A voltmeter is connected to the Au electrodes to record the generated V_{AC} as a function of the time-varying magnetic field (H_{AC}). To obtain the multiferroic response, a uniform, time-varying H_{AC} is required. To that end, a solenoid, **Figure 8.2a**, is defined to create a uniform time-varying magnetic field at its center using an AC. An air sphere is defined around the solenoid, wherein the field is calculated. A snapshot of the magnetic field is shown in **Figure 8.2b**. The used geometry generates a uniform, time-varying magnetic field. At last, the PMCs, as defined in **Figure 8.2c**, are placed in the center of the solenoid, as shown in **Figure 8.2c**. Subsequently, the current passing through the solenoid is varied, and the action of the resulting magnetic field on the PMC is calculated.

a) Cobalt-ferrite nanoparticles

b) PMMA-grafted nanoparticles

c) Nanoparticles embedded in P(VDF−TrFE) matrix
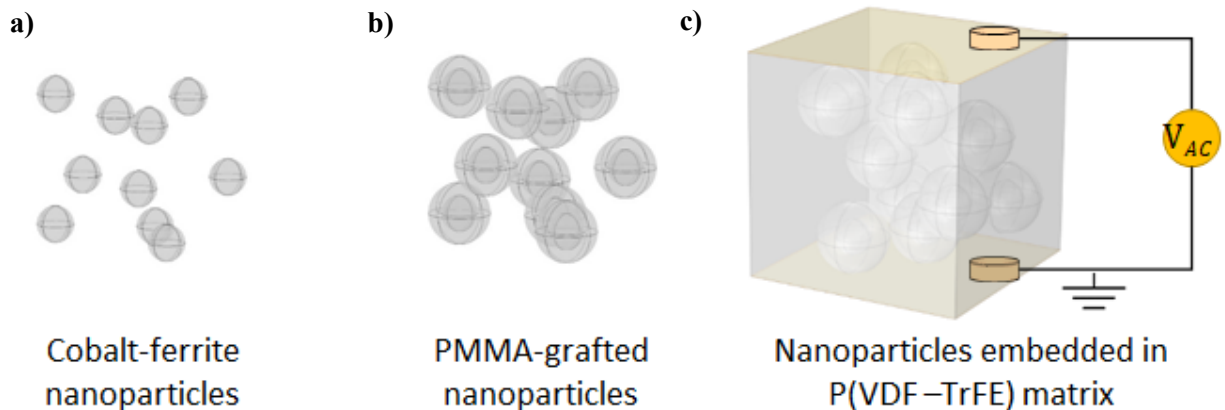
Figure 8.1. *An example of defining PMC geometry for finite-element method simulation. a) bare nanoparticles, b) PMMA-grafted nanoparticles, and c) the same nanoparticles in b) that are embedded in a P(VDF-TrFE) matrix, which is contacted with top and bottom Au electrodes. The voltmeter reads V_{AC} that is generated upon application of H_{AC}.*

8.2.2. Uniformly dispersed versus agglomerated nanoparticles in the polymer matrix

For a fair comparison, a fixed number of particles is used in both scenarios so that both uniform dispersion and agglomeration systems have a similar interfacial area between the nanoparticles and the piezoelectric matrix. For every case, at least 10 different randomly generated microstructures are calculated to reach reliable statistics. **Figure 8.3** shows a few examples for both uniform and agglomerated cases. From the magnetically induced voltage, the values for α_{ME} for every structure is calculated. For the sake of comparison, we have normalized all the calculated α_{ME} by dividing them by the largest α_{ME}, which is obtained for the case with uniform nanoparticle dispersion. The normalized α_{ME} for every case are then averaged and presented in **Figure 8.4**. It should also be noted that in the simulation, the whole volume of the matrix is considered piezoelectric, even the volume enclosed by the agglomerated particles. This limitation of the software becomes advantageous in better understanding of the experimental results. Our code defines the nanoparticles such that they do not merge upon agglomeration. The interface

between the nanoparticle and the piezoelectric phase for uniform dispersion and agglomeration cases remains practically the same.
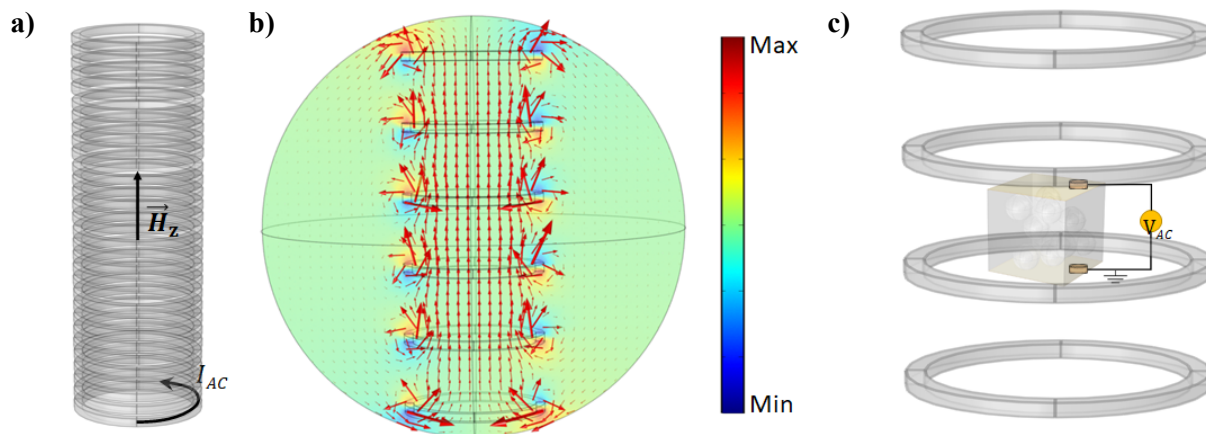
Figure 8.2. Definition of the simulation geometry. a) First, a solenoid is defied, wherein an AC current is passing. b) The geometry is optimized to yield a uniform field at the center of the solenoid. c) The PMC is placed at the center of a solenoid to calculate the magnetoelectric voltage coefficient. (Note that some of the turns for solenoid are removed for clarity of the image). The images are not to the scale as used for the simulations.
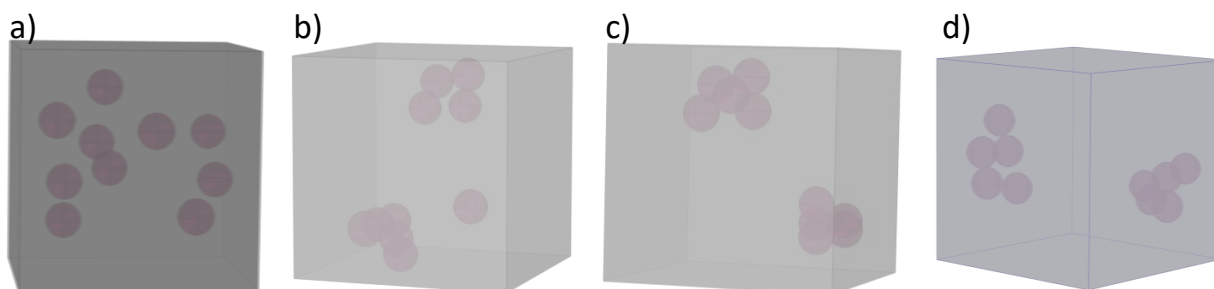
Figure 8.3. Typical examples of simulated composites with different nanoparticle dispersion. a) typical case of a uniform dispersion scenario, and b-d) examples of agglomeration of the nanoparticles. For agglomeration, the nanoparticles are set to be in close contact but not merging. The rest of the cube, including the volume enclosed between the agglomerated nanoparticles, is piezoelectric.

To substantiate the operational mechanism of the PMCs, and the adverse effect of agglomeration, finite-element method simulations have been performed for both scenarios of uniform and agglomerated dispersions of magnetic nanoparticles (cobalt-ferrite in this case) in a piezoelectric polymer matrix made of P(VDF-TrFE). Cobalt-ferrite, with Co stoichiometry of 0.7, hence $Co_{0.7}Fe_{2.3}O_4$, is chosen for its relatively large magnetostriction coefficient, which approaches 590×106 ppm along the [100] direction. [50,53] The choice of P(VDF-TrFE) as the matrix is motivated by its sizeable piezoelectric voltage coefficient of -0.372 V m N^{-1}. We note that the code is generic and can be adapted to different materials systems. Details of the simulation are given in the Supplementary Materials. A PMC thin-film, schematically shown in **Figure 8.1a**, is subjected to a time-varying magnetic field, H_{AC}, along the z-axis. The induced strain in the nanoparticles as a function of H_{AC}, the volumetric stress exerted on the piezoelectric phase, and the voltage difference developed across the capacitor plates are calculated. The graphics in **Figure 8.4a-b** present a snapshot of the calculations when H_{AC} is maximum for uniform dispersion of the nanoparticles.

As H_{AC} varies, the nanoparticles are strained and stress the nearby piezoelectric phase. The strained nanoparticles, **Figure 8.4a**, stress the nearby piezoelectric phase. The resulting volumetric stress in the P(VDF-TrFE) phase generates a piezo-voltage, **Figure 8.4c**, that varies in time and is out-of-phase with the applied H_{AC} because P(VDF-TrFE) has a negative piezoelectric voltage coefficient.

Following the establishment of the operational mechanism, α_{ME} for the composites with uniform and agglomerated nanoparticle dispersion are calculated. Typical examples of the structures used for the simulations of the PMCs with uniform dispersion and aggregated nanoparticles are given in **Figure 8.3**. The summary of the calculations, presented in **Figure 8.4d**, unambiguously show that the PMC with uniform nanoparticle dispersion have a larger α_{ME} with a narrow standard deviation from its mean value, whereas the composite with agglomerated particles have a significantly smaller α_{ME} with a broader standard deviation from the mean value. The reduction in α_{ME} is solely due to the agglomeration because the stress is transferred to the nearby nanoparticles instead of the piezoelectric phase. Hence, magnetostrictive strain is effectively damped, and the interfacial interaction between the magnetic and piezoelectric phases is reduced, yielding a reduced piezo voltage and therefore substantially reduced α_{ME} values.
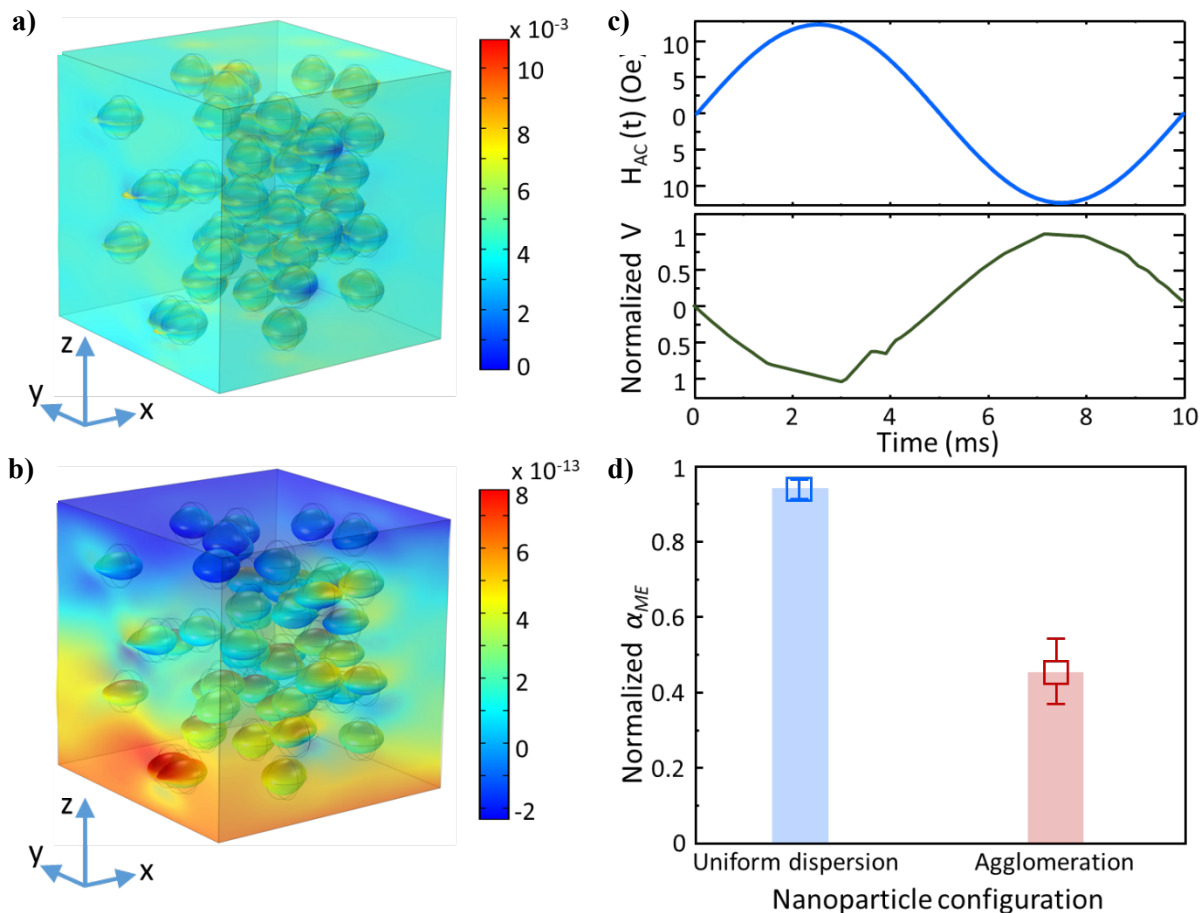
Figure 8.4. *Origin of the reduced coupling coefficient in PMCs. a) and b) simulation of the PMC with uniform nanoparticle dispersion under an AC magnetic field, H_{AC}, that varies along the z-axis. For the sake of clarity, the strain in the nanoparticles has been graphically magnified to show the effect of magnetostriction. The volumetric stress in the piezoelectric phase by the strained nanoparticles is shown in a), and the resulting voltage in the piezoelectric phase is shown in b). c) The calculated magnetically induced voltage is out of*

phase with the H_{AC} because of the negative d_{33} coefficient of P(VDF-TrFE). d) Comparison between the voltages generated by PMCs with fine uniform dispersion and agglomerated nanoparticles. For every scenario, the statical average is obtained for at least 10 simulations with different nanoparticle distributions.

8.3. Experimental

Cobalt-ferrite nanoparticles were synthesized by the thermal decomposition method.[47, 53, 67] As synthesized, nanoparticles are covered with oleate.[53] To initiate the surface of the nanoparticles, we exchange oleate, which covers the surface of the as-synthesized nanoparticles, with CTCS.[57, 59] Subsequently, MMA brushes were grown using surface-initiated atom transfer radical polymerization (SI-ATRP). The molecular weight of the PMMA shell amounts to M_n= 41000 g mol^{-1}. The polydispersity index, PDI, of the grafted-PMMA is below 1.2, indicating that the polymerization proceeded in a controlled living fashion.

Composite thin films were prepared by dissolving various amounts of the PMMA-modified nanoparticles with P(VDF-TrFE) in a common organic solvent (cyclopentanone) and at a substrate temperature of 50 °C. Thin-films were realized by spin-coating or bar coating under low humidity conditions (below 10%) to suppress vapor-induced phase separation (VIPS)[62, 70] and obtain compact thin-films. Film thickness and roughness were measured using a Dektak profilometer. To prepare capacitors, glass slides were first thoroughly cleaned in acetone, propanol, and DI-water. As bottom electrode, 50 nm Au/1 nm Cr electrodes were evaporated. Films of P(VDF-TrFE) or its composites were formed by spin coating under low humidity of <10 % to suppress VIPS. The magnetic properties of the nanoparticles and PMMA-modified ones were measured using a VSM (Cryogenic Ltd) magnetometer. The magnetization, *M-H*, loops were measured under a maximum applied field of 50 kOe at 300 K. The ferroelectric properties were measured using the Sawyer-Tower circuit. The magnetically induced voltage coefficient was determined using a lock-in technique, as described in chapter 7.[71]

8.4. Design considerations for PMC thin-films with large α_{ME} values

After having established the importance of a uniform dispersion of the magnetic nanoparticles and their interfacial interaction, we embark on the experimental realization of the PMC thin-films with large α_{ME}, in the absence of an external DC magnetic field, i.e., a self-biased multiferroic composite. We put forth the following composite design considerations; First, highly magnetostrictive nanoparticles and polymers with large piezoelectric voltage coefficient should be used. Second, the magnetic properties of the nanoparticles should be adjusted to obtain room-temperature remanent magnetization in the nanoparticles to enable the realization of a self-biased multiferroic. Third, the interfacial area between the magnetic nanoparticle and the piezoelectric polymer phases should be maximized, which means that the size of the nanoparticles should be reduced to the nano-size regime, while at the same time they still show room-temperature remanent magnetization. Lastly, but most importantly, the nanoparticle should be compatible (or be compatibilized) with the polymer matrix to ensure uniform dispersion and maximizing the interfacial magnetoelectric coupling interactions.

8.4.1. Downsizing and compatibilization of cobalt-ferrite nanoparticles

Thermal decomposition is used to synthesize cobalt-ferrite, $Co_xFe_{3-x}O_4$, nanoparticles, and the size and stoichiometry of the nanoparticles are finely tuned. The $Co_xFe_{3-x}O_4$ nanoparticles are chosen due to their relatively large magnetostriction coefficient [50] and their large magneto-crystalline anisotropy [46-50], which enables nanosizing of the particles while maintaining room-temperature remanent magnetization.[49-53]

However, a complex interplay exists between Co stoichiometry, x, magnetic properties, and particle size, which should be investigated to find the optimized stoichiometry range.
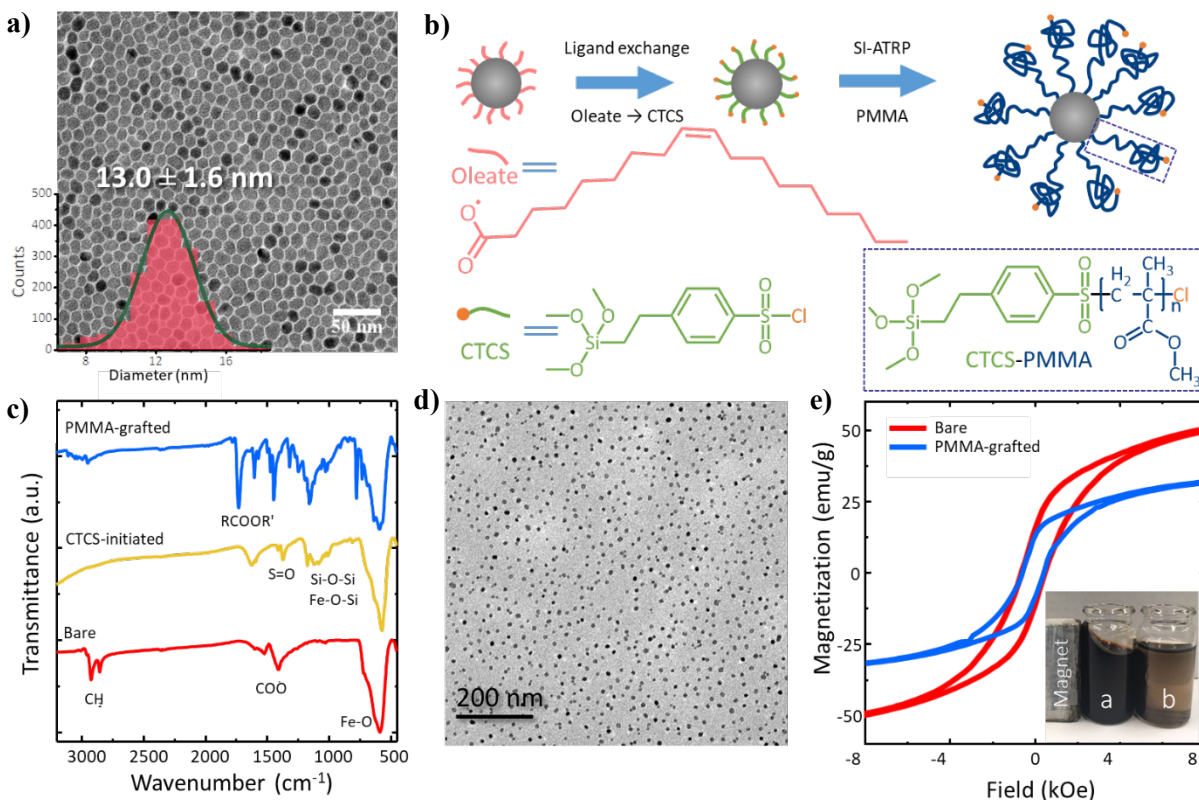
Figure 8.5. *Compatibilization of cobalt-ferrite nanoparticles. (A) TEM image of bare (oleate-coated) cobalt-ferrite nanoparticles. The inset is the size distribution histogram obtained for more than 2000 nanoparticles. (B) Schematic representation of SI-ATRP synthesis of PMMA on the nanoparticles. (C) FTIR spectra of oleate-, CTCS-, and PMMA-coated cobalt-ferrite nanoparticles. (D) TEM image of the PMMA-coated cobalt ferrite nanoparticle with PMMA molecular weight of Mn = 41 kg/mol. (E) Room temperature magnetization as a function of applied magnetic field for bare and PMMA-grafted cobalt ferrite nanoparticles with an average diameter of 13± 1.6 nm and Co stoichiometry, x ~ 0.7. The inset shows the colloidal stability of bare (a) and PMMA-grafted (b) nanoparticles in organic solution (toluene) in the presence of the magnetic field.*

A typical TEM image of the as-synthesized nanoparticles and their size distribution is given in **Figure 8.5a**. Through an extensive synthesis attempt combined with the characterization of the magnetic properties of the nanoparticles, details we have published previously [53], it is found that the optimum cobalt stoichiometry, x, is 0.7, which enables reducing the size for the nanoparticle with stable room-temperature magnetization to just 13 ± 1.6 nm (in diameter).[53] The nanoparticles presented in **Figure 8.5a**, therefore, show a stable room-remanent magnetization, M_r, that amounts to 25 emu g^{-1} as presented in **Figure 8.5e**.

The next step is the compatibilization of the $Co_{0.7}Fe_{2.3}O_4$ nanoparticles with the piezoelectric polymer matrix, P(VDF-TrFE). Compatibilization is realized by grafting polymethylmethacrylate (PMMA) on the surface of the nanomagnets. Surface-initiated atom transfer radical polymerization (SI-ATRP) is chosen to

grow the PMMA chains from the nanoparticles' surface, as shown in **Figure 8.5 b**, because SI-ATRP enables precise control over the thickness of the PMMA shell. [54-58]

Fourier Transform Infrared Spectroscopy (FTIR), **Figure 8.5 c**, shows the presence of CH and COO bands, indicating that the as-synthesized nanoparticles are capped with oleate surfactant. Therefore, the first step in our SI-ATRP is to replace the oleate with the surface initiator 2-(4-chlorosulfonylphenyl) ethyltrichlorosilane (CTCS). Details of the ligand exchange procedure are described in the Materials and Method section. The FTIR spectra of the nanoparticles after the ligand exchange process, **Figure 8.5c**, demonstrate the successful replacement of CTCS. Subsequently, PMMA growth is initiated via ultrasound-mediated ATRP. The FTIR spectra of PMMA-grafted nanoparticles, **Figure 8.5c**, show the characteristic peak of the ester group of PMMA at 1730 cm^{-1} confirming successful growth of PMMA on the surface.[57, 59] ATRP provides a high level of control over the kinetics of the reaction; hence the thickness or molecular weight of the PPMA shell could be precisely controlled with a polydispersity (PDI) that varies between 1.1 to 1.25. A TEM image of the grafted nanoparticles with a PMMA molecular weight of Mn = 41 kg mol^{-1} is shown in **Figure 8.5d**. Magnetically induced agglomeration is entirely prevented, and the nanoparticles are separated by the PMMA shell, with a center-to-center distance of 35 ± 6 nm as determined from the TEM image. Experimentally, the M-H curve of the PMMA-grafted nanoparticles, **Figure 8.5c**, shows a reduction of M_s (obtained at 20 kOe) from 64.5 emu gr^{-1} for the bare to 42.3 emu gr^{-1} of the PMMA-grafted nanoparticles. Reduction of remanent magnetization is because of the PMMA shell, which constitutes nearly 37% of the total weight of the grafted nanoparticles. Therefore, the M_s of the bare nanoparticles should be reduced by the same factor to 40.6 emu gr^{-1}, which is very close to the experimentally measured value. [60, 61] The growth of the PMMA shell very efficiently hinders particle agglomeration in solution and leads to a high degree of colloidal stability of the nanoparticles in organic solvents such as toluene and cyclopentanone, even in the presence of a strong magnetic field, as shown in the inset of **Figure 8.5e**.

8.4.2. Thin-film fabrication and characterization

The PMMA-grafted nanoparticles are dispersed in P(VDF-TrFE) in the solution phase, and thin-film PMCs are fabricated. We note that thin-films with as-synthesized oleate-coated nanoparticles are also fabricated as the benchmark composite. To evaluate the miscibility or compatibility of the nanoparticles with P(VDF-TrFE), differential scanning calorimetry (DSC) of both composite films are performed, and the first heating and cooling thermograms, **Figure 8.6** are analyzed.
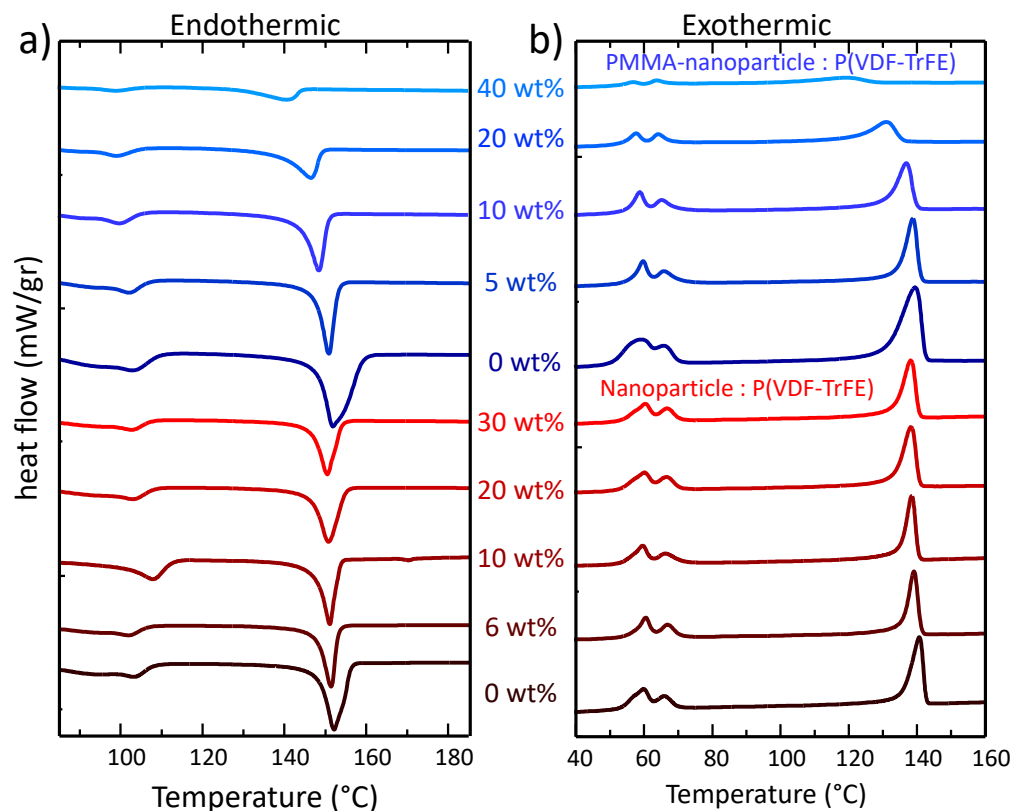
Figure 8.6. *DSC thermogram for P(VDF-TrFE) nanocomposites. a) The first heating and b) cooling curves for the composites with different wt% of as-synthesized nanoparticles (red) and PMMA-grafted nanoparticles (blue).*

We noted that cobalt ferrite magnetic nanoparticles do not show any phase change or a magnetic phase transition for the investigated temperature range.[72] Therefore, the DSC curves only account for the phase transition in P(VDF-TrFE). For the benchmark composites with the as-synthesized oleate-coated nanoparticles, **Figure 8.7a**, the melting temperature (T_m) and crystallization (T_c) temperatures do not show significant variation with the composition and remain constant, which indicates the immiscibility of the oleate-coated nanoparticles with the P(VDF-TrFE) matrix.

In sharp contrast, the nanocomposites with PMMA-grafted nanoparticles show a monotonic depression in both T_m and T_c of P(VDF-TrFE) with increasing the particle loading, indicating miscibility of the PMMA-grafted nanoparticles with the P(VDF-TrFE) matrix over the investigated composition range.[41] The miscibility arises from the dipole/dipole interaction between the −CF2 groups of VDF and the −C=O groups of PMMA and the hydrogen bonding between the double-bonded oxygen of the carbonyl and the acidic hydrogen of the −CH2−CF2− group.[62] The normalized crystallinities of various nanocomposites are presented in **Figure 8.7b**. The crystallinities are obtained from DSC thermograms and are corrected for the weight fraction of the P(VDF-TrFE) phase and then normalized to the crystallinity of the pristine P(VDF-TrFE) film, which is 35%. Due to their miscibility, the crystallinity of the nanocomposite with PMMA-grafted nanoparticles reduces much faster than that of the benchmark composite as the concentration increases.
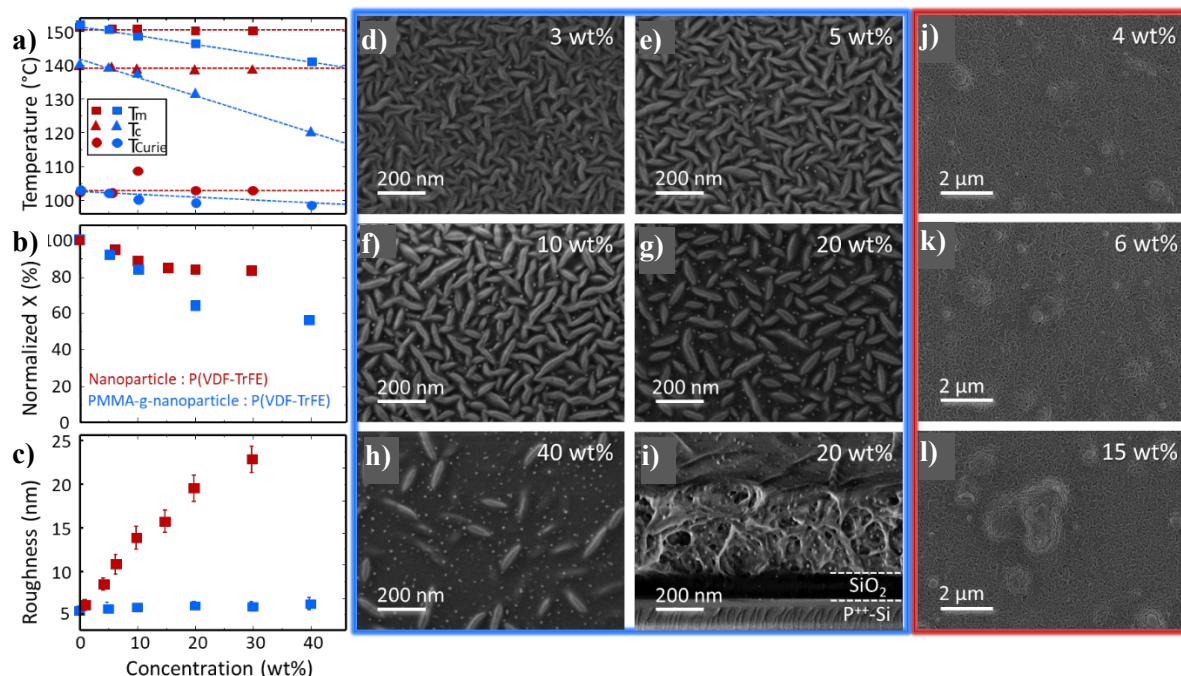
Figure 8.7. *Microstructure of the polymer multiferroic thin-films. a) Evolution of the melting (T_m), crystallization (T_c), and Curie (T_{Curie}) temperatures of the nanocomposite. b) Normalized crystallinity of P(VDF-TrFE) phase as a function of nanoparticle concentration for as-synthesized (red) and PMMA-grafted (blue) nanoparticles. The dashed lines in panel A are guides to the eye. c) Changes in the roughness of the nanocomposite thin-films as a function of particle loading. d-h) SEM topographical images for the nanocomposites of P(VDF-TrFE) with various loading of PMMA-grafted nanoparticles. i) Cross-sectional image of a 400 nm thick P(VDF-TrFE) nanocomposite thin-film with 20 wt% loading of PMMA-grafted nanoparticle. j-l) Nanocomposites of P(VDF-TrFE) with as-synthesized nanoparticles.*

Based on the DSC results, phase separation and, consequently, agglomeration is expected for the benchmark nanocomposite, whereas a uniform dispersion of PMMA-grafted nanoparticles in P(VDF-TrFE) is anticipated. The scanning electron microscope (SEM) image for P(VDF-TrFE) nanocomposite thin-films with various loading of PMMA-grafted nanoparticles are presented in **Figure 8.7d-h**. The needle-like grains are well-known P(VDF-TrFE) crystallites, and the white dots are the PMMA-grafted nanoparticles. The crystallites are, therefore, pure P(VDF-TrFE), and the PMMA-grafted nanoparticles are accommodated in the amorphous phase of the matrix at the expense of a reduction in the size and number of the P(VDF-TrFE) crystallites, which is consistent with the crystallinities that are obtained from DSC thermograms. The SEM analysis undoubtedly confirms that the PMMA-grafted nanoparticles are uniformly distributed in the P(VDF-TrFE) matrix. The uniform dispersion is obtained for all compositions, even for loadings as high as 40 wt%, as shown in **Figure 8.7g**. A cross-sectional SEM image of the sample with 20 wt% PMMA-grafted nanoparticles, **Figure 8.7i**, shows the absence of nanoparticle agglomeration in the volume of the nanocomposite thin-film that is just 400 nm thick and confirms the effectiveness of the PMMA shell in preventing phase separation.

In sharp contrast, the composites with as-synthesized nanoparticles show severe particle agglomeration, **Figure 8.7j-l**, even at loading as low as 4 wt%. All benchmark composite films suffer from agglomeration, which hampers the fabrication of smooth thin films needed to evaluate the magnetoelectric coupling. The composite thin-films fabricated from as-synthesized nanoparticles are rough, and the roughness increases with the particle loading, as shown in **Figure 8.7c**. In contrast, the

thin-films fabricated with PMMA-grafted nanoparticles show an RMS roughness well below 10 nm and are very smooth due to the absence of agglomeration.

8.5. Multiferroic properties

Having solved the agglomeration issue and achieved smooth thin-films with a uniform dispersion of the nanoparticles in the P(VDF-TrFE) matrix, we have fabricated PMC thin-film capacitors to evaluate the ferroelectric and ferromagnetic properties. First, pristine P(VDF-TrFE) thin-film capacitors are evaluated. The coercive field, EC, and remanent polarization, P_r, of the pristine P(VDF-TrFE) film, Figure **8.8a**, amounts to 50 MV m^{-1} and 6.1 µC m^{-2}, respectively. Subsequently, the benchmark nanocomposite thin-film capacitors with as-synthesized nanoparticles are measured. A representative *D-E* loop for the composite with just 10 wt% loading of as-synthesized nanoparticles is presented in **Figure 8.8a**. Despite being less crystalline than the pristine P(VDF-TrFE), the composite shows a seemingly increased P_r and E_C, which, however, are unreliable due to the increased leakage current through the device, as explained by Scott in his famous ferroelectric banana paper.[63, 64] The increased leakage current is ascribed to particle agglomeration. as a result of nanoparticle agglomeration.[63] It should be noted that the presence of the leakage current also impedes reliable evaluation of the magnetoelectric coupling and leads to an overestimation of the α_{ME} value.[20] We note that distortion of the D-E loop for the PMCs thin-films with as-synthesized nanoparticles begins at much lower compositions at the loading of 4 wt%. The leakage current problem is much severe at higher loading of as-synthesized nanoparticles, as shown in **Figure 8.8 a**.
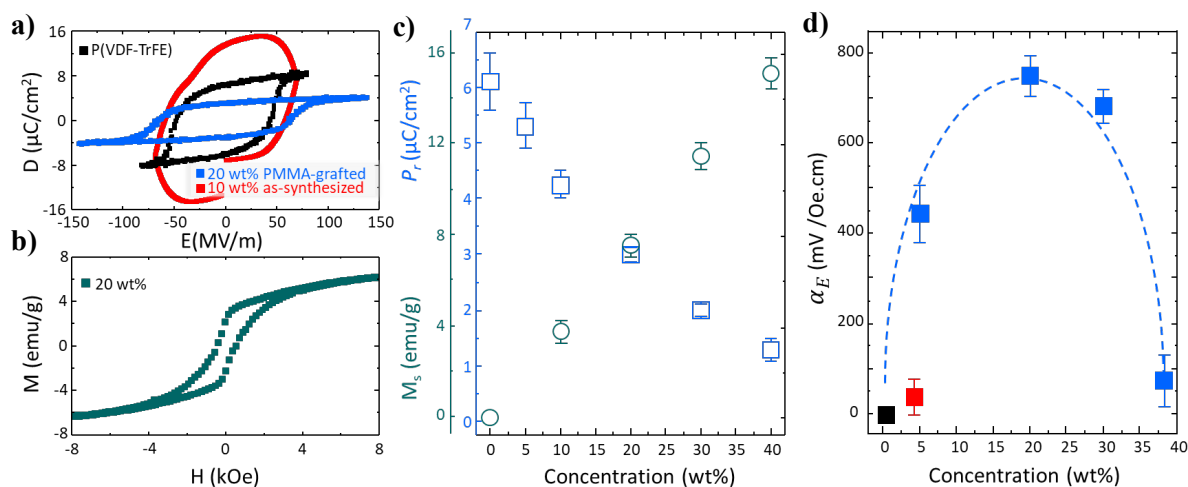
Figure 8.8. *Solution-processed nanocomposite multiferroic thin films. a) Representative ferroelectric displacement loop for a pristine P(VDF-TrFE) capacitor (black), and for P(VDF-TrFE) nanocomposites with 10 wt% as-synthesized (red) and 20 wt% PMMA-grafted nanoparticle (blue). b) Magnetization curve for the nanocomposite of P(VDF-TrFE) with 20 wt% PMMA-grafted nanoparticles. c) Evolution of remanent polarization, P_r, and saturation magnetization, M_s, of the composites as a function of the weight of PMMA-grafted nanoparticle. d) Room-temperature magnetoelectric voltage coefficient of the nanocomposites with various loading of PMMA-grafted (blue) and as-synthesized cobalt-ferrite nanoparticles (red). The coupling coefficients are obtained under similar H_{AC} and frequencies of 1 Oe and 10 kHz, respectively. The dashed blue line is given as a guide.*

Proper ferroelectric hysteresis loops have been obtained for P(VDF-TrFE) nanocomposites with PMMA-grafted nanoparticles. A representative D-E displacement loop for the composite with 20 wt% PMMA-grafted nanoparticles is given in **Figure 8.8a**, which shows a reduced P_r (3.1 µC m^{-2}) and an increased E_C

(65 MV m^{-1}). Since P$_r$ stems from the crystalline phase of the polymer, a theoretical upper limit of 3.8 μC m^{-2} is expected because the crystallinity of the P(VDF-TrFE) phase is reduced by 65% of its pristine state, shown in **Figure 8.7b**. Obtaining an experimental value similar to the expected theoretical value confirms the internal consistency of the measurements. We note that similar high-quality D-E loops, albeit with reduced P$_r$, have been obtained for all nanocomposite thin-films with loading even as high as 40 wt%, as presented in **Figure 8.9b**. The reduction trend in P$_r$ as a function of PMMA-grafted nanoparticle weight fraction is presented in **Figure 8.8c**. Remanent polarization drops linearly with the weight fraction within the investigated composition range.
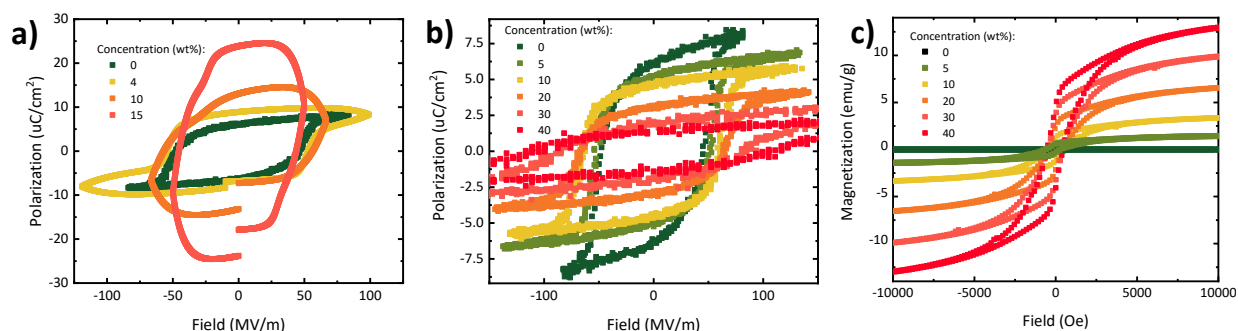
Figure 8.9. *Polarization and magnetization characterization of the nanocomposite thin films. Polarization, P-E, response of the nanocomposite thin films of P(VDF-TrFE) with a) as-synthesized nanoparticles and b) PMMA-grafted nanoparticles with various loadings. c) Magnetization, M-H, response of the nanocomposite thin films using PMMA-coated nanoparticles at different loadings.*

Next, the magnetic properties of the nanocomposites are evaluated. A representative magnetization loop for the nanocomposite with 20 wt% PMMA-grafted nanoparticles, presented in **Figure 8.8b**, demonstrates that the composite thin-film exhibits remanent magnetization at room temperature. All nanocomposites exhibit room-temperature saturation magnetization **Figure 8.8c**, with M$_s$ that increases linearly as the weight fraction of PMMA-grafted nanoparticles increases, as presented in **Figure 8.4c**. Therefore, P(VDF-TrFE) nanocomposites thin-films with PMMA-grafted nanoparticles are simultaneously ferroelectric and ferromagnetic, hence a room-temperature multiferroic nanocomposite thin-films.

Finally, the α_{ME} values for the composite are evaluated. The nanocomposites generate a voltage when are placed in an external variable magnetic field, H$_{AC}$. As indicated earlier, the magnetically induced voltage, V$_{ME}$, on the capacitor electrodes is V$_{ME}$ =$\alpha_{ME} \cdot$H$_{AC} \cdot$t, where t is the thickness of the nanocomposite layer. The H$_{AC}$ is the amplitude of the externally applied magnetic field, which varied from 1 to 9 Oe. A well-established lock-in technique is used to measure magnetically induced voltage, V, on the capacitor plates. Details about the measurement technique can be found in the previous chapter dedicated to magnetoelectric measurement and its technical consideration to avoid overestimation of α_{ME} .[74] The benchmark nanocomposites with as-synthesized nanoparticles are measured first. For this series, only α_{ME} value for the composite with 4 wt% as-synthesized nanoparticles could be evaluated and amounted 30 ± 10 mV Oe^{-1} cm^{-1}, which is comparable to the values reported in the literature. [42, 65, 66] Measurement of the α_{ME} for composites with loadings beyond 4 wt% is hampered by the leakage current through the layers. On the contrary, the nanocomposites with PMMA-grafted nanoparticles for nearly the same loading (5 wt%) exhibit a significant increase in α_{ME}, which reaches values as high as 450 ± 50 mV Oe^{-1} cm^{-1}, as presented in **Figure 8.8d**. With increasing the weight fraction of the PMMA-grafted nanoparticles to 20 wt%, the room-temperature α_{ME} value of the nanocomposite reaches 750 ± 30 mV Oe^{-1} cm^{-1}, which is a remarkably high value reported for PMC thin-films thus far. Upon further increase in the loading of the

nanoparticles, the α_{ME} values are reduced. Therefore, the experimentally determined optimal composition that yields the largest α_{ME} is 20 wt%, for the cobalt ferrite nanoparticles, $Co_{0.7}Fe_{2.3}O_4$, with the size of 13 nm and a PMMA shell with a molecular weight of 41 kg mol^{-1}. We note that values in **Figure 8.8d** have been obtained in the absence of an external DC magnetic field, H_{DC}, which confirms that the nanocomposite is self-biased. Furthermore, similar α_{ME} value in the presence of H_{DC} have been measured, as presented in **Figure 8.10**, indicating the power and effectiveness of the proposed design strategy to obtain self-biased strong coupling coefficients.
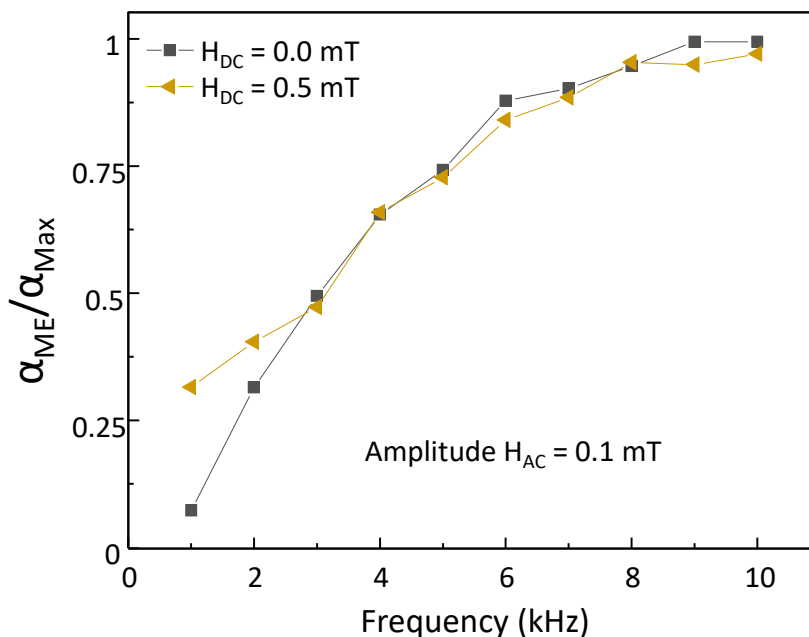
Figure 8.10. *Frequency and H_{DC} dependence of the α_{ME}. Values are obtained for the nanocomposite with 20 wt% PMMA-grafted nanoparticles. The α_{ME} values are normalized to the maximum value obtained for the case with at $H_{DC}= 0$ mT. The symbols show that within the experimental uncertainties, similar coupling coefficients and the same frequency dependence are obtained in the presence and absence of an external DC magnetic field.*

8.6. Conclusion

In summary, thin-films of polymer-based nanocomposites with remarkably large magnetoelectric coupling coefficients have been demonstrated by preventing agglomeration of the magnetic nanoparticle. By maximizing the interface between the nanoparticles and the piezoelectric matrix through nanoparticle size reduction, it is finally possible to experimentally demonstrate solution-processed thin-film nanocomposites that show a coupling coefficient of 750 ± 30 mV Oe^{-1} cm^{-1}. Since the nanoparticles are magnetic at room temperature, their resulting composite shows magnetoelectric coupling even in the absence of an external DC magnetic field. The breakthrough in uniform nanoparticle dispersion in thin-films is achieved by mitigating the agglomeration through surface-initiated polymerization of polymethylmethacrylate (PMMA) chains grafted on the surface of the cobalt-ferrite nanoparticles, which renders the nanoparticles miscible in a P(VDF-TrFE) matrix. An important note is that the large value reported here is by no means the upper limit because there are experimentally many parameters that can be explored, such as the use of highly magnetostrictive nanoparticles, to enhance the coupling response of the system even further. Demonstrating solution-processed multiferroic thin films with sub-micrometer thicknesses and a giant magnetoelectric coupling coefficient opens the gate to an unexplored

field of (flexible) multiferroic electronic devices. The methodology employed here is generic and can be adapted to various polymer nanocomposite systems, where the Holy Grail is to achieve a uniform filler dispersion in a polymer matrix.

Reference

1) D. Khomskii, *Physics* 2009, **2**, 20-27.
2) R. Ramesh, N. A. Spaldin, *Nat. Mater.* 2007, **6**, 21-29.
3) H. Schmid, *Ferroelectrics* 1994, **162**, 317-338.
4) S. -W. Cheong, M. Mostovoy, *Nat. Mater.* 2007, **6**, 13-20.
5) M. Fiebig, Revival of the magnetoelectric effect. *J. Phys. D: Appl. Phys.* 2005, **38**, R123.
6) Y. Cheng, B. Peng, Z. Hu, Z. Zhou, M. Liu, *Phys. Lett. A* 2018, **382**, 3018-3025.
7) T. Sadat, D. Faurie, P. Godard, D. Thiaudière, P. Renault, F. Zighem, *J. Phys. D: Appl. Phys.* 2020, *53*, 145001.
8) N. A. Spaldin, R. Ramesh, *Nat. Mater.* 2019, **18**, 203.
9) S. Manipatruni, D. E. Nikonov, I. A. Young, *Nat. Phys.* 2018, **14**, 338-343.
10) S. Khizroev, S. Technobiology's *Cold Spring Harb. Perspect.* 2019, **9**, a034207.
11) J. Wang, J. B. Neaton, H. Zheng, V. Nagarajan, S. B. Ogale, B. Liu, D. Viehland, V. Vaithyanathan, D. G. Schlom, U. V. Waghmare, N. A. Spaldin, K. M. Rabe, M. Wuttig, R. Ramesh, *Science* 2003, **299**, 1719-1722.
12) T. Kimura, T. Goto, H. Shintani, K. Ishizaka, T. -H., Arima, Y. Tokura, *Nature* 2003, **426**, 55-58.
13) N. Hur, S. Park, P. Sharma, J. Ahn, S. Guha, S. -W. Cheong, *Nature* 2004, **429**, 392-395.
14) P. L. A. Martins. S. Lanceros-Méndez, *Appl. Mater. Today* 2019, **15**, 4.
15) N. Cai, C. -W. Nan, J. Zhai, Y. Lin, *Appl. Phys. Lett.* 2004, **84**, 3516-3518.
16) M. K. Lee, T. K. Nath, C. -B. Eom, M. C. Smoak, F. Tsui, *Appl. Phys. Lett.* 2000, **77**, 3547-3549.
17) C. W. Nan, M. Li, X. Feng, S. Yu, *Appl. Phys. Lett.* 2001, 78, 2527-2529.
18) Z. Chu, M. PourhosseiniAsl, S. Dong, *J. Phys. D: Appl. Phys.* 2018, **51**, 243001.
19) D. Viehland, J. F. Li, Y. Yang, T. Costanzo, A. Yourdkhani, G. Caruntu, *J. Appl. Phys.* 2018, **124**, 061101.
20) J. Scott, J. Gardner, *Mater. Today* 2018, *21*, 553-562.
21) J. X. Zhang, J. Y. Dai, L. C. So, C. L. Sun, C. Y. Lo, S. W. Or, H. L. W. Chan, *J. Appl. Phys.* 2009, **105**, 054102-054106.
22) P. Martins, A. Lasheras, J. Gutiérrez, J. M. Barandiaran, I. Orue, S. Lanceros-Mendez, *J. Phys. D: Appl. Phys.* 2011, **44**, 495303-495307.
23) P. Martins, X. Moya, L. Phillips, S. Kar-Narayan, N. Mathur, S. Lanceros-Mendez S. *J. Phys. D: Appl. Phys.* 2011, **44**, 482001-482004.
24) D. Guyomar, B. Guiffard, R. Belouadah, L. Petit, *J. Appl. Phys.* 2008, **104**, 074902-074907.
25) P. MartinsX. Moya, C. Caparrós, J. Fernandez, N. Mathur, S. Lanceros-Mendez, *J. Nanopart. Res.* 2013, **15**, 1825-1830.
26) P. Martins, R. Gonçalves, S. Lanceros-Mendez, A. Lasheras, J. Gutiérrez, J. Barandiarán, *Appl. Surf. Sci.* 2014, **313**, 215-219.
27) A. Maceiras, P. Martins, R. Gonçalves, G. Botelho, E. V. Ramana, S. Mendiratta, M. San Sebastián, J. L. Vilas, S. Lanceros-Mendez, L. M. León, *Eur. Polym. J.* 2015, **64**, 224-228.
28) P. Martins, A. Larrea, R. Gonçalves, G. Botelho, E. Ramana, S. Mendiratta, V. Sebastian, S. Lanceros-Mendez, *ACS Appl. Mater. Interfaces,* 2015, **7** 11224-11229.
29) T. Fiorido, J. Galineau, V. Salles, L. Seveyrat, F. Belhora, P. -J, Cottinet, L. Hu, Y. Liu, B. Guiffard, A. Bogner-Van De Moortele, T. Epicier, D. Guyomar, A. Brioude, *Sen. and Actuators A: Phys.* 2014, **211**, 105-114.
30) T. H. L. Nguyen, L. Laffont, J. F. Capsal, P. _J. Cottinet, A. Lonjon, E. Dantras, C. Lacabanne, *Mater. Chem. Phys.* 2015, **153**, 195-201.
31) A. Ahlawat, S. Satapathy, M. M. Shirolkar, J. Li, A. A. Khan, P. Deshmukh, H. Wang, R. J. Choudhary, A. K. Karnal, *ACS Appl. Nano. Mater.* 2018, **1**, 3196-3203.
32) C. Behera, R. Choudhary, P. Das, *J. Mater. Sci. Mater. Electron.* 2017, **28**, 2586-2597.
33) C. Behera, R. Choudhary, *J. Alloys Compd.* 2017, **727**, 851-862.

34) N. Adhlakha, K. Yadav, M. Truccato, P. Rajak, A. Battiato, E. Vittone, *Eur. Polym. J.* 2017, **91**, 100-110.

35) A. Mayeen, M. Kala, M. Jayalakshmy, S. Thomas, D. Rouxel, J. Philip, R. N. Bhowmik, N. Kalarikkal, *Dalton Trans.* 2018, **47**, 2039-2051.

36) W. Jing, f. Fang, *Compos. Sci. Technol.* 2017, **153**, 145-150.

37) R. Brito-Pereira, C. Ribeiro, S. Lanceros-Mendez, P. Martins, *Compos. B Eng.* 2017, **120**, 97-102

38) A. Omelyanchik, V. Antipova, C. Gritsenko, V. Kolesnikova, D. Murzin, Y. Han, A. V. Turutin, I. V. Kubasov, A. M. Kislyuk, T. S. Ilina, D. A. Kiselev, M. I. Voronova, M. D. Malinkovich, Y. N. Parkhomenko, M. Silibin, E. N. Kozlova, D. Peddis, K. Levada, L. Makarova, A. Amirov, V. Rodionova, Nanomaterials 2021, **11**, 1154.

39) R. Polícia, A. C. Lima, N. Pereira, E. Calle, M. Vázquez, S. Lanceros-Mendez, P. Martins, *Adv. Electron. Mater.* 2019, **5**, 1900280.

40) S. Chakraborty, S. K. Mandal, B. Saha, *Ceram. Int.* 2019, **45**, 14851–14858.

41) A. Mayeen, M. S. Kale, M. S. Jayalakshmy, S. Thomas, J. Philip, D. Rouxel, R. N. Bhowmik, N. Kalarikkal, *Dalton Trans.* 2019, **48**, 16961-16973.

42) P. Martins, S. Lanceros-Méndez, *Adv. Funct. Mater.* 2013, **23**, 3371-3385.

43) T. Prabhakaran, J. Hemalatha, *AIP Conference Proceedings*: American Institute of Physics 2012,1309-1310.

44) J. Jin, S. G. Lu, C. Chanthad, Q. Zhang, M. A. Haque, Q. Wang *Adv. Mater.* 2011, **23**, 3853-3858.

45) E. Pardo, C. Train, H. Liu, L. M. Chamoreau, B. Dkhil, K. Boubekeur, F. Lloret, K. Nakatani, H. Tokoro, S. Ohkoshi, M. Verdaguer, *Angew. Chem, Int. Ed* 2012, **51**, 8356-8360.

46) A. Demortiere, P. Panissod, B. P. Pichon, G. Pourroy, D. Guillon, B. Donnio, S. Bégin-Colin, *Nanoscale* 2011, **3**, 225-232.

47) H. Sharifi Dehsari, M. Heidari, A. H. Ribeiro, W. Tremel, G. Jakob, D. Donadio, R. Potestio, K . Asadi*, Chem. Mater.* 2017, **29**, 9648-9656.

48) W. Baaziz, B. P. Pichon, S. Fleutot, Y. Liu, C. Lefevre, J. M. Greneche, M. Toumi, T. Mhiri, S. Begin-Colin*, J. Phys. Chem. C* 2014, **118**, 3795-3810.

49) A. G. Kolhatkar, A. C. Jamison, D. Litvinov, R. C. Willson, T. R. Lee, *Int. J. Mol. Sci.* 2013, **14**, 15977-16009.

50) R. Bozorth, E. F. Tilden, A. J. Williams, *Phys. Rev.* 1955, **99**, 1788.

51) A. López-Ortega, E. Lottini, C. D. J. Fernandez, C. Sangregorio, *Chem. Mater.* 2015, **27**, 4048-4056.

52) A. Sathya, P. Guardia, R. Brescia, N. Silvestri, G. Pugliese, S. Nitti, L. Manna, T. Pellegrino, *Chem. Mater.* 2016 , **28**, 1769-1780.

53) H. Sharifi Dehsari, K. Asadi, *J. Phys. Chem. C* 2018, **122**, 29106-29121.

54) R. Barbey, L. Lavanant, D. Paripovic, N. Schüwer, C. Sugnaux, S. Tugulu, H. A. Klok *Chem. Rev.* 2009, **109**, 5437.

55) K. Matyjaszewski, J. Xia, *Chem. Rev.* 2001, **101**, 2921-2990.

56) K. Ohno, T. Morinaga, K. Koh, Y. Tsujii, T. Fukuda, *Macromolecules* 2005, **38**, 2137-2142.

57) F. Galeotti, F. Bertini, G. Scavia, A. Bolognesi, *J. Colloid Interface Sci.* 2011, **360**, 540-547.

58) T. E. Patten, K. Matyjaszewski, *Adv. Mater.* 1998, **10**, 901-915.

59) E. Marutani, S. Yamamoto, T. Ninjbadgar, Y. Tsujii, T. Fukuda, M. Takano, *Polymer* 2004, **45**, 2231-2235.

60) J. Vargas, W. Nunes, L. Socolovsky, M. Knobel, D. Zanchet, *Phys. Rev. B* 2005, **72**, 184428.

61) S. Fleutot, G. L. Nealon, M. Pauly, B. P. Pichon, C. Leuvrey, M. Drillon, J. L. Gallani, D. Guillon, B. Donnio, S. Begin-Colin*, Nanoscale* 2013, **5**, 1507-1516.

62) M. Li, N. Stingelin, J. J. Michels, M. J. Spijkman, K. Asadi, K. Feldman, P. W. M. Blom, D. M. de Leeuw*, Macromolecules* 2012, **45**, 7477-7485.

63) H. S. Dehsari, M. Kumar, A. Saad, M. Hassanpour Amiri, C. Yan, S. Anwar, G. Glasser, K. Asadi*, ACS Appl. Nano. Mater.* 2018, **1**, 6247-6257.

64) J. Scott, Ferroelectrics go bananas. *J. Phys. Condens. Matter* 2007, **20**, 021001.

65) P. Martins, Y. V. Kolen'ko, J. Rivas, S. Lanceros-Mendez, *ACS Appl. Mater. Interfaces* 2015, **7**, 15017-15022.

66) P. Martins, R. Gonçalves, S. Lanceros-Mendez, A. Lasheras, J. Gutiérrez, J. Barandiarán, *Appl. Surf. Sci.* 2014, **313**, 215-219

67) H. S. Dehsari, A. H. Ribeiro, B. Ersöz, W. Tremel, G. Jakob, K. Asadi, *CrystEngComm* 2017, **19**, 6694-6702.

68) H. Fischer, *Chem. Rev.* 2001, **101**, 3581-3610.

69) K. Ohno, T. Akashi, Y. Huang, Y. Tsujii, *Macromolecules* 2010, **43**, 8805-8812.

70) H. S. Dehsari, J. J. Michels, K. Asadi, *J. Mater. Chem. C* 2017, **5**, 10490-10497.

71) T. Okazaki, Y. Furuya, Y. Sado, Y. Hayashi, S. Sato, C. Saito, *Trans Tech. Publ.* 2010, 98-103.

72) A. Franco, F. C. e Silva, *Appl. Phys. Lett.* 2010, **96,** 172505.

73) M. A. Ashraf, W. Peng, Y. Zare, K. Y. Rhee, *Nanoscale Res. Lett.* 2018, **13**, 214.

74) M. M. Vopson, Y. K. Fetisov, G. Caruntu, G. Srinivasan, *Materials* 2017, **10**, 963.

75) K. Ohno, T. Morinaga, K. Koh, Y. Tsujii, T. Fukuda, *Macromolecules* 2005, **38**, 2137-2142.

76) K. Ohno, C. Mori, T. Akashi, S. Yoshida, Y. Tago, Y. Tsujii, Y. Tabata, *Biomacromolecules,* 2013, **14,** 3453-3462.

77) T. E. Patten, K. Matyjaszewski, *Adv. Mater.* 1998, **10**, 901-915.

78) H. S. Dehsari, M. Heidari, A. H. Ribeiro, W. Tremel, G. Jakob, D. Donadio, R. Potestio, K. Asadi *Chem. Mater.* 2017, **29,** 9648-9656.

Chapter 9

Conclusion and Outlook

9.1. Summary

Functional polymers and their composites are playing an important role in todays advanced materials. PVDF and its copolymer with TrFE is the flagship of organic ferroelectric polymers and an appealing candidate for the realization of devices. Applications range from memory elements with the capability of coding information in the form of polarization states to mechanical energy harvesters for direct conversion of mechanical strain into electric energy for low-power electronics. Fabrication of a 3-0 composite of PVDF and ferromagnetic nanoparticles adds another degree of freedom and leads to the co-existence of magnetic, electric and mechanical coupling in the composite. This, in turn opens new horizons for the realization of hybrid memory elements, high efficiency energy harvesters and sensitive magnetic field sensors, to name a few.

In this thesis, we have fabricated and realized a single transistor memory cell consisting of a field-effect transistor with a ferroelectric gate insulator made of P(VDF-TrFE) and a conductive channel of single layer graphene. The device is then modelled and the concept is extended for realization of multi-state memories by patterning the gate of the FeFET. A generic mathematical model is also developed that describes the behaviour of the device with an acceptable accuracy. The obtained model was also used for the optimization and enhancement of the high on-off ratio memory element based on Graphene FeFETs.

Next, we focused on energy-harvesting related applications of polymer-based multiferroic compounds. Regarding the inherently insulating behaviour of this class of materials and importance of considering this fact in the realization of energy harvesters, a circuit model of a piezoelectric energy harvester was discussed and various approaches were investigated to maximise the output power. A measurement system has also been designed to accurately capture the voltage response of the piezoelectric material. It is equipped with a high input-impedance stage to effectively minimise the loading effect of the measurement instruments when interfacing with piezoelectric materials with large internal resistance and capacitance.

The thesis continued with a numerical analysis of the effect of the mechanical structure of piezoelectric energy harvesters on the delivered power, using a finite element method. The effect of introducing porosity with various pore geometry, size and polymer/air ratio is discussed in detail for improving the harvested power. Local electric field, induced mechanical strain and deformation have been taken into account in this 2D and 3D study.

Since accurate and reproducible measurements of magnetoelectric coupling in multiferroic materials requires good understanding of the underlaying physics and potential pitfalls, a chapter is dedicated to the development of a reliable and self-consistent protocol for measuring the magnetoelectric coupling coefficient using a lock-in amplification technique. This leads to a reliable measurement of the primary figure of merit for a typical multiferroic material, reflecting the strength of the bilateral interplay of the two ferroic orders. First, the measurement theory is explained and then the predictions of the proposed method are experimentally validated with high accuracy and consistency.

Using the proposed method, the voltage generation in a polymer-based multiferroic composite and its magnetoelectric response is studied in detail. The fabricated device is consisting of magnetostrictive nanoparticles dispersed in a P(VDF-TrFE) matrix. Measurements are performed under various biasing conditions, sweeping frequency and nano particle loadings for extensive characterization. FEM analysis was used to gain more insight about the underlaying physics and their interactions, including magnetism, electrostatic and structural mechanics. The governing constitutional equations are presented and discussed. Subsequently, the model is used to simulate

the effect of nanoparticles size, their concentration and effect of agglomeration in the overall output voltage of the multiferroic capacitor.

9.2. Outlook

The findings presented in this thesis are encouraging to use polymer-based multiferroic materials in order to realize a hybrid magnetic-electric single transistor memory, which is capable of storing information in form of electric polarisation and magnetic moments. Multiferroic composites consisting of ferromagnetic nanoparticles dispersed in a ferroelectric P(VDF-TrFE) matrix can be used as the gate insulator of the FET device. This enables the modulation of the channel current both with a magnetic and electric field due to the established coupling between these two ferroic orders.

The generic device model, presented for graphene FeFETs in this thesis, can be used for other 2D materials like MoS_2. This is especially interesting since MoS_2, contrary to graphene which is a bandgap-less semiconductor, has an intrinsic band gap. Therefore, it is expected that the obtained FeFET using MoS_2 will demonstrate a higher on/off ratio due to its band structure.

Moreover, the introduced polymer-based multiferroic nano composites can be the key step for realization of high-efficiency energy harvesters, supplying wearable and implantable gadgets, where bulky batteries are not a practical option. This is especially desired since polymer-based energy harvesters have the advantage of mechanical flexibility and can be interfaced in a conformable fashion.
Additionally, geometrical modification of the obtained energy harvesting device, like introducing pores as discussed in a dedicated chapter in this thesis, can be employed to improve the overall performance of the final device.

Appendix A

Following scripts were used to generate the geometry of the finite element problem in the COMSOL Multiphysic's method editor environment using Java programming language.

A) Generating geometry of the FEA problem with randomly distributed core-shell ferroic nanoparticles in a cubic polymer matrix:

```java
int NUMBER_OF_Particles = 75;       // number of ferroic nano particles
int ind = 1;                        // index for addressing the particles

model.component("comp1").geom("geom1").lengthUnit("um"); // defining the unit of length
model.component("comp1").geom("geom1").feature().clear();

// defining position and radius of particles Pcr & Pcteta : particle coordination in cylindrical system
radius and tetha respectively

double [] Px;
double [] Py;
double [] Pz;
double [] Pr;

// defining shell radius around the particles
double Shell_r = 0.035;
int NIs = 0;

Px = new double [NUMBER_OF_Particles];
Py = new double [NUMBER_OF_Particles];
Pz = new double [NUMBER_OF_Particles];
Pr = new double [NUMBER_OF_Particles];

// defining polymer matrix dimensions

double Film_HEIGHT_Z = 0.44;
double Film_WIDTH_Y = 0.44;
double Film_LENGTH_X = 0.44;

// This Flag is used to check if Z of nanoparticle is inside the cylinder or not
boolean PassFlag = true;
// This "Over Lap Avoidence Flag" is used to prevent nanoparticles overlapping
boolean OLAPassFlag = true;

double sx, sy, sz = 0.0;
double Particle_MIN_RADIUS = 0.035;
double Particle_MAX_RADIUS = 0.035;
Px[0] = 0.0;
Py[0] = 0.0;
Pz[0] = 0.0;
Pr[0] = 0.0;
```

```java
model.component("comp1").geom("geom1").create("Air-Block", "Block");
model.component("comp1").geom("geom1").feature("Air-Block").set("pos", new double[]{-0.75, -0.75,
-0.75});
model.geom("geom1").feature("Air-Block").set("size", new double[]{2, 2, 2});
model.component("comp1").geom("geom1").create("PVDF-Block", "Block");
model.component("comp1").geom("geom1").feature("PVDF-Block").set("pos", new double[]{0.0, 0.0,
0.0});
model.geom("geom1").feature("PVDF-Block").set("size", new
String[]{Double.toString(Film_LENGTH_X), Double.toString(Film_WIDTH_Y),
Double.toString(Film_HEIGHT_Z)});

while (ind < NUMBER_OF_Particles)

{

  while (OLAPassFlag && PassFlag)

  {

    Pr[ind] = Math.random()*(Particle_MAX_RADIUS-Particle_MIN_RADIUS)+Particle_MIN_RADIUS;
    Px[ind] = Math.random()*Math.abs(Film_LENGTH_X);
    Py[ind] = Math.random()*Math.abs(Film_WIDTH_Y);
    Pz[ind] = Math.random()*Math.abs(Film_HEIGHT_Z);



    if (Px[ind] < (Film_LENGTH_X-(Pr[ind]+Shell_r)) && Px[ind] > (Pr[ind]+Shell_r) && Py[ind] <
(Film_WIDTH_Y-(Pr[ind]+Shell_r)) && Py[ind] > (Pr[ind]+Shell_r)
        && Pz[ind] < (Film_HEIGHT_Z-(Pr[ind]+Shell_r)) && Pz[ind] > (Pr[ind]+Shell_r))

    {

      for (int i = 0; i < ind; i++)

      {

        if (Math.sqrt(Math.pow((Px[i]-Px[ind]), 2)+Math.pow((Py[i]-Py[ind]), 2)+Math.pow((Pz[i]-Pz[ind]),
2)) > (Pr[ind]+Pr[i]+2*Shell_r))

        {
          OLAPassFlag = false;
        }

        else

        {
          OLAPassFlag = true;
```

```
            PassFlag = true;
            break;
          }


       }
     }
     else
     {
       NIs++;
       PassFlag = true;
       OLAPassFlag = true;
       continue;
     }

   }

   sx = Px[ind];
   sy = Py[ind];
   sz = Pz[ind];


   model.component("comp1").geom("geom1").create("sphA"+ind, "Sphere");
   model.component("comp1").geom("geom1").feature("sphA"+ind).set("r", Pr[ind]);
   model.component("comp1").geom("geom1").feature("sphA"+ind).set("pos", new double[]{sx, sy, sz});

   model.component("comp1").geom("geom1").create("sphB"+ind, "Sphere");
   model.component("comp1").geom("geom1").feature("sphB"+ind).set("r", Pr[ind]+Shell_r);
   model.component("comp1").geom("geom1").feature("sphB"+ind).set("pos", new double[]{sx, sy, sz});


   model.component("comp1").geom("geom1").create("Dif"+ind, "Difference");
   model.component("comp1").geom("geom1").feature("Dif"+ind).set("keep", "off");
   model.component("comp1").geom("geom1").feature("Dif"+ind).selection("input").set("sphB"+ind);
   model.component("comp1").geom("geom1").feature("Dif"+ind).selection("input2").set("sphA"+ind);

   model.component("comp1").geom("geom1").create("sphCore"+ind, "Sphere");
   model.component("comp1").geom("geom1").feature("sphCore"+ind).set("r", Pr[ind]);
   model.component("comp1").geom("geom1").feature("sphCore"+ind).set("pos", new double[]{sx, sy,
sz});

  ind++;
  OLAPassFlag = true;
  PassFlag = true;
}
model.component("comp1").geom("geom1").run();
```

B) Generating geometry of the FEA problem with randomly distributed bare ferroic nanoparticles in a cubic polymer matrix:

```
int NUMBER_OF_Particles = 54;           // number of ferroic nano particles
int ind = 1;                            // index for addressing the particles
model.component("comp1").geom("geom1").lengthUnit("um");  // defining the unit of length
model.component("comp1").geom("geom1").feature().clear();

// defining position and radious of particles Pcr & Pcteta : particle cordination in cylandrical system
radious and teta respectivly

double[] Px;
double[] Py;
double[] Pz;
double[] Pr;

int NIs = 0;

Px = new double[NUMBER_OF_Particles];
Py = new double[NUMBER_OF_Particles];
Pz = new double[NUMBER_OF_Particles];
Pr = new double[NUMBER_OF_Particles];

// defining polymer matrix dimensions
double Film_HEIGHT_Z = 0.44;
double Film_WIDTH_Y = 0.44;
double Film_LENGTH_X = 0.44;

/// This Flag is used to check if Z of nanoparticle is inside the cylander or not
boolean PassFlag = true;
/// This "Over Lap Avoidence Flag" is used to prevent nanoparticles overlaping
boolean OLAPassFlag = true;

double sx, sy, sz = 0.0;

double Particle_MIN_RADIUS = 0.02;
double Particle_MAX_RADIUS = 0.02;

model.component("comp1").geom("geom1").create("Air-Block", "Block");
model.component("comp1").geom("geom1").feature("Air-Block").set("pos", new double[]{-0.75, -0.75, -0.75});
model.geom("geom1").feature("Air-Block").set("size", new double[]{2, 2, 2});

Px[0] = 0.0;
Py[0] = 0.0;
Pz[0] = 0.0;
Pr[0] = 0.0;

model.component("comp1").geom("geom1").create("blk"+1, "Block");
```

```java
model.component("comp1").geom("geom1").feature("blk"+1).set("pos", new double[]{0.0, 0.0, 0.0});
model.geom("geom1").feature("blk"+1).set("size", new String[]{Double.toString(Film_LENGTH_X),
Double.toString(Film_WIDTH_Y), Double.toString(Film_HEIGHT_Z)});
while (ind < NUMBER_OF_Particles)

{
  while (OLAPassFlag && PassFlag)
  {

    Pr[ind] = Math.random()*(Particle_MAX_RADIUS- Particle_MIN_RADIUS)+Particle_MIN_RADIUS;
    Px[ind] = Math.random()*Math.abs(Film_LENGTH_X);
    Py[ind] = Math.random()*Math.abs(Film_WIDTH_Y);
    Pz[ind] = Math.random()*Math.abs(Film_HEIGHT_Z);

    if (Px[ind] < (Film_LENGTH_X-Pr[ind]) && Px[ind] > Pr[ind] && Py[ind] < (Film_WIDTH_Y-Pr[ind]) &&
Py[ind] > Pr[ind] && Pz[ind] < (Film_HEIGHT_Z-Pr[ind]) && Pz[ind] > Pr[ind])

    {

      for (int i = 0; i < ind; i++)

      {

        if (Math.sqrt(Math.pow((Px[i]-Px[ind]), 2)+Math.pow((Py[i]-Py[ind]), 2)+Math.pow((Pz[i]-Pz[ind]),
2)) > (Pr[ind]+Pr[i]))

        {
          OLAPassFlag = false;
        }

        else

        {
          OLAPassFlag = true;
          PassFlag = true;
          break;
        }

      }
    }
    else
    {

      NIs++;
      PassFlag = true;
      OLAPassFlag = true;
      continue;
    }
  }
```

```
   sx = Px[ind];
   sy = Py[ind];
   sz = Pz[ind];

   model.component("comp1").geom("geom1").create("sph"+ind, "Sphere");
   model.component("comp1").geom("geom1").feature("sph"+ind).set("r", Pr[ind]);
   model.component("comp1").geom("geom1").feature("sph"+ind).set("pos", new double[]{sx, sy, sz});

   ind++;
   OLAPassFlag = true;
   PassFlag = true;
}
model.component("comp1").geom("geom1").run();
```

Publications

1) An iontronic multiplexer based on spatiotemporal dynamics of multiterminal organic electrochemical transistors, D. Koutsouras, **M.H Amiri**, Paul Blom , F. Torricelli , K. Asadi, P. Gkoupidenis
Adv. Funct. Mater. 2021, 2011013 (**Same contribution first author**)

2) Crossbar Array of Artificial Synapses Based on Ferroelectric Diodes, L. Seufert, **M. H. Amiri**, P. Gkoupidenis, K. Asadi
Adv. Elec. Mater Oct. 2021, **(Same contribution first author)**

3) Thin-Film Polymer Nanocomposites for Multiferroic Applications, H Sh Dehsari, M Kumar, A Saad, **M. H. Amiri**, C Yan, K Asadi
ACS Applied Nano Materials 1 (11), 6247-6257

4) Self-Power Cardiac Pacemaker by Piezoelectric Polymer Nanogenerator Implant, S. Azimi, A. Golabchi, A.Nekookar, Sh. Rabbani, **M. H. Amiri**, K. Asadi, M.M. Abolhasani
Nano Energy, 2021, 105781

5) Piezoelectric Nylon-11 Fibers for Electronic Textiles, Energy Harvesting and Sensing, S. Anwar, **M.H Amiri**, S. Jiang, M. M Abolhasani, Paulo R. F. Rocha Kamal Asadi
Adv. Funct. Mater 2020, 2004326

6) Hierarchically structured porous piezoelectric polymer nanofibers, M.M.Abolhasani, M. Naebe, **M.H Amiri**, K. Shirvanimoghaddam, S. Anwar, J. J. Michels, K. Asadi
Adv. Sci. 2020, 2000517

7) Self-Poled Sausage-like PVDF Nanowires as Novel Piezoelectric Nanogenerators, H. Soleymani, M. Noormohammadi, M. Almasi Kashi, **M. H. Amiri**, Jasper J. Michels, Kamal Asadi and Mohammad Mahdi Abolhasani
Adv. Mater. Interfaces. 2021, 2001734

8) Porous graphene/poly(vinylidene fluoride) nanofibers for pressure sensing, M. M. Abolhasani, S. Azimi, M. Mousavi, S. Anwar, **M. H. Amiri**, K. Shirvanimoghaddam, M. Naebe, J. Michels, K. Asadi
J. Appl. Polym. Sci. Feb 2022

9) Design Rules for Memories Based on Graphene Ferroelectric Field-Effect Transistors, **M H Amiri**, J Heidler, K Müllen, K   Asadi,
ACS Appl. Electron. Mater. 2020, 2, 1, 2-8

10) Designing multi-level resistance states in graphene ferroelectric transistors, **M.H Amiri**, J. Heidler, K. Müllen, P. Gkoupidenis, K. Asadi
Adv. Funct. Mater. 2020, 2003085

11) Doping free transfer of graphene using aqueous ammonia flow, **M. H Amiri**, J Heidler, A Hasnain, S Anwar, H Lu, K Müllen, K Asadi
RSC Advances 10 (2), 1127-1131

12) Polymer Field-Effect Transistor Memory Based on Ferroelectric Nylon Gate Insulator, S Anwar, B Jeong, MM Abolhasani, W Zajaczkowski, **M. H Amiri**, K Asadi
J. Mater. Chem. C 2020, 8, 5535